Rapid Acceleration of Legged Robots

A Pneumatic Approach

Author:

Joshua van Zyl

VZYJOS003@myuct.ac.za

Supervisors:

A/Prof. Amir Patel

Dr Reuben Govender

Department of Electrical Engineering

University of Cape Town

South Africa

MSc(Eng) thesis submitted in fulfilment of the requirements for the degree of Master of Science in the Department of Electrical Engineering at the University of Cape Town

August 2021

Keywords: Pneumatic; Robot; Agility

Declaration

I, Joshua van Zyl, hereby:

1. I know that plagiarism is wrong. Plagiarism is to use another's work and pretend that it is one's own.
2. I have used the IEEE convention for citation and referencing. Each contribution to, and quotation in, this report from the work(s) of other people has been attributed, and has been cited and referenced.
3. This report is my own work.
4. I have not allowed, and will not allow, anyone to copy my work with the intention of passing it off as their own work or part thereof.

I know the meaning of plagiarism and declare that all the work in the document, save for that which is properly acknowledged, is my own. This thesis/dissertation has been submitted to the Turnitin module (or equivalent similarity and originality checking software) and I confirm that my supervisor has seen my report and any concerns revealed by such have been resolved with my supervisor.

Joshua van Zyl

Department of Electrical Engineering

University of Cape Town

Monday 9th August, 2021

Abstract

For robotics to be useful to the public in a multifaceted manner, they need to be both legged and agile. The legged constraint arises as many environments and systems in our world are tailored to able-bodied adults. Therefore, a practically useful robot would need to have the same morphology for maximum efficacy. For robots to be useful in these environments, they need to perform at least as well as humans, therefore presenting the agility constraint. These requirements have been out of reach of the field until recently.

The aim of this thesis was to design a planar monopod robot for rapid acceleration manoeuvres, that could later be expanded to a planar quadruped robot. This was achieved through a hybrid electric and pneumatic actuation system. To this end, modelling schemes for the pneumatic cylinder were investigated and verified with physical experiments. This was done to develop accurate models of the pneumatic system that were later used in simulation to aid in the design of the platform.

The design of the platform was aided through the use of Simulink to conduct iterative testing and multivariate evaluations using Monte Carlo simulation methods. Once the topology of the leg was set, the detail design was conducted in Solidworks and validated with its built in simulation functions. In addition to the mechanical design of the platform, a specialist boom was designed. The design needed to compensate for the forces the robot exerts on the boom as well as the material constraints on the boom. This resulted in the development of a cable-stayed, four bar mechanism boom system.

An embedded operating system was created to control the robot and take in and fuse sensor inputs. This was run using multiple sensors, sub-controllers and microcontrollers. Sensor fusion for the system was done using a Kalman Filter to improve readings and estimate unmeasured states of the robot. This Kalman Filter took LiDAR and accelerometer readings as inputs to the system to produce a sub-centimetre accurate position measure for the system.

Finally, the completed platform was validated using fixed-body forward hopping tests. These tests showed a significant degree of similarity to the simulated results and therefore validated the design process.

Acknowledgements

This project would not have been possible without the support of my supervisor AProf. Amir Patel and co-supervisor Dr. Reuben Govender. Their frequent advice kept me from wondering out too far into the weeds of research.

To Amir thanks for exposing me to a whole different side of engineering in sensor fusion and optimisation that I might well have never even heard of otherwise.

To Reuben thanks for always being infectiously optimistic and positive regardless of the situation at hand and even more so for helping me and supporting this project before ever being brought on to co-supervise.

This acknowledgment section would be a farce if I omitted thanks for my mentor and collaborator on this project Dr. Callen Fisher. Thanks for introducing me to the lab the field and helping out with all manner of testing and debugging and joining me for a beer to vent when things really weren't working. You've been a great mentor and friend through this chapter of my life.

Acknowledgment must also go to all the other members of the mechatronics lab for chipping in to lend a hand or taking a look at some code to help debug it when the need arose.

Thanks to all the technical staff in both the Electrical and Mechanical Engineering Departments as without our help and advice this project would never have been possible and a special thanks to Pierre Smith and Riyaad Jacobs for taking the time to teach me more about machining.

Finally thanks to my family for all the support through the stressful times on this project.

The financial assistance of the National Research Foundation (NRF) towards this research is hereby acknowledged. Opinions expressed and conclusions arrived at, are those of the author and are not necessarily to be attributed to the NRF. Grant number: 117744 and 101245. Acknowledgement for the financial assistance for the Author through the VC Research Scholarship and 10A funding is extended to the University of Cape Town. Further financial assistance is acknowledged from the Ada and Bertie Levenstien Bursary.

Contents

List of Figures

List of Tables

Chapter 1: Introduction

The design of the modern world has been shaped by a conceptualisation of the target demographic who use it. This demographic has largely been able-bodied adults - leading to designs that can be challenging for anyone or anything that does not fit this legged template. These design choices are ubiquitous and include stairs, grates and curbs where the problems they create are observable in the difficulty disabled people have in navigating them. These interactions are still difficult despite modern laws and regulations with respect to accessibility[1][2][3]. For this reason robots need to move in a way that spaces are designed for - walking.

Past robotics literature has revealed a number of walking platforms, which are generally slow moving, making them less practical [4]. To this end, we need to look for platforms that are capable of high levels of agility to keep up with or surpass humans. A number of recent state-of-the art platforms are currently pushing the limits of robotic agility, namely Atlas [5] and Atrias [6]. The final obstacle to useful legged robots is that of control. These systems and their desired tasks are extremely complex and nonlinear, resulting in designing controllers becoming an intractable task.

Figure 1.1: Accessibility issues in the developed world [3]

1.1 Motivation

Legged locomotion is a problem that does not have a *singular solution*. There are multiple ways walking has been achieved in nature, with differing degrees of agility. This variance is seen with bipeds like ostriches [7], quadrupeds like cheetahs [8], and even decapods like crabs [9]. The complexity of legged robotics makes it necessary for engineers to look to nature to help inspire the design of robotic platforms and inform some of the design choices made. To this end, all of the animals listed previously have had bio-inspired robots modelled after them [10] [11] [12].

Despite the inspiration we get from nature it is not exactly analogous to the technology we have available. This has caused a divergence in research between those that seek to copy the process of how something is done (bio-mimicry) and those that only want to achieve its outcomes (bio-inspiration). The creative use of actuators that don't have a comparison in nature allows for potentially better implementations in mechanical systems due to the divergence of requirements[13].

This difference is also important from a control perspective and is due to the fact that robots tend not to be computing dynamic manoeuvres in real time. Instead, large sections of work are focused on either steady-state control in the form of limit cycles [14] or heuristic controllers such as Spring Loaded Inverted Pendulum (SLIP) models [15]. These models reduce the complexity of the real world problems being solved but often are not very accurate approximations of the systems they are being used to control.

In spite of all of these complexities, legged robots are still worth pursuing. This pursuit is driven by the need for robots to be legged to be able to be used in unpredictable and often non-ideal environments. For this to become a reality robots need to perform in highly agile and controllable manners.

To this end, this thesis seeks to develop a platform and environment to allow for the testing of different robotic platforms and feedback controllers. The platform itself needs to be modular to allow for the testing of the varied morphologies mentioned earlier, while the testing environment needs to be robust and platform independent to allow for the testing of different platforms.

1.2 Aims of the Study

The aim of this project was to explore the design of an expandable legged robot for transient manoeuvres (manoeuvres where the platform accelerates to a steady-state or decelerates away from it). This aim was split into a number of objectives.

The purpose of this study was to evaluate the validity of the use of pneumatic cylinders as active actuators in robotic platforms. This project was restricted to a monopod, rather than a bipedal or quadrupedal robot, in order to be feasible within MSc timelines. To overcome the inherent instability of a monopod, a support boom will be used to ensure the limb movement approximates planar motion. The platform constructed for the monopod and support boom should be expandable in the future to allows for testing in a planar quadruped or biped configuration

1.2.1 Objectives of the Study

The design of the robot was primary objective to be capable of performing agile manoeuvres with the secondary objective of being modular to allow for expansion of the platform in the future. The platform was also to be as simple as possible. This simplicity was to not only simplify the control of the platform but also to allow for its use in trajectory optimisation.

In order to use trajectory optimisation methods, a reduced order model of the platform was required. This needed to be validated experimentally to qualify its use in future design simulations for the system.

For testing purposes a sagittal plane (the plane splitting the left and right sides of the body) support structure would be required. This structure needed to effect the motion of the platform as little as possible and where it did effect it it needed to be as uniform an effect as possible.

The final objective was to develop a controller to perform a long-time-horizon task - one where it started and ended at rest while covering a fixed distance. This system controller would be required to take sensor inputs from the system and condition these inputs to

generate useful data. This needed to be paired with a controller to manage the output of the system.

1.2.2 Purpose of the Study

The purpose of this study was to evaluate the validity of the use of pneumatic cylinders as active actuators in robotic platforms. The platform constructed for this should also be expandable in the future to allow for testing in a planar quadruped or a biped robot configuration. A generalised test rig was required to be developed for easier testing of other platforms without having to create custom infrastructure.

1.3 Scope, Limitations and Constraints

Several generic limitations were placed on the platform due to its nature as a masters project. These were:

- 24 months to complete the project;
- As few custom components as possible;
- The use of freely available and easily machinable materials;

To set the scope of the project to what was manageable the following additional constraints were added:

- The platform would not be required to run outside of a lab;
- The platform would never have to run unsupported;
- The platform would not have to carry its own power source;
- No actuators or drivers for those actuators would be constructed;
- and finally the evaluation of the success of the design would be based on its functionality and not the implementation of a controller on it.

The support structure was required due to the monopod implementation of the system. Due to the requirement for this support structure it logically followed that the system would be running in a lab and therefore would also not require on board power.

1.4 Plan of Development

This report is broken into four main sections and can be seen in Figure 1.2 below. The first of these is the background, this section contextualises the research being done and structure of the report. The second section concerns how the design of the platform was chosen. The third section concerns the control system of robot and the other components required for the system to run. The final section is the system evaluation which covers the testing of the platform and any improvements that could be made to it.

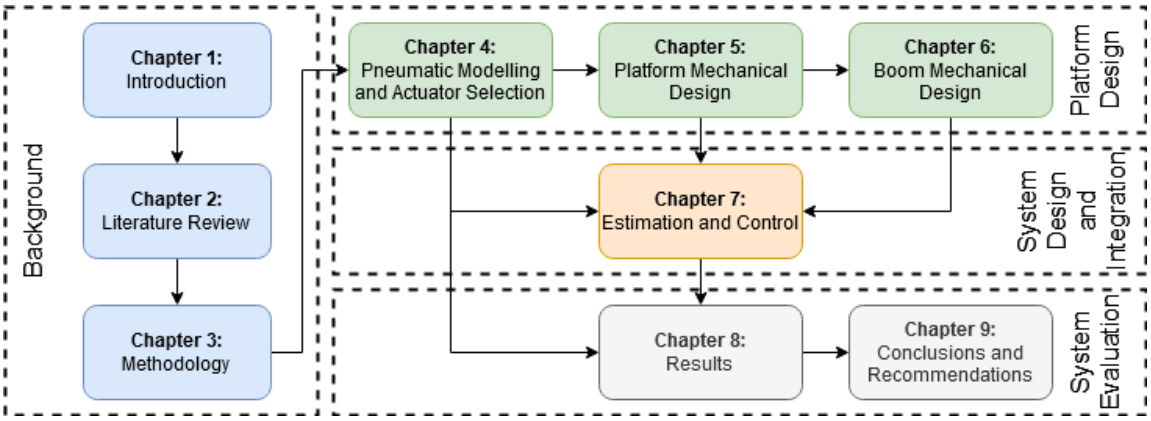

Figure 1.2: Flow and structure of the report

The report follows with Chapter 2 which lays out the work that has already been done in the field and helps explain the trade-offs made in the design of legged robots. This serves as the basis to motivate the decisions that will follow. Chapter 3 discusses the methodology used in the design of the platform, embedded system and associated components. This chapter also discusses the testing procedures used to validate the system.

Chapter 4 describes the actuator selection process. This chapter also develops different modelling schemes for pneumatic cylinders and the validation process for these models. Chapter 5 describes the mechanical design of the system while Chapter 6 discusses the associated boom. These chapters consider the motivating factors for the design choices

made from a performance and design optimisation standpoint.

Chapter 7 describes the sensor array for the system and its integration. It also deals with sensor fusion, filtering and the embedded system design of the platform.

Chapter 8 describes the validation tests run on the robot and extracts meaningful metrics from the data to compare to other platforms. Finally, Chapter 9 discusses the culmination of the work done and if the objectives of the project were met. This chapter also describes possible changes and additional areas of work worth exploring.

Chapter 2: Literature Review

2.1 Legged Locomotion

Given how ubiquitous walking is, it could be assumed to be a trivial task and not the result of millions of years of evolution. The advancements made in nature due to evolution are, therefore, not to be taken lightly. On the scale of evolution, robotics is a new field. This is illustrated in the numerous videos of robotics competitions showing a montages of robots falling over, seemingly at random. This is not to say astounding progress hasn't been made with advances coming from both the academic and private sectors such as MIT's mini-cheetah [16] and Boston Dynamics Atlas [17]. Both of these platforms show how far the field has come and what is currently possible in terms of agility and robustness.

The long existence of walking toys, such as the Sony Aibo [18] from the late 1990s, also serves to diminish the problem. Indeed legged robots have existed for decades but the way that current advanced robots move is very different from older platforms. This is because these older platforms move in implicitly stable ways. These stable gaits work by always keeping the robots centre of mass within the support polygon of their foot contacts (seen in Figure 2.1 below). This is a very stable way to move but limits the manoeuvrability of the platform.

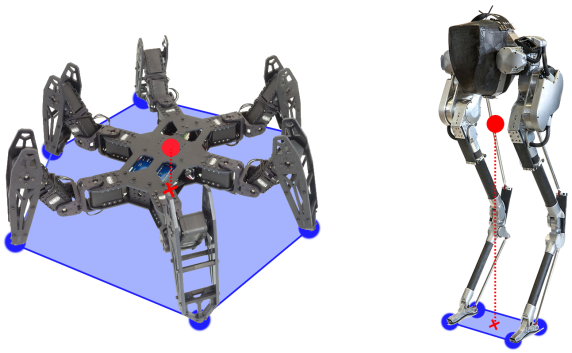

Figure 2.1: Contact polygon for a Hexapod (Left) and a Biped (Right). The blue area is the contact polygon, red dot is the centre of mass and the red cross is the centre of mass projected onto the plane of the contact polygon.

At this point, it is important to fully describe the concept of manoeuvrability as it underpins many of the decisions and constraints in this project. Manoeuvrability is a difficult metric to measure. At its core it is an acceleration-based metric - how fast can something reach its top speed or how quickly something can change direction. In short it is defined as the ability to change the velocity vector of the body of the robot [19]. It logically follows that the question of what the requirements for large accelerations in legged robots are and how different expressions of acceleration (positive, negative and turning) are achieved by mechanical design and feedback control [20].

It is also useful to consider how manoeuvrability differs from stability as alluded to earlier. These two metrics are often at odds, with very stable systems often being less manoeuvrable. In robots with the same number of legs, this is often a difference between fully and underactuated systems. Fully actuated systems are more stable as they have sufficiently powerful and numerous actuators to cancel out their dynamics. This allows for full control over these systems often using high gain feedback controllers making them significantly more stable than underactuated systems. The disadvantage to this is that these full actuated gait cycles are far less efficient and far slower than ones where the dynamics of the system are used to its advantage. These under-actuated systems are less stable as they have more degrees of freedom than degrees of control. This loss of stability is not without merit and can come with large gains in both speed and efficiency [21].

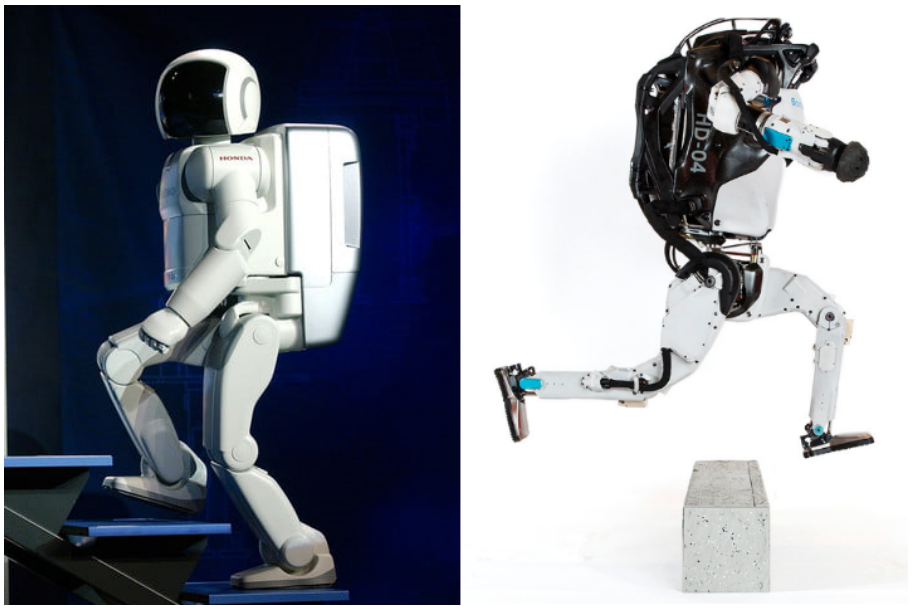

Figure 2.2: Asimo, a robot which cancels out its dynamics [4] (Left) vs Atlas, a robot that takes advantage of its dyanmics [5] (Right).

It is useful before continuing to make a distinction between biomimetic and bioinspired robotics. The distinction between the two is that while bioinspired robots seek to mimic the physical output of a system, biomimetic robots also seek to mimic the way that physical output was achieved [22].

Presently a great deal of research in robotics is specifically in the field of bioinspired robotics. This trend is especially prevalent in the field of legged robotics due to the complexity of inherent to this mode of locomotion. The animals used as a basis for this research are very diverse [23] and can range from cockroaches [24] on six legs, to cheetahs [25] on four legs and even flamingos on two legs [26]. The information we can gather from nature with respect to gait cycles and limb configurations can help inform both the design and control of these robotic platforms, and can help to narrow the possibility space.

2.2 Limb Design

Early legged walkers made use of fully stable gaits due to the control problem implicit to unstable higher speed gaits. These statically stable gaits work by constraining the centre of mass of the platform to lie within the contact polygon of the robot [27]. This can be seen as restricting the projected centre of mass to within the polygon as seen previously in Figure 2.1. These gaits are useful as they allow for the creation of very robust systems but tend to have a higher Cost of Transport (CoT usually defined as the energy input into the system over is final position, $CoT = \frac{\int E}{x_f}$, where E is the total energy input to the system and x_f is the final distance travelled by the system) and are slower than the alternate dynamically stable gaits [21].

As the field of robotics expanded, robot configurations requiring dynamically stable gaits began to emerge. The most emblematic of these designs is the monopod, as a statically stable gait for this robot does not exist. These monopods instead made use of SLIP (Spring Loaded Inverted Pendulum) based gaits [28] [29] [30]. These gaits assume that the centre of mass of the platform can be treated as following the same path as a Spring Loaded Inverted Pendulum and uses this assumption to reduce the order of the control

problem. These SLIP based gaits were also rapidly applied to other types of legged robots and could be seen on bipeds [31], quadrupeds [32] and even hexapods [33].

Research into such varied configurations of leg robots has highlighted several common features of well designed platforms: high power density, low leg inertia and force transparency of the actuators [34].

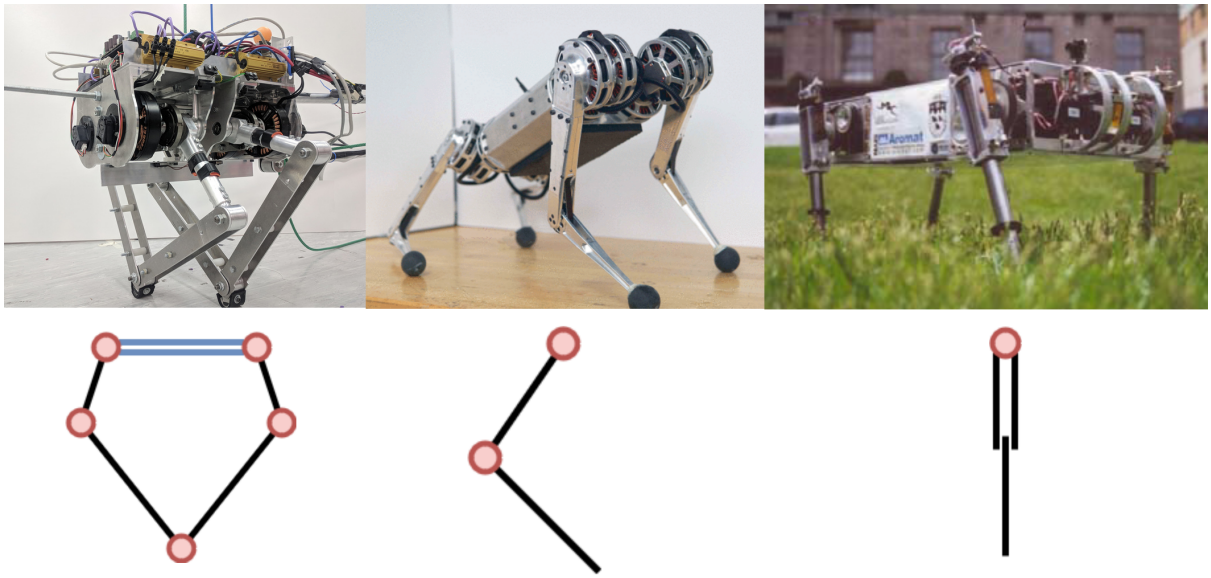

Figure 2.3: From left to right is Baleka [35] with a scissor 5 bar leg bellow it, MIT mini cheetah [16] with a series articulate leg, and Scout II [29] with a prismatic leg.

2.2.1 Four and Five Bar Linkage

These multi-bar linkage designs are conflated as they have very similar principals of operation and can be seen exemplified in the left of Figure 2.3. These designs make use of a scissor linkage with two motors, mounted in the body, controlling the position of the end effector. The 4 bar variant of this design is a divergence from a traditional 4 bar linkage as in this case the 5th linkage (depicted with parallel lines in Figure 2.3) is removed by having the motors co-axially located. The design has been seen in platforms such as Baleka [35], Stanford Doggo [36], ATRIAS [6] and others [37] [38]. The location of the motors in the body reduces the inertia of the leg allowing for greater accelerations and complies with the SLIP assumption of a massless leg. Further, the symmetry of the design allows for a more consistent force output than is seen in series articulate design [39].

This consistent force output also grants a high degree of proprioception. This symmetry may also cause a larger number, and variety, of feasible gaits as the force output doesn't vary as substantively to favour a specific gait.

In these multi-bar linkages, the two lower links are only loaded in compression, unlike series articulate designs where the lower links experience compression and bending. This allows scissor designs to have simpler limb geometry when designing for minimal inertia. This could also reduce the mechanical complexity for design as torque transmission to offset joints, as seen in many series articulate counterparts, is unnecessary.

2.2.2 Series Articulate

This is the only leg design seen in nature and is therefore also seen the most frequently in biologically inspired robots [31], [40], [41], [42]. This leg is comprised of two series links with actuation at each joint to independently control the succeeding link. An important design consideration with this type of leg design is how to actuate the knee joint. Mounting a motor at the knee joint increases the leg's inertia, reducing the performance of the leg. To avoid this, motors are often mounted on the body and transmit power to the knee. This is either done through the use of belt drives, such as on the MIT mini cheetah [16], chain drives such as those seen on StarlETH [43] or solid push rods such as on Cassie [44].

A further consideration required for this type of leg is its joint configuration. This is important as the direction of the joints can significantly effect performance. This impact on performance is also not consistent across a trajectory with certain mythologies providing better acceleration in exchange for worse braking [45].

2.2.3 Prismatic

The prismatic leg was one of the earliest leg designs used in robotics and can be seen frequently in the work of Marc Raibert in the 1980's [46] [32] [29]. Despite its age, this topology still appears in current research [47]. Prismatic platforms initially utilised pneumatic cylinders, but have since branched out into other technologies such as linear

motors [48].

The advantage of these platforms is a reduction in the component count for the legs due to the use of the actuator as a leg. Additionally, the prismatic nature of the leg reduces the number of reference frames and can, therefore, help in simplifying the simulation and control of the leg.

These platforms frequently make use of spring systems (or systems equivalent to springs in the case of pneumatic cylinders). This allows for these to act in a similar way to series elastic systems and can reduce the cost of transmission for the platform. The use of these legs as spring exciter systems can also further reduce the control problem as the platform will tend to a limit cycle based on the spring properties of the leg.

2.3 Existing Actuation Methods

The following section will evaluate the existing actuation methods and their relative advantages and disadvantages with respect to their use in legged robots.

2.3.1 Electric Motors

This section will consider the use of brushless DC (BLDC) motors as this is the most commonly used type of motor in the field of robotics. These are used over their bushed counterparts due to their better control characteristics and higher power to weight ratios. The use of BLDC motors is not the only choice in this actuator selection as there are many drivetrain options to consider as seen in Figure 2.4. These different drivetrains are chosen due to the torque, cost of transport and proprioception requirements for legged robots and will be explained in detail in the sections to follow.

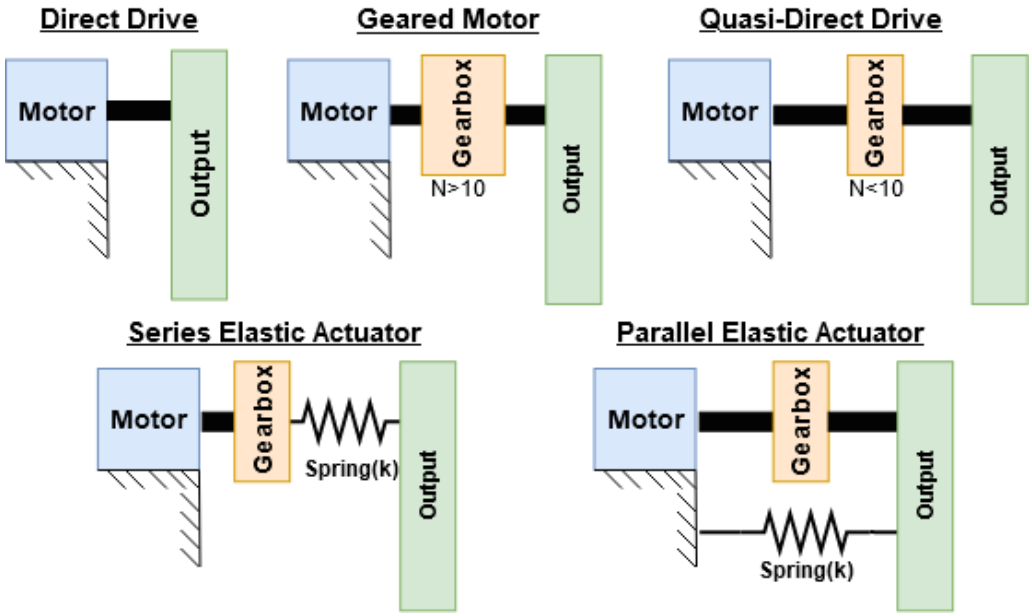

Figure 2.4: Diagram of commonly used drive trains for legged robots where N represents the gear ratio in terms of torque magnification from the motor and K represents spring stiffness (adapted from [39]).

2.3.1.1 Direct Drive

The simplest drivetrain option is direct drive - whereby the limb is attached directly to the rotating element of the motor. This method is used by robots such at Minitaur [37]. The advantage of doing this is that the torque generated by the motor is applied directly to the limb and the lack of additional gearbox inertias allow for a high degree of proprioception. This also reduces the chance of mechanical errors effecting the system as it reduces tolerances stack-up and backlash issues.

This system is not without its disadvantages as brushless DC motors generally do not meet the torque requirement in the desired speed range. These direct drive platforms are therefore limited in size to reduce their weight and lower the required maximum torque output. Furthermore, accurate position control of the limbs is limited in resolution by the number of poles of the motor and can result in cogging (the tendency for the motor to snap between its pole positions) if motors with too few poles are used.

2.3.1.2 High Reduction Systems

In contrast to the direct drive mentioned previously, are high reduction systems. These systems make use of gear ratios larger than 10 (though frequently significantly larger than this minimum) reductions to substantially increase the torque output of the motor. This reduction often comes through the use of harmonic drives - seen in ANYmal [49]. These high torque motors allow the system to overcome its dynamics and force itself into their intended positions. This type of drive is therefore often paired with a high gain controller to enforce its motion.

This drivetrain is not without its trade-offs, as these stiff systems reduce the proprioception of the system due to its stiff nature. These high reductions have an added disadvantage as high gear box inertias limit acceleration, these gearbox inertias can also prevent the system from being back driven leading to damage due to the shock loading inherent to legged locomotion. A further disadvantage of such a drivetrain is a reduction in the platform's ability to take advantage of its passive dynamics.

2.3.1.3 Quasi-Direct Drive

The quasi-direct drive is a compromise between the direct drive and high reduction systems and is characterised by having a speed reduction gear ratio between 2 and 10. By making use of these lower gear ratios the motor can more easily measure the forces applied on the limbs as the inertia magnification due to the gearbox is smaller than in the high reduction case. A further advantage is that the system can still be back-driven where the external forces on the robot can move the motor - this back-drivabilty can be used to lower the peak forces seen in the gearbox.

The disadvantage of such a system is that large BLDC motors still need to be used to reach the requisite minimum stall torque as the torque magnification factor is still relatively low. Other disadvantages can come from issues with the drive train implementation. The gearboxes require manufacturing to exacting tolerances which can increase the cost of the system or cause jamming if these tolerances are not met. Furthermore, gearboxes will inherently add some amount of backlash to the system which can make control more

challenging. The other commonly used reduction method is a belt drive, however this type of drive can stretch and require offset motor mountings. These quasi-direct drives are a rapidly growing tool in robotics and can be seen in robots such as the MIT Mini Cheetah [16] and Baleka [35].

2.3.1.4 Series and Parallel Elastic Actuation

The final factor in electrical drive systems is the decision to include an elastic element. This choice is made semi-independently of the previous three - all of which are concerned with gearing. Though the use of an elastic element is a separate choice, the decision of which to use is somewhat dependant on the rest of the drive trains implementation.

In the case of a series elastic actuator, the elastic element is attached to the output of the motor, or more likely gearbox, between it and the load. This allows the spring to absorb some of the shock of landing - a feature very useful in high reduction systems that can't be back driven. This shock absorption serves a dual purpose to protect the rest of the drivetrain from high impulsive loads and to re-purpose some of the energy from landing to reduce the CoT of the system. The disadvantage of this is that it makes the control of the system more difficult as the deflection of the spring has to be accounted for in its motion. This is a disadvantage for position control but can aid in force control as the spring deflection can be used to approximate the external load on the system though this comes with a reduction in control bandwidth [50].

In the case of parallel elastic actuators, the elastic element is connected between the limb of the robot and the body. This type of elastic element, therefore, captures energy during a touchdown phase which it releases during a take-off phase. The advantage of this is that the energy capture still helps protect drivetrain components by reducing shock loads (though not as significantly as in the series elastic case) and increases efficiency as some of the landing energy is stored. Further, the release of the stored energy in take-off increases the peak power output of the system [51] [52].

2.3.2 Hydraulics

Hydraulic actuators have been used in legged robots since the earliest days of the field and are seen on platforms like Big Dog [42], ZBot [53] and HyQ [54].

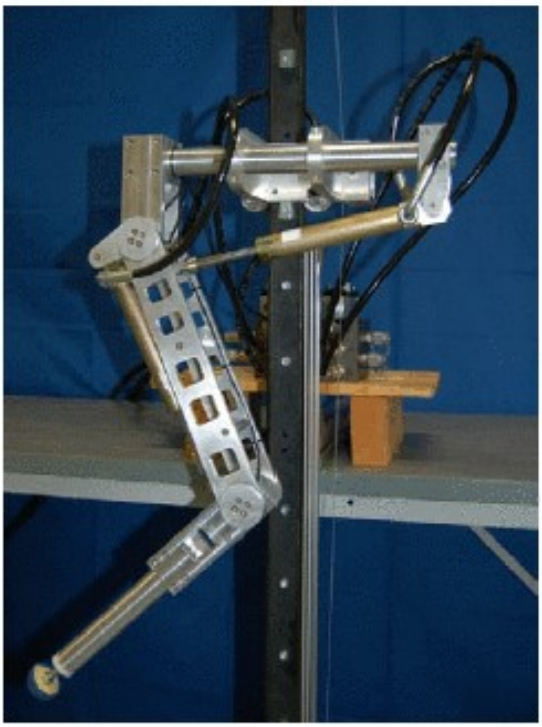

Figure 2.5: HyQ a hydraulically actuated series articulate robot [54]).

Hydraulic actuators have enjoyed such long-running usage due to their exceptionally high force output and accurate position and velocity control due to the incompressible nature of the hydraulic fluid used. In addition to this, hydraulic actuators tend to be linear actuators which can be advantageous for mechanical design.

These actuators are not without drawbacks though, as they require return lines for the hydraulic fluid and their pumps can be quite heavy. In the case of hydraulics, the high pressures used serve to further increase the weight of the pumps and cylinders used while the mass of the working fluid is also non-negligible. Furthermore, these actuators have a low-velocity limit set by the flow rate of fluid that can be pumped into the cylinder.

2.3.3 Pneumatics

Pneumatic cylinders, which use gas (typically air) as the working fluid rather than hydraulic oil, are typically faster and lighter than hydraulics. As the air is vented directly to the atmosphere, no return lines are needed, simplifying the system and further reducing mass. For these reasons, pneumatic cylinders have been used in the field of legged robotics since its inception [28] and are still in use today in platforms such as the Festo Kangaroo [40] seen in Figure 2.6 as well as others [55] [56].

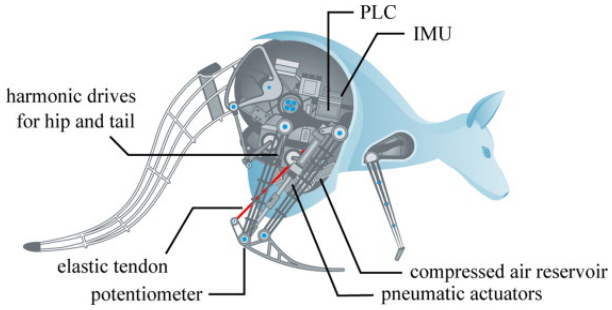

Figure 2.6: The pneumatically actuated Festo Kangaroo with its own onboard air supply [40]).

The behaviour of the cylinder is then determined by the valve configuration attached to it, with modern valve systems being capable of speed, position, or force control through the use of off the shelf proportional control valves or custom servo valve solutions [57] [58] [59]. Though impressive these valves often reduce the top speed of the cylinder and have relatively high settling times. In addition to any potential control disadvantages, pneumatic cylinders also require the use of potentially large or heavy accumulators to store the compressed air they use as a working fluid.

2.4 Legged Robot Design Principles

The design of legged robots is highly complex and dependent on an extremely large number of factors. For this reason, there is no singular mathematically optimal design for these systems. In place of this, there are a set of best practices that aid in the conceptualisation of the designs and narrows the design possibility space.

2.4.1 Leg Inertia

One of the most obvious design factors for legged robots is the minimisation of leg inertia, to maximise angular acceleration. Due to the high frequency of strides and relatively small operational angle ranges of the leg acceleration, and by extension torque, is often the limiting factor on legged robots. By decreasing leg inertia higher accelerations are possible for the robot.

An additional advantage of reducing the leg inertia of a platform is that it can increase body stability. This is due to conservation of momentum and is most visible in the aerial phase of a running gait. As the leg rotates form its take off to landing angle it swings rapidly and can cause the body to pitch as a reaction. By reducing the inertia of the leg the required body inertia for stability is also lowered and therefore this allows for smaller, lighter robots.

This need to reduce leg inertia is often achieved by moving actuators into the body instead of allowing them to sit in the joint where their toques act as seen in the MIT Cheetah [25]. Due to this several modern robots rely on relatively long belt or chain drives.

2.4.2 Force Output

A second logical design feature of legged robots is peak force output. The reason for this force requirement is to allow for greater ground contact forces which in turn allow for higher speeds. This is due to the positive correlation between both stride frequency and contact force, and overall top speed [60]. Furthermore, as the stride frequency increases the stance time decreases requiring very impulsive force outputs.

Though these high force outputs are required for legged robots they do not need to be sustained for long periods. The motion of a robot is equivalent to a high shock load case for mechanical design correction factors. This impulsive load case can also allow for a reduction in the specification of certain power components (such as motors and motor controllers) as the impulsive power output requirements will generally not cause an overheating failure.

2.4.3 Proprioception

Following on from the ability to output a high force is the principle that a robot should be able to sense its position in the world and the forces it applies on the world. This is more commonly referred to as proprioception and is done in several ways. Perhaps the most straight forward way is to attach a force sensor to the foot of the robot which can measure the force applied from the outside world and this has been done in the case of large robots such as LittleDog [61]. The issue with this approach is that these force sensors tend to be heavy, fragile and expensive; all of these features being suboptimal for being located at the foot of a robot. In an attempt to reduce the weight and cost of some of these senors they have been replaced with strain gauges. However, strain gauges are susceptible to the noise present in most robotics environments.

An alternate option is to make use of the actuators themselves as force sensors. For this to work, the force needs to be easily transmissible to the actuator generating its reaction force. In the case of electric motors, this means only allowing the use of the direct or quasi-direct drive. In these cases, the force is related to the current in or out of the motor [62]. Another way of measuring the force at the actuator is the use of a series elastic actuator. In this design the deflection of the elastic element is proportional to the applied load through Hooke's Law [50].

In the case of pneumatic or hydraulic cylinders, it means not letting the cylinder rest on its end stops and requires the use of additional fluid circuitry and the use of several pressure transducers. However, this can lead to a significant increase in the cost of the system and can reduce its maximum speed and force output.

The position sensing component of proprioception is easily achieved through the use of encoders (both rotary and linear) to find the position of the limbs in the platform's own reference space. The position of the platform's reference space is significantly more challenging and often requires the use of multiple sensors such as cameras, Inertial Measurement Units (IMU), ultrasonic sensors and LiDARs in addition to the other sensors on the robot.

2.4.4 Foot Design

A final critical factor in the design of legged robots is the foot design. Feet are an incredibly complex factor and are often treated as additional research on existing platforms [63]. The reason for this complexity is that feet cause several different effects that can often interact in unexpected ways [64].

The first factor to consider with feet is if the foot has a profile or a point. The advantage of a profile foot is that it increases the size of the contact polygon allowing for an increase in static stability. However, this is still a trade-off because these foot shapes can have undesirable effects when in motion. Some cases may require degrees of freedom in the form of an ankle joint. These ankle joints have been both passive and active and can serve to increase performance and efficiency but this comes at the expense of significantly increased complexity [65], [66], [67].

The second factor in foot design is the implicit spring-damper system in the foot. The large impulsive contact forces inherent in legged robots mean that any material will deform elastically and store energy as a spring. This problem is exacerbated in profiled feet due to their large bending loads. In addition to the spring-damper effects caused by the design of the foot, its material might also contribute. This contribution is due to the fact that robot feet are often made of high friction materials such as rubber which adds to the passive compliance of the foot. However, this is not to say that this is always negative, as with proper design of both these spring-damper feet and a controller designed to take advantage of them higher speeds and efficiencies might be achieved.

2.5 Sagittal Plane Support Systems

Due to the inherent limitations of planar robots, a support system is needed for the sagittal plane. This plane, seen in Figure 2.7 below, separates the left and right sides of the body and is often used in robots to reduce the cost of building platforms due to decreasing the number of limbs constructed. This reduction in scope also serves to reduce the control complexity of these platforms.

These planar supports can take many forms with each type having distinct advantages and disadvantages. These distinctions between supports will be discussed in detail below.

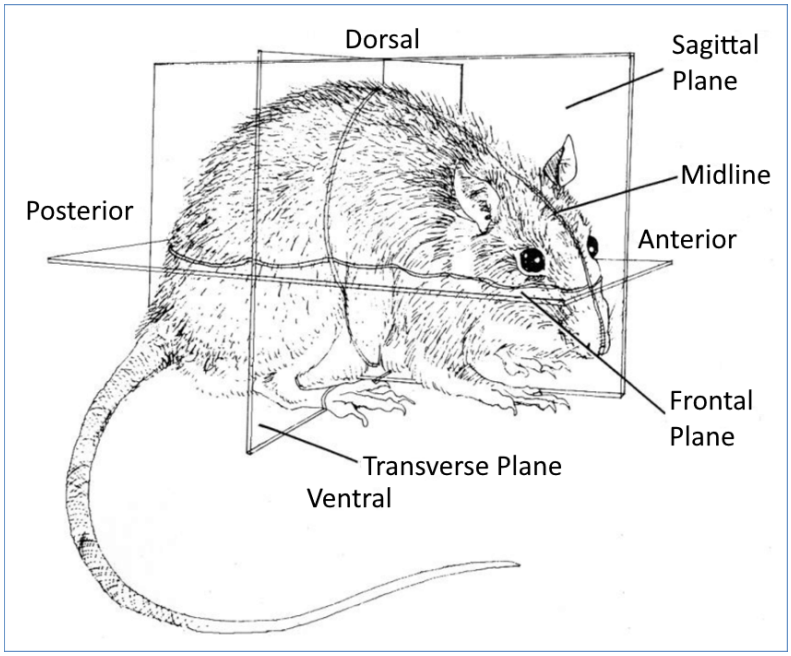

Figure 2.7: Planes of motion described based on a small quadruped image adapted from [68].

The key feature of any support system is that it should affect the dynamics of the robot as little as possible (outside of its role in the sagittal plane) and that any effect the support system would have should be sufficiently smaller than the internal dynamics of the system. Finally, the effect of the support on the system should be as consistent as possible and independent of the current configuration or orientation of the system [69].

2.5.1 Booms

Booms have been the standard in legged robotics since their inception and continue to be used to this day. The fact that they constrain robots to move in a circle allows for long tests to be run in a lab with limited space - a factor especially useful for long duration efficiency testing. The design of these booms is complicated with several variations (seen in Figure 2.8) attempted in the literature. Despite these variations, there are some universalities required for good boom design.

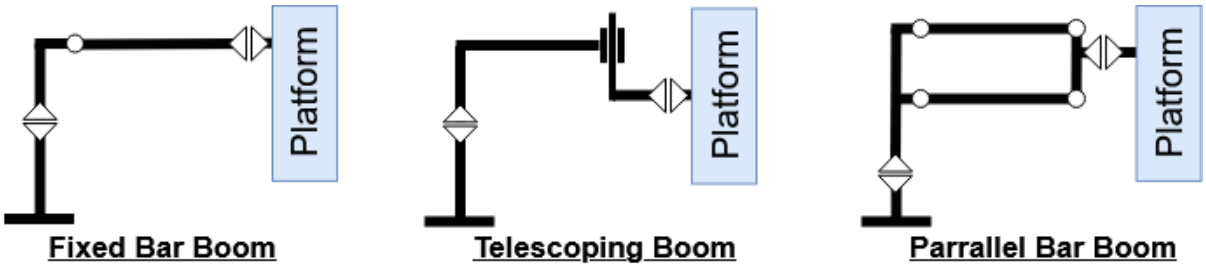

Figure 2.8: Diagram of commonly used boom designs.

These common factors are mass, rigidity, and length. These factors are all critically important but are often acting in opposition to each other - forcing compromises between them based on the requirements of the specific platform. Mass is a generally important factor for legged robots with reductions in mass directly improving performance in almost all cases. This weight requirement extends logically to the boom - which can be approximated as a payload on the robot. The next factor is rigidity; this factor is influential as if the boom is not sufficiently rigid it can act as a spring-mass system introducing extra dynamics the controller needs to account for. The final factor is the length of the boom. The length of the boom needs to be sufficiently long that a small angle approximation can assume the robot is moving in a straight line. The boom also needs to be long enough to ensure that the front and rear legs do not sit too far off of the tangent arc of the boom in the case of quadrupeds. This factor acts in tandem with the other two as increasing length increases both the mass and inertia of the boom worsening performance. This increase in inertia acts as a compound factor with an increase in the bending moment (due to the increase in inertia mass) to reduce rigidity.

In addition to the general factor above, there are several existing boom designs with different advantages and drawbacks seen in Figure 2.8. The most basic of these is the single bar fixed boom. In this configuration, a bar with two rotational degrees of freedom at the base connects to a one roll joint at its tip which in turn then connects to the robot. This design was used the most frequently [15], [26], [46], [70], [71] of all the boom options, likely because of its light weight and simplicity. The simplicity of this design makes it easy to manufacture and the need for only a single bar reduces the weight of the boom. However, as the robot's sagittal plane tilts as the boom moves it can be disadvantaged on takeoff and overly supported in areal phases. This can compromise the validity of any test as it might not allow the results to be extendable to non-boom scenarios.

To counteract the problem of a tilting sagittal plane, a linear guide fitted to the end of the boom can be used. This boom can only rotate about its base, the boom arm is then connected to a vertical rail followed by a roll joint before reaching the robot (as seen in Figure 2.8) [72]. This design solves the sagittal plane issue and can negate some rigidity concerns by having the beam of the pole be more fixed. However, this comes at a cost as the inertial mass of the boom, as seen by the robot, being different for vertical and horizontal motions. This can bias the platform towards certain gaits.

The final type of boom is the parallel bar boom. This boom uses equal bars to form a parallelogram that keeps the end effector perpendicular to the ground and can be seen in Figure 2.8. This is the second most common type of boom in the literature [30], [35], [73] likely due its perpendicularity. The second bar of such a boom is also useful as it can serve to increase the rigidity of the system. The counter point to this is that the second bar increases the weight of the boom and can cause a significant inertial mismatch if the bars are sufficiently offset.

2.5.2 Rail Systems

Rails are another possible support system. This type of support uses a set of rails above or below the platform to help stabilise the platform. A cart follows the robot forwards on a horizontal set of rails, while the second vertical set of rails allow it to move up and down. A pivoting arm could also support the robot rather than a second set of rails such as in Figure 2.9 below.

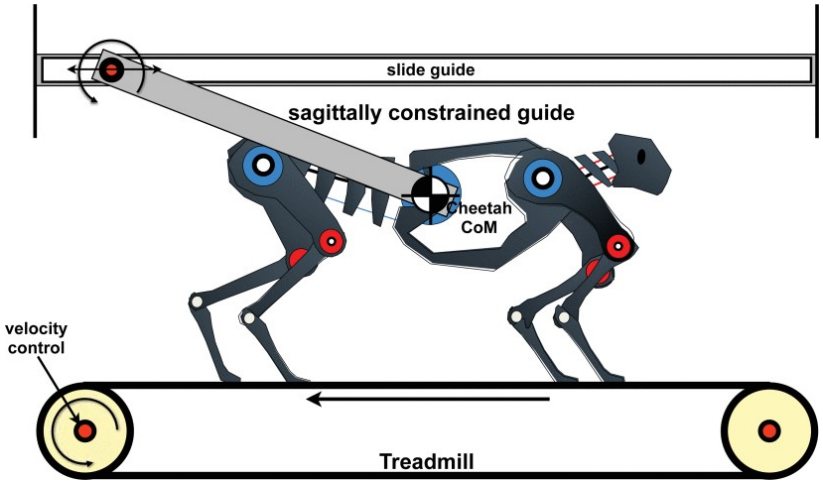

Figure 2.9: Support system for the MIT Cheetah robot [25].

This type of support has the major disadvantage of limiting test distances to the longest useable straight line in the lab; further by moving so far from its centre point power supply lines (electrical, pneumatic or hydraulic) increase in length and lead to higher transmission losses. There is also an additional problem in the sliding mass of the cart and the mismatched inertia of this type of support system. The final issue with such a system is that it requires a considerable infrastructure investment to build and install a sufficiently long set of rails to be useful [74].

The advantage of this system is that the robot is actually travelling in a straight line and not just approximating it as in a boom system. Furthermore, the smaller support arms can potentially reduce the mass of the system.

This type of system can be seen on the ARL Monopod II [75] and MIT Cheetah [25]. These platforms got around some of the issues of a rail system by paring it with a treadmill. The use of a treadmill greatly increase the viability of this type of system however this requires significant work to be done on the control system for the treadmill to ensure it will not effect the gait of the robot. Furthermore, due to the difference in force application due to the robot being stationary a treadmill can only be used to test steady-state gaits and is not viable for transient manoeuvres.

2.5.3 Trolley

A trolley system is similar to that of the rails system, however, in this case the large infrastructure requirements of the rails is minimised. It follows that a trolley would therefore have many of the same advantages and disadvantages as a rail system. The problems being the large sliding mass and the mismatched inertia, meanwhile, the carried over advantage is the fact that the system is moving in a straight line.

Where these designs differ is that by removing the rails system there is a reduction in the tolerances required for the system to work. This is due to the parallel constraint placed on rail systems. This could reduce the cost of such a system but could also increase in the mass of the cart. Further by reducing this tolerance there is less of a guarantee of the system moving in a straight line and this could have an effect on the safety of such a system. The trolley design has been used with platforms such as Spring Turkey [76].

2.5.4 Friction Sliding

The final type of support system considered was a friction slider system. This support makes use of 2 panels of low friction material (usually Perspex®) that sit on either side of the robot. The robot runs using these sheets as bumpers it can slide against. This type of solution was paired successfully with a treadmill for the Planar Elliptical Runner robot [77] seen in Figure 2.10.

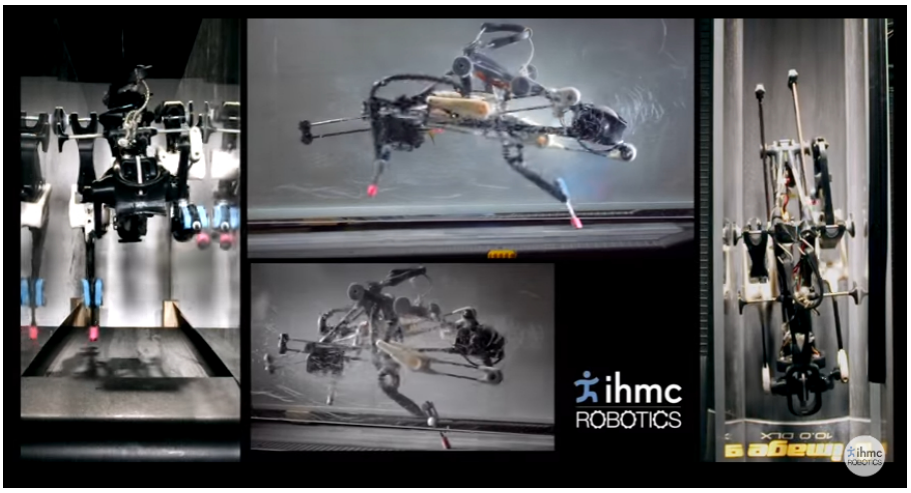

Figure 2.10: Elliptical Runner Robot running on a treadmill with friction slider bumpers [78].

This design counters the disadvantage of most other systems in their mismatched inertia's and additional mass on the platform. The problem with such a system is that large sheets of Perspex need to be acquired and supported to remain the correct distance apart. Multiple panels also need to be avoided as the seams between the sheets could negatively affect the robot. This puts a hard upper limit on the track length for a test. This limits this support system to very small tests or use paired with an inertial treadmill.

The removal of a fixed system limits sensors to being mounted on the platform itself causing some measurements to be more difficult to acquire. Finally, the Perspex sheets themselves place a limit on the maximum force and energy outputs of the robot. This force limit is needed to not damage the Perspex, escape its bounds or wedge itself in place.

2.6 Summary

This chapter evaluated the factors that go into the design of a planar robot. These factors are often highly intertwined and its important to note that some choices are more difficult to pair than others if not entirely incompatible. The leg design choices inform the actuator choices and can significantly alter how to adapt these decisions to fit with the best practice design principals. In addition to the design of the platform the design of the system around it is also critical and will effect the sensor choices and how those sensors are integrated into the system. This literature review therefore lays the ground work to inform the design choices and their associated trade-offs that come in future chapters.

Chapter 3: Design Requirements and Methodology

This project was broken down into several distinct sections required to develop and test the systems validity as a legged robotic platform. These sections included the actuator and drive system selection, mechanical design, support system design, sensor and system design, controller design and finally testing and validation.

This chapter serves to outline the constraining factors on the project and the approach used to design this system and evaluate its effectiveness.

3.1 Limitations and Constraints

Several limitations and constraints were placed on the project to limit the scope and increase the likelihood for success. Perhaps the largest constraint placed upon the system was that it would only be required to operate in a laboratory environment and only be required to move in a planar manner. This reduced the scope of the problem as the assumption of running in a lab means that a flat, level floor can be assumed, and the systems power supply does not need to be on the robot. The 2D assumption reduces not only the scope of the control problem but also reduces the minimum number of degrees of freedom that the platform would require to be viable.

A further limitation on the project was time and access to resources due to the COVID-19 pandemic as the South African national lockdown took away the ability to physically work on the platform or conduct tests for several months.

3.2 Platform Specifications

There are several factors that are critical to the design of legged robots as mentioned in Section 2.4. These factors can at times be antagonistic and therefore require different levels of priority. To establish this priority a pairwise comparison was conducted.

	Robustness	Leg Inertia	Force Output	Force Measurement	Proprioception	Shock Absorption Ability	Control Ability	Adherence to Control Heuristics	Weight	**Total**
Robustness	-	1	1	1	1	0.5	1	1	0.5	7
Leg Inertia	0	-	1	1	1	0	1	1	0	5
Force Output	0	0	-	1	1	0	1	1	0	4
Force Measurement	0	0	0	-	0.5	0	0.5	1	0	2
Proprioception	0	0	0	0.5	-	0	0.5	1	0	2
Shock Absorption Ability	0.5	1	1	1	1	-	1	1	0	6.5
Control Ability	0	0	0	0.5	0.5	0	-	0.5	0	1.5
Adherence to Control Heuristics	0	0	0	0	0	0	0.5	-	0	0.5
Weight	0.5	1	1	1	1	1	1	1	-	7.5

Table 3.1: Pairwise comparison table to establish precedence. 1 indicates the row value has precedence, 0.5 means equal precedence and 0 means that the column has precedence

From table 3.1 the weighting of the the various design parameters can be seen. This weighting between parameters was used to inform the trade-offs made in the design of the platform.

3.2.1 Actuator Specification

For a platform to be successfully used for transient manoeuvres, a minimum of two actuators are required. Though it is possible to use fewer actuators, this would, however, limit the ability of the platform to preform aggressive transient manoeuvres.

As a scissor leg had already been designed in the UCT Mechatronics lab, this morphology was not considered [35]. Therefore, the two required actuators could be considered separately as a shoulder actuator to position the leg and a 'knee' actuator to provide the power for the stride. This lead to different specifications for each actuator.

The shoulder actuator needed to be sufficiently high power to re-position the leg from the takeoff angle to the landing angle in the flight phase of the gait. This sets the minimum force or torque output required from the actuator in tandem with the inertia of the leg. A further requirement for this actuator is that it needs to be capable of accurate position control to reach a constant takeoff and landing angle.

The knee actuator has a different set of requirements to the shoulder. The knee required less fine control than the shoulder. In place of this fine control it needed to be capable of very high power outputs. Furthermore, there needed to be a robust method of transferring that power to the ground without significantly increasing leg mass or inertia. Finally, the leg actuator needed the ability to add in some passive compliance to shield the system from the shock load inherent to running.

3.3 System Design and Prototype Testing

3.3.1 Pneumatic Actuators

Due to the the non-negligible effects of upstream components on the performance of pneumatic actuators modelling had to be considered on a whole system level. This system includes the compressor, accumulator, piping, cylinder, and valves.

For the selection and model characterisation of pneumatic cylinders, single vertically constrained hop tests were conducted. These tests were done on a system where the accumulator size and pipe losses to the cylinder could be considered to be negligible. The motion of the cylinder was measured using a time of flight sensor and LiDAR, while the force was logged using a three-axis force sensor. This test was conducted for multiple hops with multiple cylinders of different strokes and bores to quantify their motion characteristics. This data was then used to find other properties of the system such as the switching delay in the solenoid valve and further back calculate the pipe flow and orifice losses in the system.

The data from these tests was used to size a compressor with respect to operating pressure and accumulator size, inform the modelling of the cylinders motion and size the cylinder for the final implementation on the platform. Finally the model developed was validated by conducting continuous hopping tests.

3.3.2 Leg Topology

The topology of the leg was evaluated in simulation. This was done primarily for actuator sizing purposes but also involved comparing series articulate and prismatic leg designs. These simulations were done using Simscape Multibody in addition to the models for pneumatic cylinders developed from the hopping tests in Section 3.3.1.

For the prismatic leg design the parameters of the legs were evaluated by conducting a grid search over the parameter space. After the initial results were evaluated the grid search was run again with finer graduations and tighter bounds limited by what was identified as good operating regions.

This solution was not possible for the series articulate design as there were several more variables of interest, making the problem size intractable for a typical grid search. For this reason Monte Carlo Simulation methods were used. This allowed for a wider solution space due to the random nature of the sweep. Similar to the previous simulation, once a good operating region was established the bounds of the Monte Carlo simulation were refined to allow for higher resolution in this good region.

3.3.3 Platform Mechanical Design

Once the topology for the system had been set from the simulation and the actuators had been sized, a mechanical design was generated. Due to the limited time available for this project it was only possible to generate a single working prototype.

The design was prioritised for ease of assembly and modularity. This was done to allow for future expansion of the platform or to allow for the testing of other leg configurations. An additional reason for this was for ease of maintenance in the event of a failure of any of the parts.

Due to the limited time for the design several iterations were done in the SOLIDWORKS CAD system. This allowed for the use of its built in design analysis tools to refine the design and ensure it would be sufficiently strong. Prior to machining parts from metal, test parts were prototyped using laser cutting and 3D printing to investigate any assembly or interference issues.

The final platform was manufactured from a combination of aluminium and steel, with aluminium selected for its light weight while certain parts were restricted to steel due to rigidity requirements. Machining for the platform was limited to the use of a 3-axis CNC milling machine, manual lathe and laser cutting.

3.4 Sagittal Plane Support Design

Due to the small size of the platform, a custom support system needed to be designed. This support system was under the same mechanical design constraints as the robotic platform.

A boom was chosen as it was the considered to be the only practically implementable system. This was due to the size constraints of the lab it was to run in and the time constraints on the project. To reduce the weight of the boom while maintaining its rigidity a cable stay method was decided upon. This would force the beams into compression at all times, remove slack from the system, increase stiffness and limit bending deflection.

Once a design for the support was found, its design process followed similarly to that of the robotic platform. The support design was limited to materials that could be easily obtained and fabricated, such as aluminium tubes, steel cables and 3D printed parts. More exotic materials such as carbon fibre reinforced polymer tubes were briefly considered, but were avoided due to complexities in fabricating with such materials.

Prior to the support system's use, the steel cables needed to be tensioned to consistent values while not exceeding the buckling load limit of the boom. This was done using the resonant frequency of the steel cables as a proxy measurement for tension.

3.5 System and Sensor Architecture

The original intention with the sensor system was to make use of 3 encoders on the boom along with the known geometry of the boom to find the position of the robot in 3D space. This plan was unsuccessful due to the deflection of the boom. The encoder system was still a viable method to measure the position of the robot not withstanding its vertical height. The use of an encoder to measure the position of the platform along the vertical axis was impractical due to the non-negligible boundary deflection of the boom. To counter this a height sensor was required.

Due to the short time duration of the motions, a high update rate was required. This combined with a non-contact sensing requirement limited the sensor selection to LiDAR units. A Garmin LiDAR Lite V3 was used, but had insufficient accuracy to be useful. To counteract this a Kalman Filter [79] was designed and implemented.

The Kalman Filter made use of a MPU9250 IMU unit in addition to the LiDAR. This was useful as the LiDAR (running at $500Hz$) was interspersed with the data the from the accelerometer running at $4kHz$. This increased the accuracy of the position measuring and brought it to a sub-centimeter level of accuracy. This sensor system is discussed further in Section 7.1 and can be seen in Figure 7.1

In addition to these encoders and the Kalman Filter inputs, a linear encoder was placed on the cylinder to measure the length of the leg and a feedback encoder was located on the motor to measure the angle of the leg.

3.6 Signal Processing

Signal processing is critically important to robotics. This is due to their being redundant sensor data that need to be fused or sensors that are less accurate than they need to be for their use case. Because of this, a series of techniques are used to improve the quality of the data being used. The type of processing varies based on the sensors used, processing overhead available and difficulty implementing. This section is by no means an exhaustive list or comparison of filtering techniques but rather a primer on Kalman Filters.

3.6.1 Kalman Filtering

Kalman Filters are a family of filters that have been in use for over 50 years. These filters act to reduce the noise in a system and fuse the inputs from multiple sensors into a single, coherent, state for the system - where the state represents the true values for all the parameters of concern at a given point in time.

These filters do this through their use of Bayesian statistics and estimation of their state parameters. To this end, all of the state parameters must be continuous and have a Gaussian distribution [80].

A Kalman Filter takes in noisy measurements and uses these measurements along with previous information about the system to estimate the current states of the system. This estimate and the readings for the system are then compared to test their accuracies. The difference between them (or residual) is used to find the most likely correct value for the state using the error characteristics of the estimate and the readings respectively [81].

This concept can be seen pictorially in Figures 3.1 and 3.2. The way the prediction is calculated for the next estimate stage and the error associated with the estimate is adjusted to try to make it more accurate (more specifically lower the least-squares error) [82].

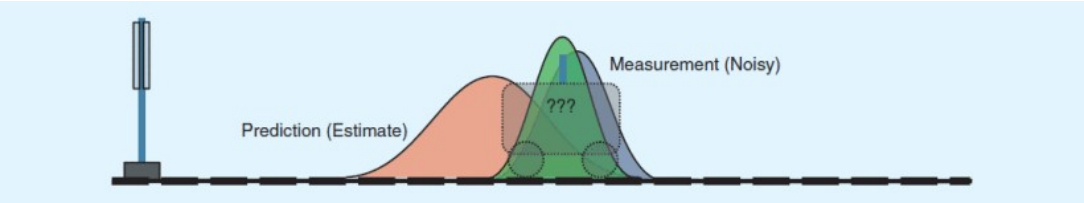

Figure 3.1: Overlaps of the Gaussian Probability Density Functions for the measurement and prediction and how they combine to form a more accurate state [80].

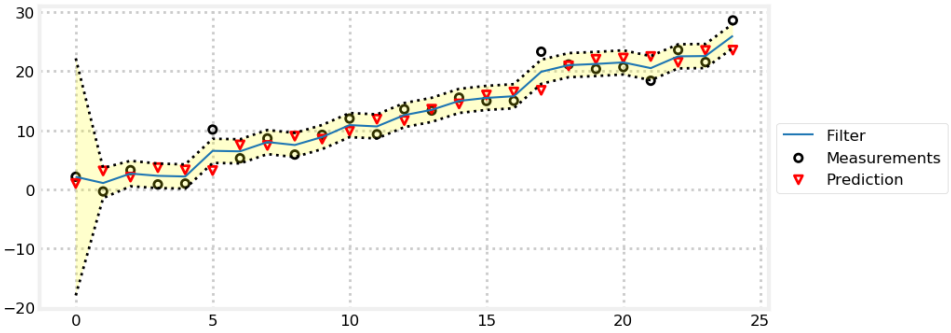

Figure 3.2: Plot of the prediction, measurement and least squares error region for a simulated Kalman Filter over 25 cycles [79].

The decision for how much to trust the reading versus the estimate is perhaps the most important factor in the design of the filter. This is because if the reading is given absolute priority the filter isn't doing anything and just tracking to its input. However, if the estimate is trusted too far it becomes a so-called smug filter where it can drift further from the truth with each update ignoring its sensor inputs. The exact value of these Kalman gains is dependant on both the sensors used and the known behaviour of the system being measured [79].

There are also different types of Kalman Filter with each being suited to a different task. The most common of these are the Linear Kalman Filter (KF) and Extended Kalman Filter (EKF) with the EKF using the KF to extend to non-linear problems. This works by assuming that the linearised dynamics are approximately equal to the non-linear dynamics for the time between update events.

The largest issue with the use of any Kalman Filter is that the filter may become unstable if the estimates and assumptions used to create it are not always true. Its therefore critically important that the system can sanitise known bad data to prevent this instability.

3.7 Controller Design

The controller implemented on the platform was only designed to test the efficacy of the platform design. To this end a state machine based controller was implemented.

Two different state machine controllers were used: one being used to test for hopping in one dimension, with the second controller used to test for hopping with a fixed body in two dimensions.

This controller was implemented on a Teensy 4 microcontroller. The use of a microcontroller allowed for direct interaction between the operating system for the robot and its peripherals.

3.8 Platform Validation and Testing

Testing of the platform was conducted in an incremental fashion, to reduce the chance of any errors in testing leading to catastrophic failure. A further benefit of this was a reduction in the challenge of debugging the system.

The first part of the system tested was the output of the sensor system. This was tested by moving the completed boom by hand and comparing the sensor outputs to where the boom was moved to. In addition to this the Kalman filter output was compared to the outputs of its own sensors to check for stability.

Once the sensor system was validated the motor was integrated. To do this the motor was fixed to the boom without the leg and fed a series of torque and position commands.

Following the motor validation the one dimensional vertical hopping tests were conducted. The outputs of these tests were compared to the simulations of the platform and the Vertical Agility metrics from other platforms [35]. This Vertical Agility metric was defined as:

$$VA = \frac{y_{max}}{t_{hop}} \tag{3.1}$$

Where y_{max} was the maximum hop height of the platform and t_{hop} was the time taken to complete a hop.

The final tests conducted were the forward hopping tests. These tests were conducted for both the highest speed stable gaits and the best single hop values. These results were again compared to the simulated data and make use of a custom horizontal agility metric. This metric was defined in two different ways with the first being a direct conversion from Vertical Agility maintaining unit parity while the second also made use of the final velocity as a scaling factor these equations can be seen in 3.2 below.

$$\begin{aligned} HA_1 &= \frac{x_{hop}}{t_{hop}} \\ HA_2 &= \frac{x_{hop}}{t_{hop}} \dot{x}_{hop} \end{aligned} \tag{3.2}$$

Chapter 4: Pneumatics Modelling and Actuator Selection

Pneumatic actuators have been in use for centuries due to their simplicity and efficacy. In modern times these actuators are still used due to their light weight, low cost and high power - all factors helpful in the design of legged robots.

In contradiction to the simplicity of their mode of operation, quantifying that operation is far more challenging. Unlike electrical actuators, pneumatic actuators are non-negligibly affected by the system they are attached to even if that system is oversized. These systems based characteristics can also be difficult to quantify, requiring the use of specialist tools such as flow meters to quantify losses (which add losses of their own).

When comparing the positive characteristics of pneumatic cylinders to the requirements for the knee actuator (discussed in section 3.3.2) it was decided to use pneumatic actuators for this joint as the properties of a pneumatic cylinder align to the actuator requirements for low mass and a large impulsive force output.

This chapter therefore proposes a scheme for the identification of the system parameters and their effect on the cylinder. In addition to this it proposes a reduced-order modeling scheme for the motion of a pneumatic cylinder.

4.1 Pneumatic System Configuration

A pneumatic system at minimum requires four parts: an accumulator, transmission pipes, control valve(s) and an actuator. In addition to this, a compressor is often used, however, the compressor operates before the system to fill the accumulator and does not effect the performance of other components outside of the peak accumulator pressure. The control valves used are often solenoid valves for switching between supply and atmospheric

pressure, though more complex variants may be found. Pressure regulators, throttle valves and other components are often used to achieve specific pressure or flow results.

The schematic of the pneumatic system used for testing can be seen in Figure 4.1 A below. In this system the, 10 bar, 5 cubic meter pneumatic supply system at the University of Cape Towns BISRU [1] Lab was used. This supply system was significantly oversized and therefore would not be a limiting factor in the system testing. The valve used for the initial testing was a *Pneumax 404-52* solenoid valve while the first cylinder tested was the *SMC C85N20-400*.

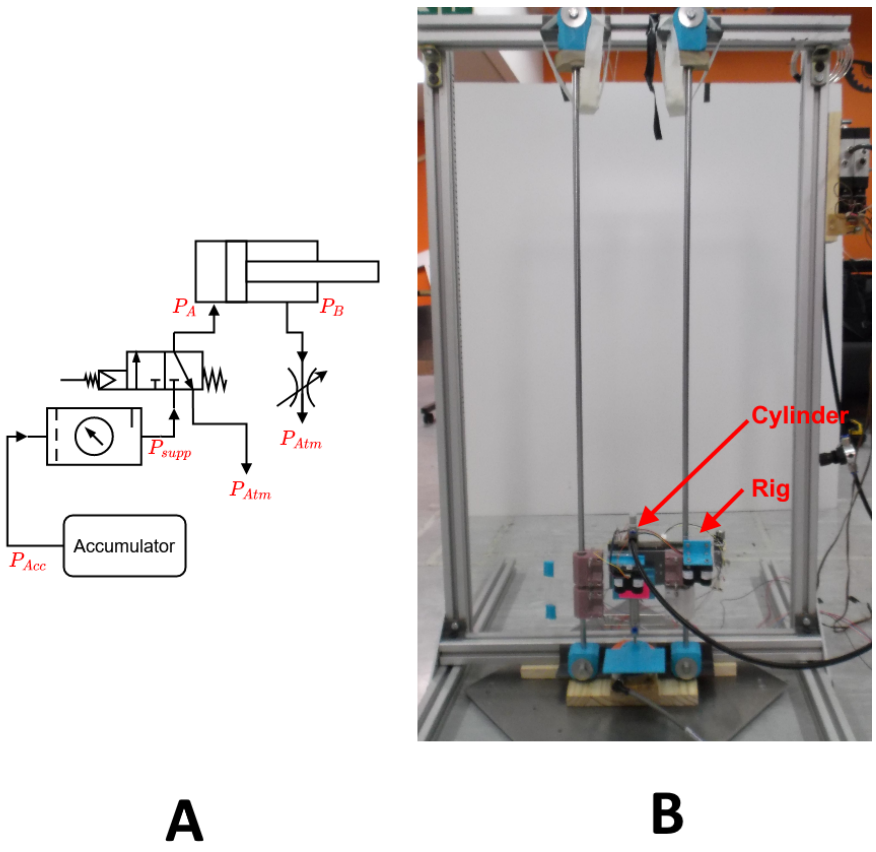

Figure 4.1: A: The pneumatic system architecture. B: the test rig used to test and validate the system.

In addition to the pneumatic system above, a linear rail constraint rig and measurement system were constructed, which can be seen in Figure 4.1 B. In addition to the linear rails, this system made use of a *Garmin Lidar Lite V3* Lidar unit to measure the position of the cylinder vertically and an *Optoforce OMD-45-FH-2000N* force sensor to measure the ground reaction force.

[1] Blast Impact Suitability Research Unit

4.2 Pneumatic Modelling

In order to create valid specifications for a cylinder to be used in a legged robotic platform, an accurate pneumatic model was required. In spite of this, the complexity of fluid dynamics can make an accurate model less viable for tasks where computational speed is a significant factor, such as on low power micro-controllers or in computationally expensive tasks like trajectory optimisation.

Due to these distinct advantages two different models were constructed and compared. The first made use of thermodynamic and fluid dynamic principals to accurately model the system. The second model, meanwhile, used a reduced-order model, matched to existing motion templates.

4.2.1 Rigid Body Dynamics

For the model of the system to be validated, a test rig was constructed with a pneumatic cylinder hopping vertically. This system had six main forces which acted on the two bodies of the cylinder rod and cylinder body. These forces being friction in the rails (F_{fRig}), friction in the cylinder (F_{fCyl}), gravity ($M_1 g$ and $M_2 g$), ground reaction force (F_{grx}), hard-stop force in the cylinder (F_{crx}) and finally the pneumatic force in the cylinder due to pressure (F_P).

The system was considered as two bodies to allow the relative motion of the cylinder and additionally to quantify the hard-stop contact force internal to the cylinder. These forces and where they act can be seen in Figure 4.2 below.

This allows for the net forces on the bodies to be defined as:

$$\begin{aligned} F_1 &= -F_{fRig}\hat{\dot{y}}_1 - M_1 g + F_p - F_{fCyl}\hat{\dot{l}}_{leg} - F_{HS} \\ F_2 &= -M_2 g - F_p + F_{fCyl}\hat{\dot{y}}_{21} + F_{HS} + F_{grx} \end{aligned} \tag{4.1}$$

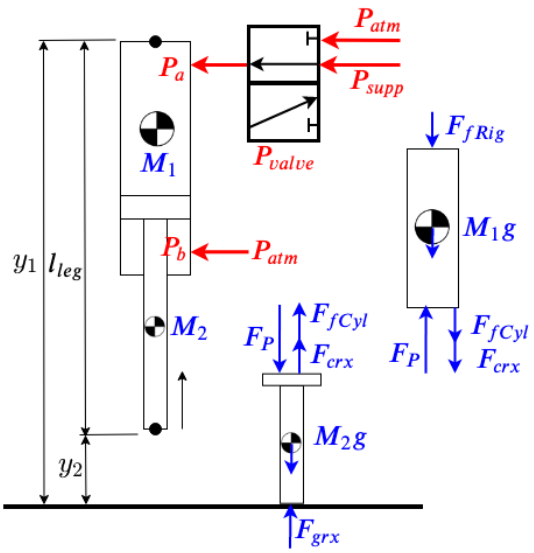

Figure 4.2: Diagram showing the relevant coordinates of the system. These include the height of the cylinder, y_1, the length of the cylinder, l_{leg}, and the relevant pressures. Free body diagrams for the body and rod of the cylinder can be seen on the right.

The contact forces were based on the soft contact model used by Celik and Piazza [83] and made use of a Heaviside step activation function based on the distance of the foot from the ground. This lead to the following system of equations for the ground contact:

$$F_{grx}(\delta, \dot{\delta}) = a\delta^3(1 + b\dot{\delta}) \tag{4.2}$$

$$\delta(y_2) = -y_2 H(-5y_2)$$

$$\dot{\delta}(y_2, \dot{y}_2) = -\dot{y}_2 H(-5y_2) \tag{4.3}$$

$$H(y) = \frac{1}{2} + \frac{1}{2}\tanh\frac{y}{s} \tag{4.4}$$

where a and b are constants for the force and δ and $\dot{\delta}$ are position and velocity functions adjusted through the use of the Heaviside function, H. This Heaviside function makes use of an activation value of s experimentally derived by Celik.

The hard-stop forces on the cylinder were derived similarly, however, in this case they were defined based on the relative length (l_B) of the cylinder and its derivative as:

$$\begin{aligned} l_B &= 2L_{stoke} - (y_1 - y_2) \\ \dot{l}_B &= \dot{y}_2 - \dot{y}_1 \end{aligned} \tag{4.5}$$

The values for δ_l and $\dot{\delta}_l$ were then found as previously using l_B and $\dot{l}_B$ with the cylinder reaction force being:

$$F_{HS}(\delta_l, \dot{\delta}_l) = c\delta_l^3(1 - d\dot{\delta}_l) \tag{4.6}$$

By combining equations 4.1, 4.2 and 4.6 and Newton's second law of motion the system could be solved using any numerical time based solver.

4.2.2 Fluid Dynamics Pneumatic Cylinder Model

The fluid dynamics model describes the pressure in chambers A and B of the cylinder (P_a and P_b respectively) while including the various flow and orifice losses in the system. This initially required the velocity of the fluid to be found through the use of the formula for pipe losses for fully developed laminar flow [84]:

$$\Delta P = \frac{64}{Re}\frac{L}{D}\frac{1}{2}\nu^2 + K\frac{1}{2}\rho\nu^2 \tag{4.7}$$

with ΔP being the difference between P_a and the supply pressure for control volume A and P_b and the atmosphere for control volume B. The loss factor for the system $K \approx 10$ was found empirically through testing the hop up testing described in section 4.3.1. The above equation was then solved for flow velocity (ν) using the positive quadratic solution, as the direction of the flow was known to be positive during the takeoff. Within this equation, ρ was dependant on the temperature (T) as another time-variant parameter. The temperature of the control volumes were calculated using an ideal gas assumption [85] as follows:

$$\begin{aligned} T_a &= T_{stp}^{\frac{\gamma}{\gamma-1}}\left(\frac{P_a}{P_{supp}}\right)^{\frac{\gamma-1}{\gamma}} \\ T_b &= T_{stp}^{\frac{\gamma}{\gamma-1}}\left(\frac{P_b}{P_{atm}}\right)^{\frac{\gamma-1}{\gamma}} \end{aligned} \tag{4.8}$$

$$\rho = \frac{nP}{RT}, \tag{4.9}$$

where γ was the isentropic expansion ratio $= \frac{C_p}{C_v}$, R was the gas constant of air and n was the molar mass of air. Using the ideal gas law the mass of the air in either control volume could be defined with its derivative as:

$$\begin{aligned} M_{air,i} &= \frac{P_i V_i}{R T_i} \\ \dot{m}_{air,i} &= \frac{\dot{P}_i V_i + \dot{V}_i P_i}{R T_i}, \end{aligned} \tag{4.10}$$

where V_i - the control volume - was based on the volume of each respective chamber of the cylinder, and, along with its derivative $\dot{V}_i$, were known from the mechanics of the system. Due to the short duration of the hop, and large pressure changes in the system, an adiabatic model would be most accurate. However, for the sake of simplicity an isothermal model was tested in simulation. Using this formulation of the mass flow rate and the velocity of the fluid found earlier, the rate of change of pressure could be calculated as:

$$\dot{P} = \frac{\nu R T \rho A_{pipe} - \dot{V} P}{V}. \tag{4.11}$$

The pressure could be converted to a force using the known area of the pneumatic cylinder. This area is asymmetrical between control volumes A and B as the B side has a reduced area due to the cylinder rod.

These time dependant equations, (4.1) and (4.11), were then solved in Matlab/Simulink (using the ODE113 solver).

4.2.3 Reduced-Order Pneumatic Cylinder Model

The aforementioned fluid dynamics model captured the complete behaviour of the pneumatic cylinder, and while it was solvable with traditional computationally techniques, it contained some numerically challenging aspects reducing it applicability to low computational power use cases.

However, it was hypothesised that a simple force-damper model could be used as a reduced-order approximation for this system. This approximation was selected as it could be helpful as a control template for the motion of the cylinder under excitation. This approximation was valid due to the fact that the cylinder outputs a force inversely

proportional to its speed which tends to a maximum steady-state velocity with stroke length.

Thus a new model for F_P can be defined as:

$$F_{Papprox} = P_{supply}A_a - (\dot{y}_2 - \dot{y}_1)C, \tag{4.12}$$

where C was a damping constant experimentally derived for the system based on the peak output force and the steady-state velocity. This steady-state velocity was found experimentally using the testing seen in Section 4.3.1, while the force F_P was assumed to activate immediately and was based on the pressure of the test and cylinder bore used.

The simplicity of this model made it computationally efficient while also leaning into the template approach to modelling.

4.3 Testing and Model Validation

Testing was conducted to evaluate the parameters of the system and validate the model against the system. This testing was broken into hop up tests that were done prior to modelling to establish the system parameters and continuous testing to validate the model.

4.3.1 Hop Up Testing

For this test, the closed cylinder was started stationary on the ground while connected to the vertical rails test rig. This test was controlled by an embedded system which logged to an external PC - the architecture of which can be seen in Figure 4.3.

The state of the solenoid valve was tied to a button with the valve allowing compressed air to flow from the compressor into control volume A while the button was held and this control volume being vented to atmosphere when the button was released. When the button was pressed the Arduino would start logging position data at a rate of 500 Hz. This height data was synced to the force data from the Optoforce (logged at a rate of

1 kHz) as it came into the system master PC where it was saved to text files for later post processing.

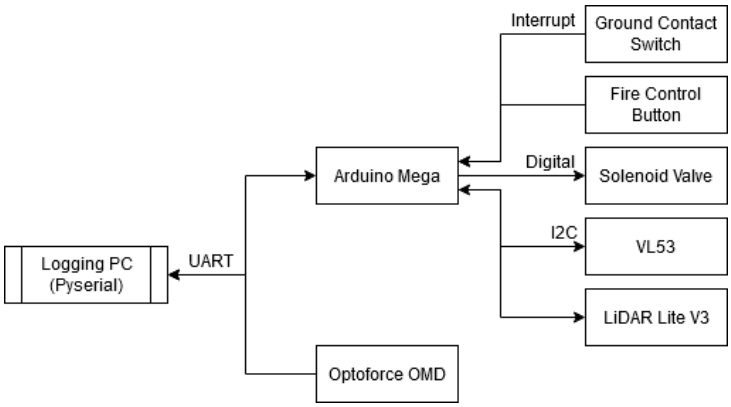

Figure 4.3: System Architecture used for the testing of cylinders.

Due to the noise characteristics of the height sensors, data post-processing was required. The slow data rate of the *VL53* sensor (30 Hz) was too low to be useful, while the *LiDAR Lite V3* had a relatively low accuracy of ± 2.5 cm. For this reason post-processing the motion of the cylinder was required. This post processing was done with a piece-wise polynomial approach which can be seen in Figure 4.4.

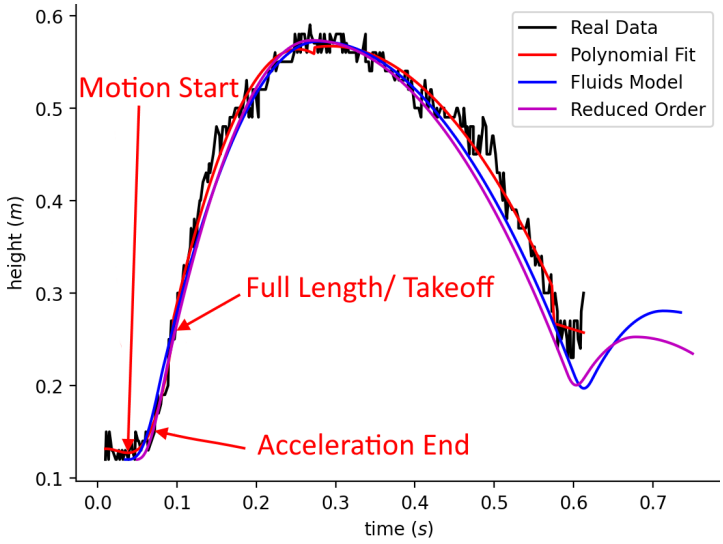

Figure 4.4: Comparison of the different system models. Real data is the raw output from the LiDAR, which was curve fit to generate the Polynomial fit. The reduced order model is the model described in Section 4.2.3 while Fluids model is the model described in 4.2.2.

The motion of the cylinder was split into four characteristic parts: acceleration, steady-state, ballistic up and ballistic down. These motions were selected based on their appear-

ance in the raw data acquired and the order of polynomial expression for each part being based on the best fit and the known forces on the platform during that section. The first motion was set as a 2nd order polynomial, as this was the best fit without over-fitting. The steady-state section was approximated as a 1st order polynomial to evaluate steady-state parameters extracted from this line. The up and down ballistic segments were both approximated as 2nd order polynomials as the known forces acting on the system were gravity and friction. These motions were split as the friction changed direction with the motion of the test rig.

This test was repeated five times for each of the two cylinders tested, a *SMC C85N20-400* with a bore of 20 mm and a *Festo DSNU-16-125-PPV-A* with bore of 16 mm. These results could reasonably be expanded to 25 mm and 12 mm bores as those bores have the same port sizing and therefore the same orifice flow restriction as in the 20 mm and 16 mm bores respectively.

4.3.2 Continuous Hopping Tests

The continuous hopping tests were done to validate the force damper model of the cylinder against an untested scenario. To this end the model was used to generate preset trajectories. This scheme used different contact times to test the ability of the cylinder to hop to different heights. This was then implemented using the foot contact switch and a delay from the micro-controller. Figure 4.5 shows the output of continuous hopping in both filtered and raw states. This filtering was done both with averaging the data across hops (referred to as "Averaged Real Data") and a Polynomial fit method ("Polynomial Approximation") as described previously. The real data ("Test Data") was then compared to the output of a Trajectory Optimisation based simulation using the reduced-order model (referred to as "Optimisation Trajectory") which was run prior to the physical system testing. This trajecory optimisation was run by Dr Callen Fisher and further information regarding it can be found in his dissertation [86].

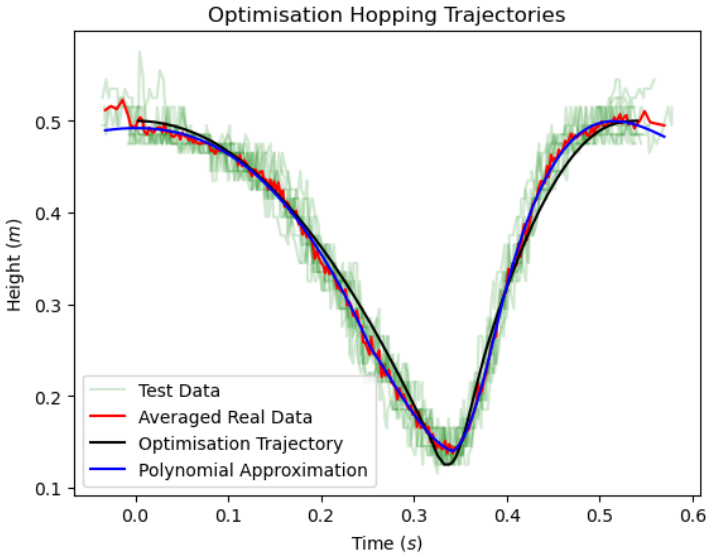

Figure 4.5: Comparison of continuous hopping data, its linearisation and its anticipated trajectory.

Figure 4.6 depicts the output variance in hop height obtained by altering the delay between ground contact and the firing of the cylinder. This delay was swept from zero until it could be seen that the cylinder was fully collapsed and had a short delay while in the collapse state for the pressure in the cylinder to reach its equilibrium.

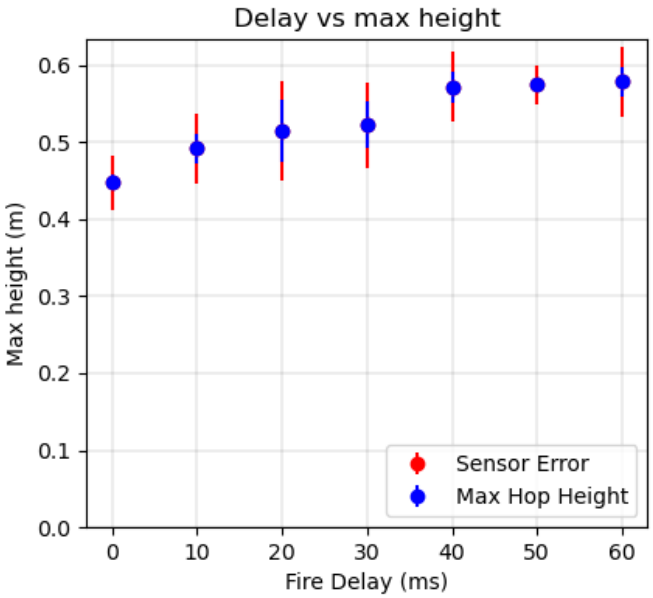

Figure 4.6: Variance in hop height based on based on fire delay.

4.4 Summary

The tests conducted successfully validated the use of a pneumatic cylinder as an active actuator for legged robots rather than its use as a spring exciter system traditionally seen in the literature [46]. The tests also validated a scheme for controlling hop height of the cylinder based on the activation position of the cylinder.

Chapter 5: Platform Design

This chapter details the process through which the mechanical design of the robot was conducted and the choices involved in developing it. The chapter begins with the development of the specifications and the selection of actuators, before moving on to the design of the mechanical parts and their acceptance testing.

5.1 Requirements and Specifications

One of the original requirements placed on the project was the use of a pneumatic cylinder. This actuator would be used for the lower leg actuator due to its low cost, light weight and high power output. This differed from the hip actuator with its need for accurate position control of the joint. This difference in requirement forced the selection of a DC motor for this joint to meet its demands. A brushless DC motor was selected over a stepper or servo-motor as latter has an inconsistent torque output and high weight, while the former makes use of large gear reductions that can be damaged by the shock loading implicit in legged robots. These two actuators were the main specification for the platform and would be used to inform the rest of the design.

The requirements for the actuators are developed in the sections that follow with each section building from the choices made in the previous sections. In addition to this, the general mechanical specifications were based on those developed in Table 3.1. The predominant requirements emerging from this being that the system is as light as possible while also being sufficiently robust to handle the repeated shock loading inherent to legged robots.

5.2 Motor Specification

The motor specification was based around two factors, firstly the choice to make use of a Quasi-Direct drive system and secondly purchasing the motor from either T-motor or Maxon. The choice of the Quasi-direct drive system was due to its high torque outputs these systems achieve without requiring elastic elements to protect the gearbox [87]. The supplier limitation was because these suppliers had previous working relationships with the research group, and therefore additional accessories for motors from these distributors were on hand. Both suppliers also sold units with integrated motors and gearboxes simplifying the drive train and reducing both cost and weight.

After evaluations of both suppliers product lines, the T-Motor A80 series of motors were selected. This series was selected as these motors had higher power to weight ratios and higher numbers of poles than their Maxon counterparts and included gearboxes, unlike the rest of T-Motors range. This series consisted of two products at the time of selection: the A80-6 and A80-9 motors, the properties of which can be seen in Table 5.1.

	Max Torque (Nm)	Max Speed (rpm)	Weight (g)	Cost ($)
A80-6 [88]	12	425	462	207
A80-9 [89]	18	285	555	227

Table 5.1: Motor properties for the T-Motor A80 series.

There were two critical requirements for the specification of the motor, both of these being used to generate scenarios to test in simulation to select the motor. The first requirement was that it should be capable of repositioning the leg during the aerial phase of a hop, while the second, was that the motor should move the body in its stance phase at a similar speed as the horizontal component of the cylinder's motion. To test the first requirement, several assumptions were made to bound the problem:

1. The maximum required reposition would be 120°,
2. The largest cylinder selected would have a bore of 20mm and a stroke of 200mm,

3. The inertia of the cylinders rod support would be the same as the inertia of the cylinder,

4. An optimal controller could accelerate and decelerate the rotation of the cylinder in the same amount of time applying maximum power on the system continuously.

This set of constraints was used to construct the test giving the output seen in Figure 5.1 below. This test was conducted using an ideal motor model where maximum (stall) torque is provided when the motor is stationary and maximum speed at no-load. The equation of motion for the system were based on Newtons second law for rotation and can be seen in Appendix A.1. This equation was solved for each point using an ODE45 solver in Matlab Simulink. The time taken to reposition (seen in the z-axis of the graph) should be minimised as this would allow for more aggressive acceleration steps as less vertical height would be required to reposition the leg, however, any parameter set that took less than 0.15 s was considered viable. For this graph it could be seen that this repositioning criteria was extremely easy to fulfil with both of the T-Motor motors easily surpassing the minimum speed and torque requirements from this test case.

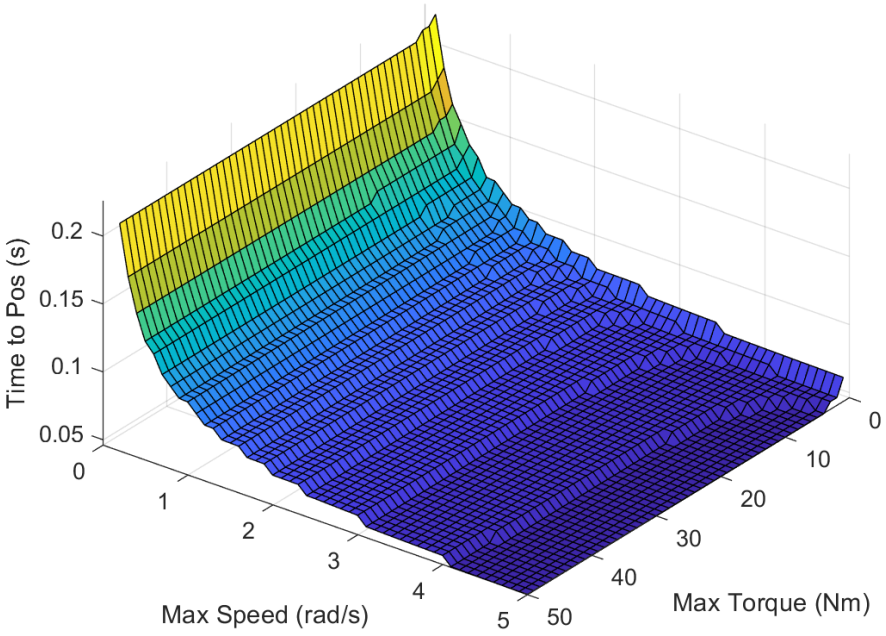

Figure 5.1: Time to rotate through 120 degrees for a 20mm Bore 200mm Pneumatic Cylinder as a function of maximum torque and speed, lower time values are better.

The second simulation test conducted was to ensure that the system could reposition itself on the ground at a rate similar to the horizontal speed of the cylinder, therefore meeting the second requirement.

This test was conducted with the cylinder starting with an assumed initial velocity of 2.15 m/s, furthermore, the cylinder was fully extended and fully vented to atmosphere. This velocity was chosen based on the maximum velocities for different cylinder from the model described previously in section 4.2. The angle of the cylinder at the start of the test was 60° forward from vertical; when the test began maximum motor power was applied to reposition it to 60° behind vertical where the simulation was stopped. A motor was considered a viable option if it could do this stance phase under motor power alone with the average velocity of the body of the platform being greater than its initial 2.15 m/s value. The equations of motion for this simulation were developed using Lagrangian Mechanics and are presented in Appendix A.2. The simulation was then run in Simulink, producing the results seen in Figure 5.2.

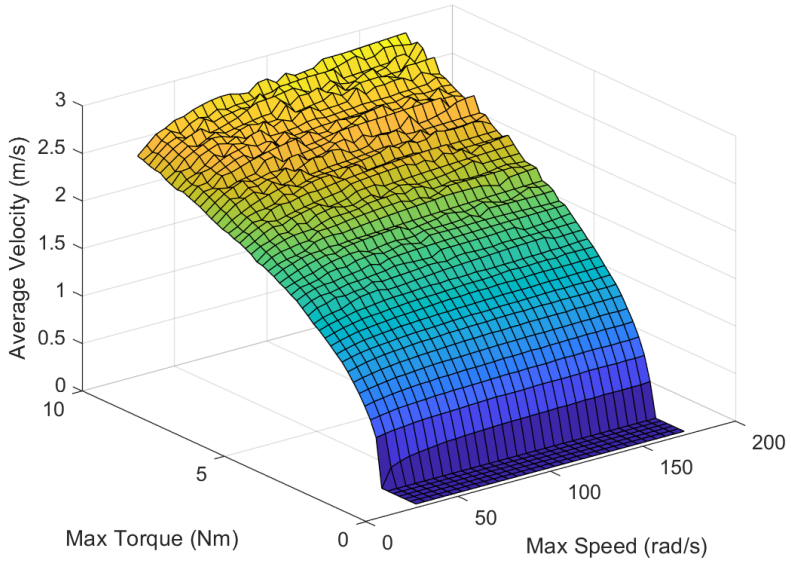

Figure 5.2: Average velocity of the body of the robot during stance under motor power only, any value greater than 2.15m/s on the z axis was considered viable with higher scores being better.

From Figures 5.1 and 5.2 and the motor properties in Table 5.1 above it can be seen that both the T-Motor*A80-6* and *A80-9* largely exceeded the minimum specification. It was therefore decided to use the *A80-6* as it was less expensive and lighter.

5.3 Pneumatic Cylinder Specification

For robots, the metric of Vertical Agility (VA) is often used as a proxy for how well the robot will perform in its manoeuvres [90]. However, as it is a linear metric being used to describe a planar motion it can be biased in favour of certain designs. To avoid this bias, and specify a pneumatic cylinder giving well rounded performance, a custom Horizontal Agility (HA) metric was formulated. These metrics were required due to the antagonistic relationship between the force output of the cylinder and its maximum speed as larger bore cylinders have greater force outputs but do so at the cost of the speed of the cylinder - this antagonistic relationship therefore implies the existence of some optimal cylinder for the design.

The following sections detail the manner in which these simulations were conducted and their outcomes before selecting a cylinder to use on the platform. Furthermore, although a single double acting cylinder was specified for the design due to its reduction in modelling complexity, additional simulations for a double link design were conducted and were compared to the single link design for completeness sake.

5.3.1 Vertical Agility Simulations

Vertical Agility is a useful metric for the design of robots as it's relatively easy and computationally inexpensive to simulate. These properties make it ideal for use in specification of actuators for robots. The metric of Vertical Agility is defined as:

$$VA = \frac{y_{max}}{t_{stance} + t_{hop}} \tag{5.1}$$

Where y_{max} is the maximum hop height, and $t_{stance} + t_{hop}$ the total amount of time it takes to complete one hop cycle.

Vertical agility simulations were run for both a single-cylinder and a double link hopper (seen in Figure 5.5). In these simulations the foot and the body were both constrained on prismatic joints to only allow them to move vertically. This was done to ensure that the line of action of the virtual leg remained vertical and through the body's centre of mass -

therefore removing any effect of a motor making the actuator selections independent and maintain modularity.

5.3.1.1 Single Cylinder VA

The first simulation run was for the Vertical Agility of a single prismatically acting cylinder. This simulation used a cylinder mass based on its size from Festo's DSNU data sheet along with a mass scaled to the approximate mass of a support that would be required based on the stroke of the cylinder. In addition to the cylinder and support masses, an approximate body mass was included to represent the mass of the motor and body. The boom mass was excluded from these simulations as the system's performance should be independent of its support structure.

Using these parameters, a simulation was constructed in Matlab's Simulink Multibody using cylinders with bores from 12 mm to 25 mm and stroke lengths from 0.1 m to 0.2 m. These size constraints were implemented as they were commonly available for Festo's DSNU type cylinders. This type of cylinder was selected as the round DSNU cylinders were significantly lighter than its ISO cylinder counterparts. The cylinder's actuation properties were modelled based on the fluid dynamics model described in Section 4.2.2. The results of these simulations can be seen in Figures 5.3 and 5.4:

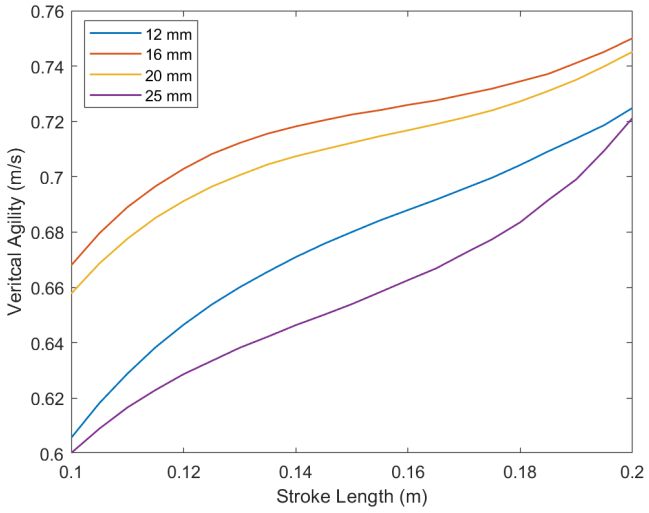

Figure 5.3: Vertical Agility of the single cylinder system vs stroke length. The cylinder bore size each line represents is shown in the legend in the upper left of the figure.

In Figure 5.3 above it can be seen that cylinders with longer strokes were favoured for the Vertical Agility simulation. These higher VA scores for longer cylinders occurred despite their weight penalty and was observed to be due to the higher velocities these systems reached while the greater mass also resulted in shorter hops and subsequently greater hopping frequencies. Additionally, the data showed that $16mm$ bore cylinders were the optimal choice for the system as they outperformed all other bore sizes for every stroke length tested.

Moreover, from Figure 5.4 it could be seen that the maximum hop height occurred at a stroke length of $0.125\ m$. This was due to this point being the optimal trade-off between the mass of the system and the maximum velocity achieved by the cylinder.

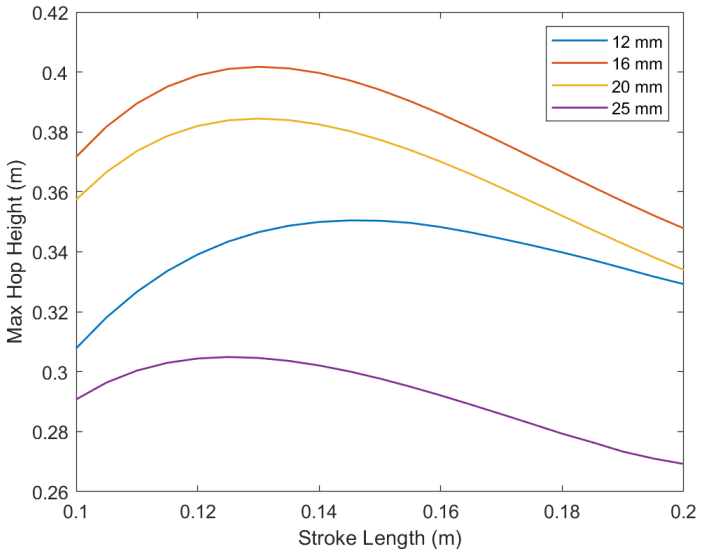

Figure 5.4: Hop Height vs Stroke Length for various cylinders. The bore of the cylinder each line represents is shown in the legend in the upper right of the figure.

5.3.1.2 Double Link VA

The Double Link system was defined as a system with two rigid links with a pivot between them. A pneumatic cylinder was attached to the two links through revolute joints at each end of the cylinder. This completed leg was then attached to the body through an additional revolute joint at the end of the first link. The geometry of the platform was defined as follows in Figure 5.5:

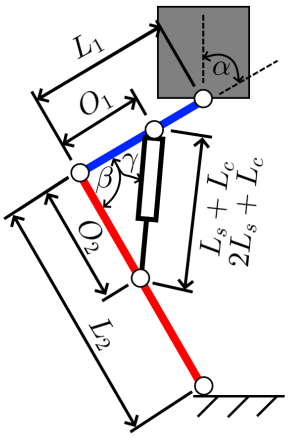

Figure 5.5: Double Link design configuration. L_1 and L_2 comprise the upper and lower links while O_1 and O_2 are the respective offsets. L_s is the stroke length while L_c is the additional offset length for the cylinder, the length of the cylinder varies from $L_s + L_c$ when closed to $2L_s + L_c$ when open.

Using the above model, both the point where L_1 meets the body and the foot at the end of L_2 were constrained, only allowing for vertical motion of these points. This was done to remove the motor dynamics from the simulation while still allowing a vertical hop. This motor-free test was desirable as it gave an initial point of comparison between the double link and single cylinder systems using only the power of their respective cylinders.

Due to the high number of possible configurations for the double link system, it was decided to run initial simulations as a parameter sweep with the final simulation being done as a Monte Carlo simulation [45] [91]. The reasons to employ Monte Carlo methods were:

- the entirely unknown and complex relation of the configuration of the system and its Vertical Agility,
- the narrow margin between valid and invalid configurations in-terms of ability to move and geometrically valid configurations
- to avoid biasing the data set towards configurations that seem more likely to work on an intuitive level.
- the functionally infinite possible number of configurations for the platform making a grid search impractical.

This Monte Carlo simulations randomised the lengths of the links L_1 and L_2 while scaling the bounds of these lengths based on the stroke length of the cylinder. Additionally, the offsets for the cylinder mounting O_1 and O_2 were set as randomised scaling factors based on their respective link lengths. The final random variable was the stroke length which was set as a multiple of $5mm$ between the bounds of $0.05m$ and $0.2m$. Each of the Monte Carlo variables was set by an individual random seed to ensure that the geometry was fully decoupled.

The other geometries in the system were then solved for based on the Monte Carlo variables (L_1, L_2, O_1, O_2 and L_s). These configurations were disregarded if they were found to not be geometrically feasible.

Throughout the process, the data was plotted periodically and the bounds on the random Monte Carlo variables were tightened to try to find the optimal solution. An intermediary plot can be seen Figure 5.6 below. This was an early plot where only fixed values of L_2/L_1 where used to try establish is any strong trend emerged and to try limit the scope of these early simulations.

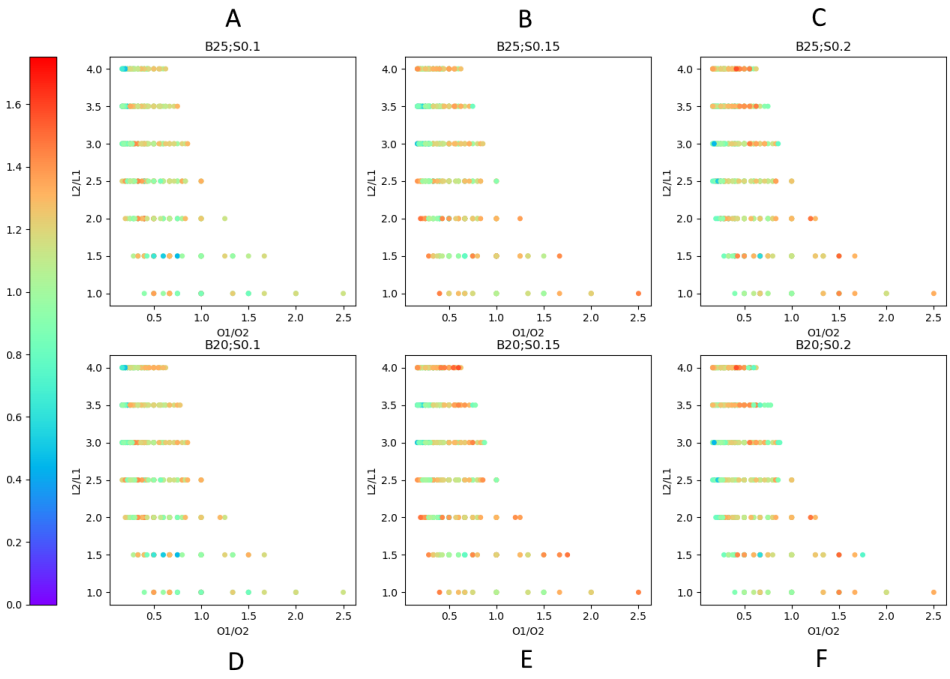

Figure 5.6: Double Link VA for Bores of 25mm (A-C) and 20mm (D-E). Stroke lengths for the cylinders of 0.1m (A,D), 0.15m(B,E) and 0.2m(C,F). Each plot is depicted as L_2/L_1 vs O_1/O_2, while colour of the point depicts its VA score with red scores being better and violet being worse.

From plots above the best simulation result could be seen to be a bore of 25mm and a stroke of 200mm. In addition to this visual analysis regression calculations were run on the data sets for all possible permutations of randomised variables to find a correlation between the randomised variables and the Vertical Agility score they produced. This was done due to the seemly random distribution of good configurations.

These regressions were then used to further reduce the bounds on the random variables for the simulations. To calculate these python was used to compute the regressions between the vertical agility score and either single parameters (such as L_1), or derived combinations of these parameters (such as $\frac{L_2}{O_2}$). This calculation was run for every single parameter as well as every permutation of two combined parameters. The strongest correlations found and their values were as follows:

$$r_{L2/O1} = -0.706$$

$$r_{L2/O2} = -0.633$$

$$r_{O1*L1} = 0.508$$

The final Monte Carlo simulation was run for 84000 seed configurations and the final simulation data can be seen in Figure 5.7 below. In the plot of $\frac{L_2}{L_1}$ vs $\frac{O_1}{O_2}$ (Figure 5.7-B) a Pareto front could be observed showing that there was an ideal, but not optimisable, area on the edge of the simulated data.

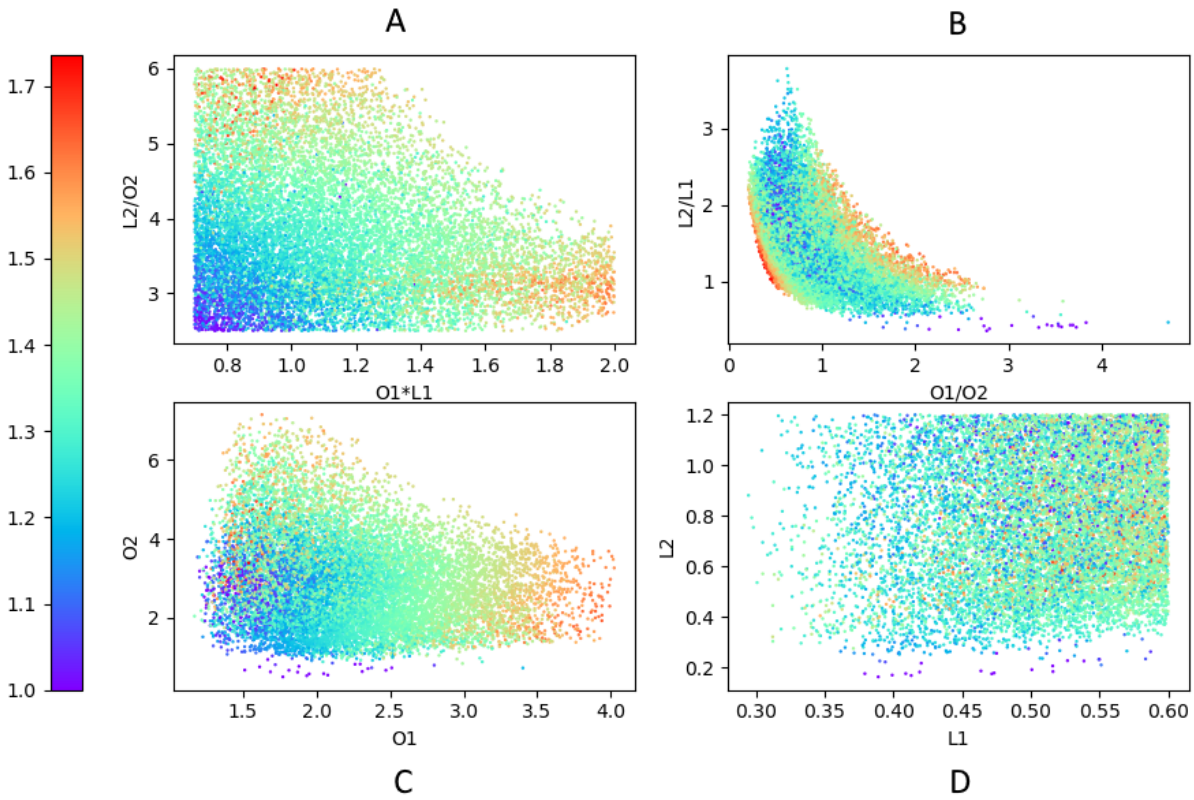

Figure 5.7: Double Link VA for Bores of 20 and 25mm.

5.3.2 Horizontal Agility

From the layout of the system (especially in the single-cylinder case), it could be deduced that the Vertical Agility metric is unfairly harsh on the robot. This is due to the fact that the leg could only make use of half of its actuators and was therefore being seen as significantly under-powered. Due to this, a new metric was proposed. This metric, referred to as Horizontal Agility (HA), would be formulated in two ways, denoted as HA_1 and HA_2 with HA_1 being a direct conversion of Vertical Agility to the Horizontal and thus maintained unit parity. HA_2 added an additional term to try balance in motor contributions. HA_1 was defined as:

$$HA_1 = \frac{x_{hop}}{t_{stance} + t_{hop}} \tag{5.2}$$

While HA_2 was defined as:

$$HA_2 = \frac{x_{hop}}{t_{stance} + t_{hop}} V_{Xlaunch} \tag{5.3}$$

To test this a hop-forward from a stationary start was conducted. This gait cycle can be seen in Figure 5.8 below with the phases of this motion described following it.

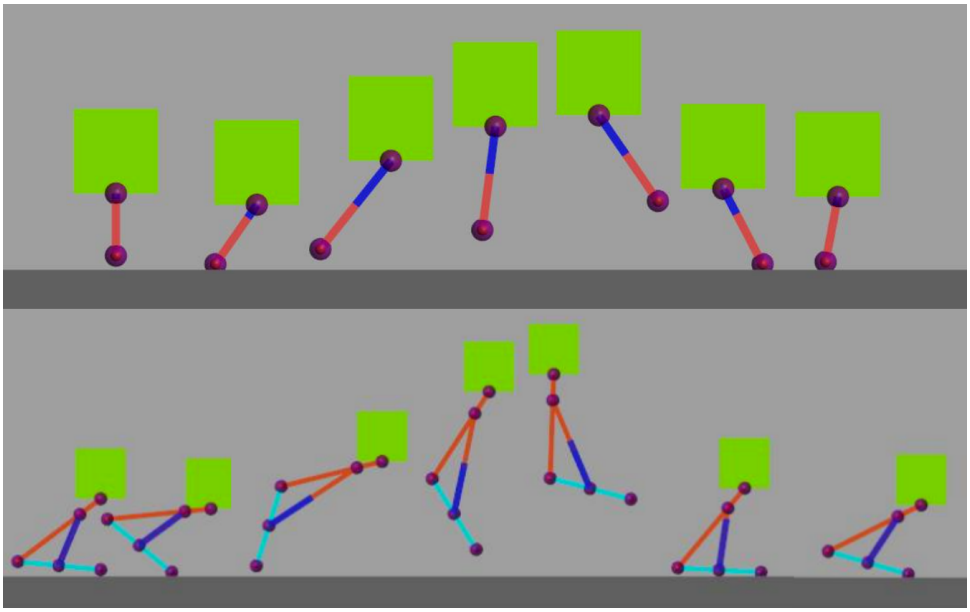

Figure 5.8: Full Gait Cycle for both the Single cylinder and Double Link Systems. Spacing of the motion is not to scale and has been adjusted for clarity.

This gait contained six distinct phases for its motion. These were as follows:

1. Start with the cylinder in its closed position and the virtual leg vertical
2. Rotate the cylinder to the desired launch angle using the motor in position control mode
3. Fire the cylinder
4. Position control to the landing angle (the launch angle flipped across the vertical)
5. On touchdown apply maximum torque till vertical
6. Position control back to launch angle

To implement this gait cycle, a state machine based controller was used with four sequential states. The XML diagram of this controller can be seen in Figure 5.9 below:

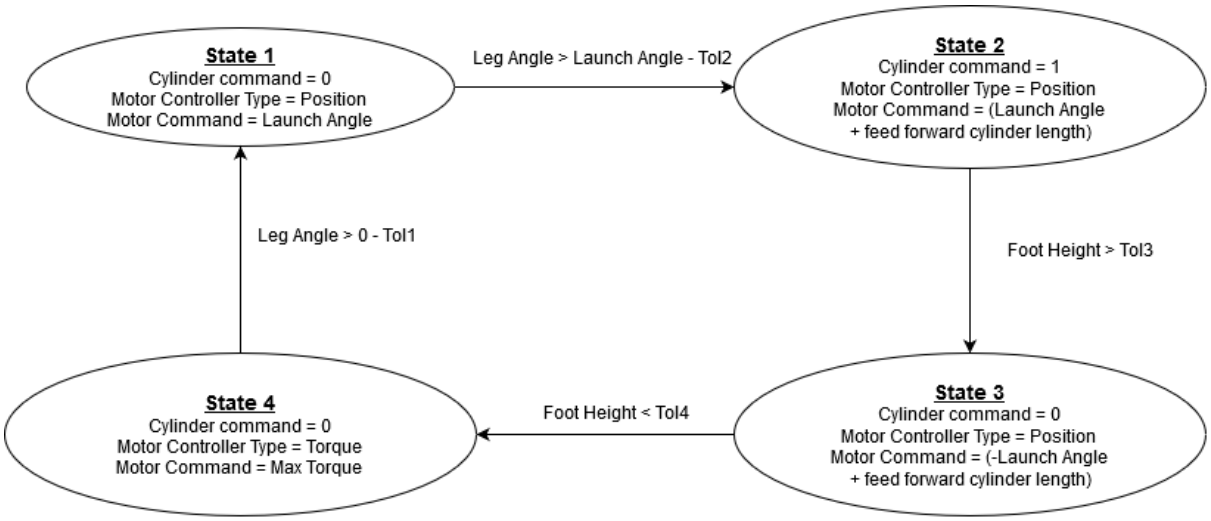

Figure 5.9: State machine controller for horizontal hopping.

The motor used in the simulation was the T-Motor A80-6 selected previously while the controller used by the state machine controller was the same as the one used by the ODrive motor controller [92]. The gain values for the PID controller's position control loop were set for each test based on the inertia of the leg configuration currently being tested.

In the case of the double link leg, a feed-forward position term was added to the position command from the state machine controller. This was due to the change in the angle of the virtual leg as the cylinder expanded. The feed-forward term allowed for the position control of link 1 to control for the virtual leg angle rather than the angle of link 1.

The simulation was stopped on the transition from state 4 to state 1 as only the first hop was considered of interest. If a simulation timed-out (3 seconds) without reaching state 4 it was considered to have been a failure and was given an HA score of 0. This frequently occurred as the system either didn't have enough power or slipped during takeoff in state 2. Both of these effects lead to a poor launch and the system failing to get high enough off the ground to transition to state 3.

5.3.2.1 Single cylinder HA

These Horizontal Agility simulations were run as a parameter sweep for the single cylinder case. This testing was for cylinders with bores from 16 mm to 25 mm, strokes from

100 mm to 200 mm and launch angles from 10 ° to 40 °. The results of these simulations can be seen in Figures 5.10 and 5.11 below for HA_1 and HA_2 respectively, while Figure 5.12 displayed the hopping distance for each test case.

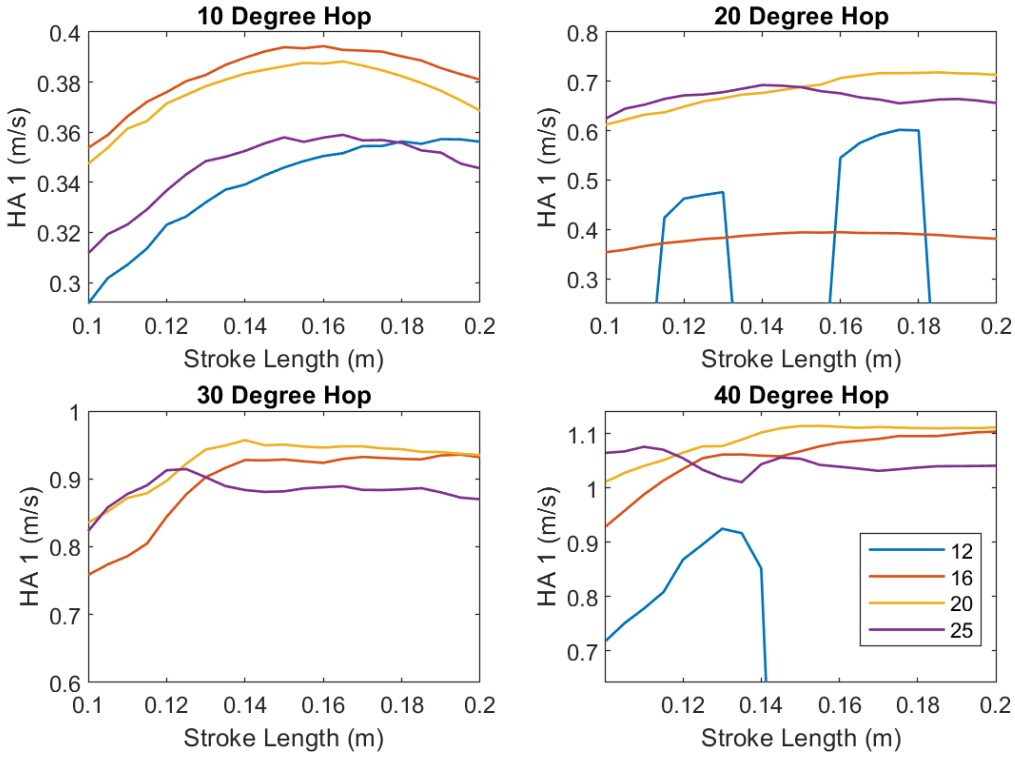

Figure 5.10: HA1 for the single cylinder vs stroke length.

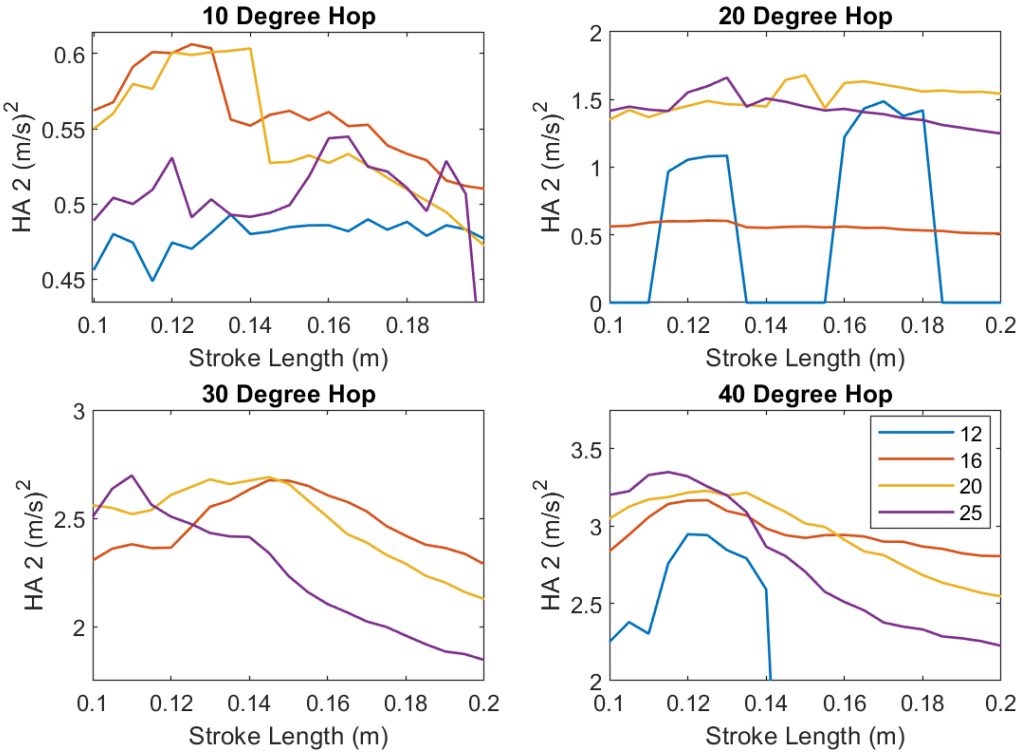

Figure 5.11: HA2 for the single cylinder vs stroke length.

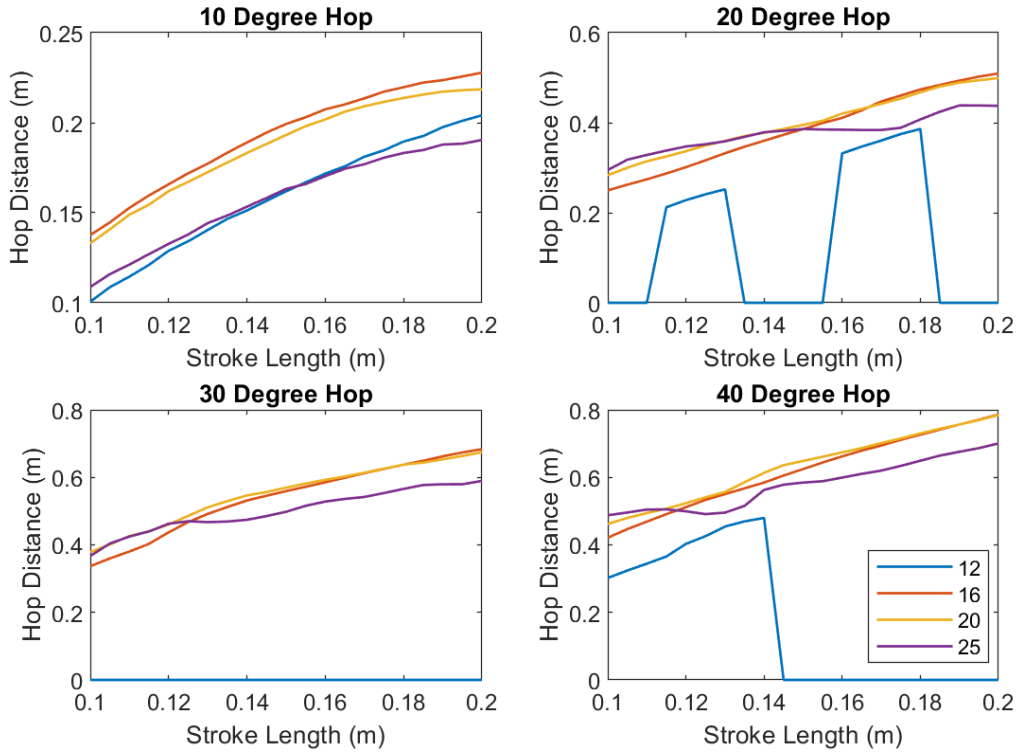

Figure 5.12: Hopping distance for the single cylinder vs stroke length.

These results display very different prioritisation to the Vertical Agility simulations seen previously. In the VA simulations, longer cylinders performed better without exception. This result did not transfer to the HA simulations with both HA_1 and HA_2 displaying local maxima in the 120 mm – 160 mm range depending on the test. This test case also did not provide a universally optimal cylinder size option as both the 16 mm and 20 mm cylinder performed well with the better choice being dependant on the test, launch angle and stroke.

5.3.2.2 Double Link HA

For the Horizontal Agility analysis, the simulation began as a Monte Carlo Simulation. This was done for similar reasons and with a similar methodology to the approach in the Vertical Agility simulations. The original set of simulations was run for 25000 valid configurations, however, from those seed 55.4% were failed simulations due to not completing a full gait cycle. Of these failed simulations the 25 mm bore failed the most frequently followed by the 16 mm bore. These two failed the at a higher rate compared to the 20 mm due to their low top speed (in the case of the 25 mm bore) and low force outputs (in the case of the 16 mm bore). The results of this simulation can be seen in Figure 5.13.

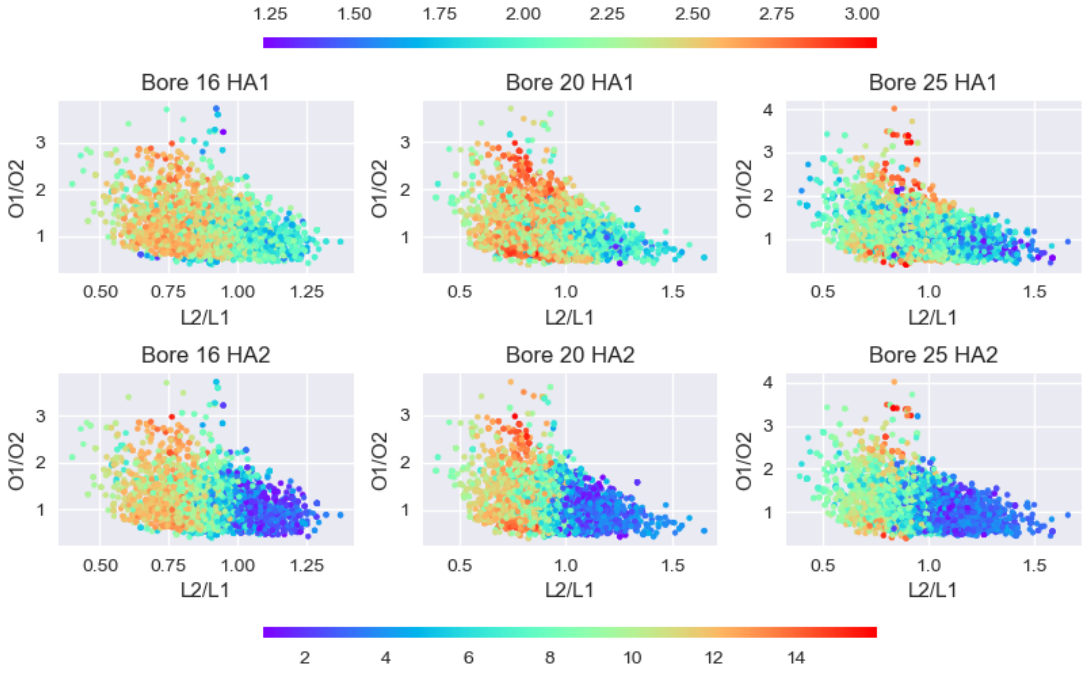

Figure 5.13: Horizontal Agility plots for the initial double link testing.

From this initial simulation set, the data was normalised by placing it into bins according to linkage length and offset and averaging the contents of the bin. This was done to find the best performing robust configuration. Robustness should be prioritised over some optimal point as this provides some outlier rejection for configurations that perform very well under these theoretic conditions but are optimised to the simulation, meaning that real-world effects might cause failure. The results of this normalised plot can be seen in Figure 5.14 below:

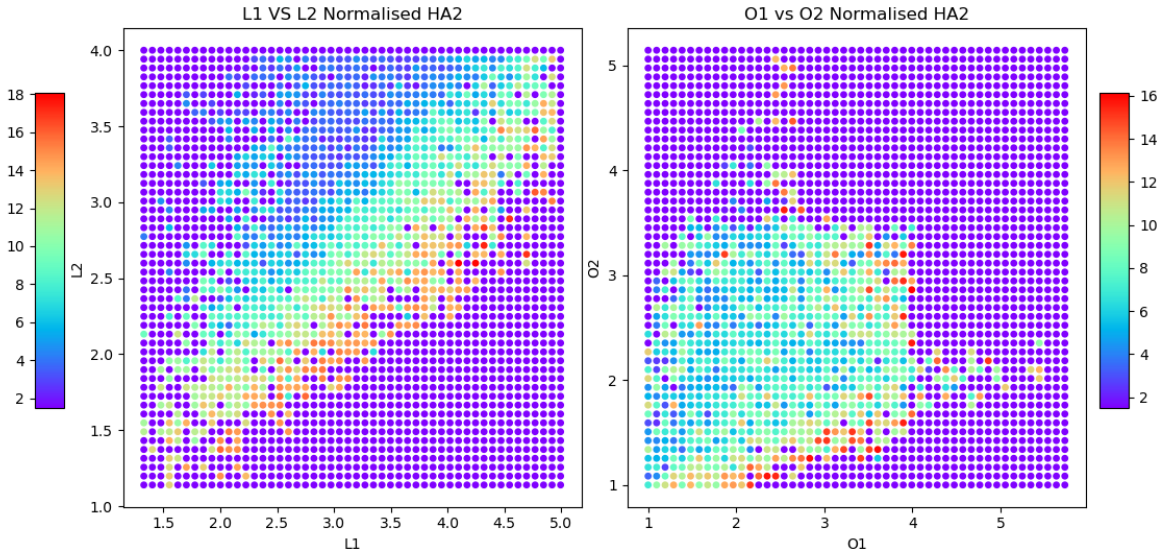

Figure 5.14: Horizontal Agility plots with binned and normalized data with purple dots representing regions with no viable configurations

From Figure 5.14 it could be seen that the optimal region for these simulations was located on the bottom edge of the viable configuration region for both the L_1 *vs* L_2 and O_1 *vs* O_2 plots. Using these plots equations were developed to describe the relation between L1, L2, O1 and O2 for good configurations. These good regions were then used as the window for the final Monte Carlo simulation.

This final simulation, the results of which can be seen in Figure 5.15, was used to determine the final values of stroke, link length and offset that were optimal. To do this each data point was averaged with its 20 nearest neighbours in each plot. These 3 average values for the initial point were then averaged across all 3 plots. The data point with the highest score after this was selected as the optimal double-link design.

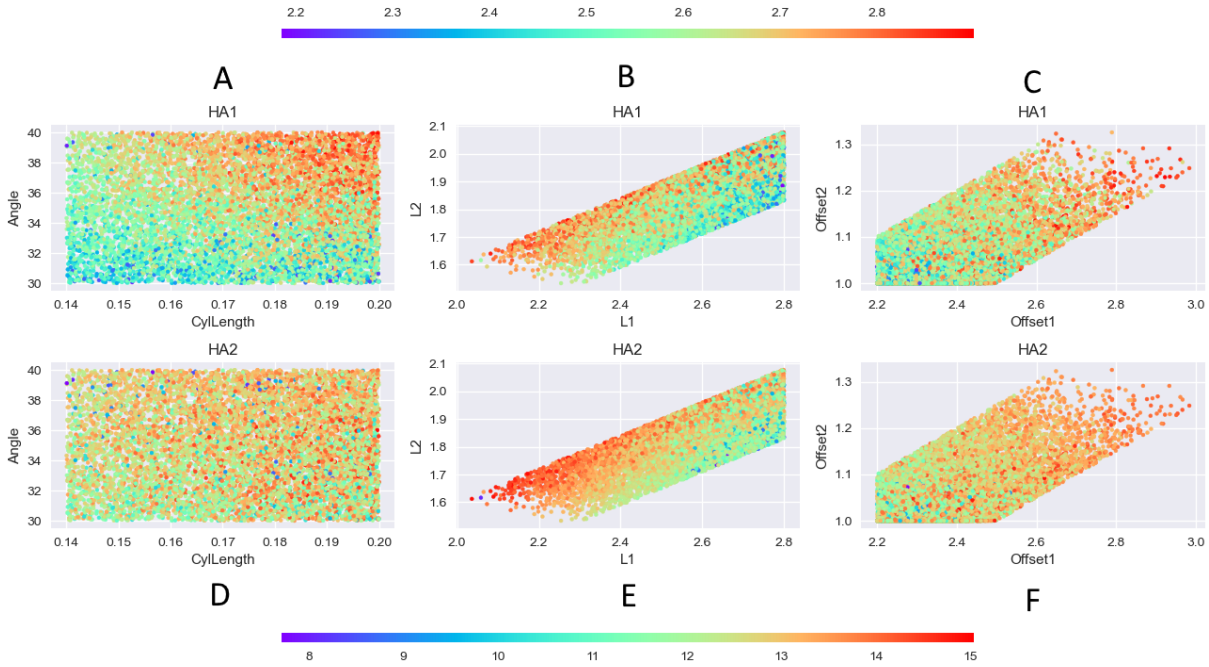

Figure 5.15: Horizontal Agility plots for the final windowed Monte Carlo simulation. Plots A-C are for HA_1 while plots D-F are based on HA_2.

5.4 Cylinder Selection

As mentioned previously it had already been decided to make use of a single-cylinder configuration as this reduced the scope of the control problem and allowed for easier implementation of the system in trajectory optimisation. This was a constraint placed on the project from its inception. The double-link simulation results show that this could have been a viable configuration for the platform and could have offered better performance over its single-cylinder counterpart.

The final selection of the pneumatic cylinder was based on a combination of HA and VA results. A $16mm$ bore was chosen as it had similar performance to the $20mm$ bore in Horizontal agility but was consistently superior in Vertical Agility testing. The stroke length of the cylinder was set at $125mm$ with this length being chosen as it had the greatest hop height in the VA testing while also giving the best HA_2 results for a $16mm$ bore cylinder. The shorter length of this cylinder also alleviated of the risk associated with using the cylinder as a leg as the supported length was shorter.

5.5 Safety Considerations

Due to the high pressures that pneumatic cylinders make use of it was critical to ensure that the cylinder was never loaded in such a way that might cause it to rupture. This was a significant concern are pneumatic cylinder are highly sensitive to transverse loading which can cause jamming or excessive wear on the cylinder in the best case and failure in the worst case. This is an additional concern in this use case as the traditional stress relief method of mounting the cylinder as a hinge was not possible. To this end, a support structure with a breakaway part was constructed. The following sections detail the design of these parts.

5.5.1 Preferential Failure

Preferential failure is a tool used very often in safety-critical applications as it can allow for fail to safe designs. This design, therefore, makes use of this too in the form of a rubber foot link with 3D printed PLA bindings. Due to the intentional fragility of this design, it could not be used to transfer force, instead to accomplish this the metal components of the cylinder rod and the foot were in contact. This contact allowed for the transfer of axial force without subjecting the cylinder rod to transverse loads. Furthermore, if the transverse load got sufficiently high the binding would break and the cylinder wouldn't be loaded further. This concern was not without merit as the motion of the boom would result in such a transverse load. Additionally, this has the benefit of making the system more robust in the case that another component failed causing a crash.

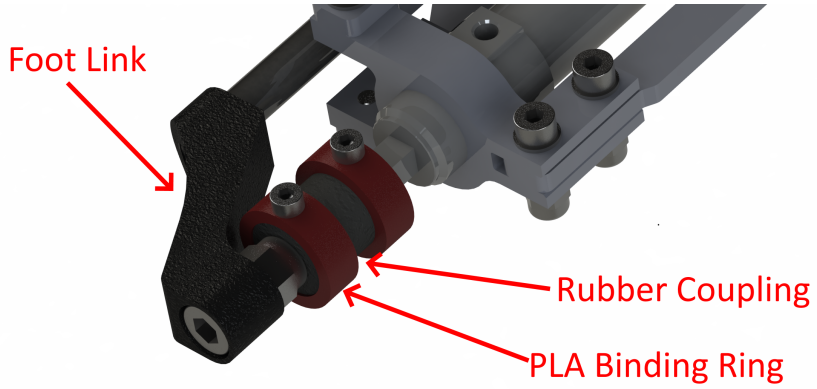

Figure 5.16: Coupling system for the support system.

5.5.2 Piston Support Design

Due to the high bending load on the cylinder, loads significantly higher than the specified design loads from the manufacturer, an additional support structure was required. The specification for the support was that it should be capable of carrying the full stall torque load from the motor ($12Nm$). It needed to be able to take this load from both a strength perspective for failure but also from a deflection perspective to ensure the load wasn't transferred to the cylinder.

This system was designed to make use of precision round rail. This was chosen over profile linear rail for its resilience against jamming under bending loads as the system required smooth operation even in this load case. A further reason for this was the lower cost for round rail and linear ball bearings when compared to similar profile systems. The disadvantage to this is that due to its round cross-section it is not as capable of handling bending loads and therefore requires a larger diameter for the same cross-sectional moment of inertia.

This support rod was run adjacent to the cylinder by mounting the cylinder within a cage of support bars. This cage ensured that the support rod ran parallel to the cylinder and further provided stiffening to the cylinder when under load. The foot link was used to tie the support rod to the cylinder rod, this necessitated it being constructed from steel due to its higher elastic modulus. This higher elastic modulus was required to limit the deflection of this part and making it suitable to support the cylinder rod. This design can be seen in Figure 5.17.

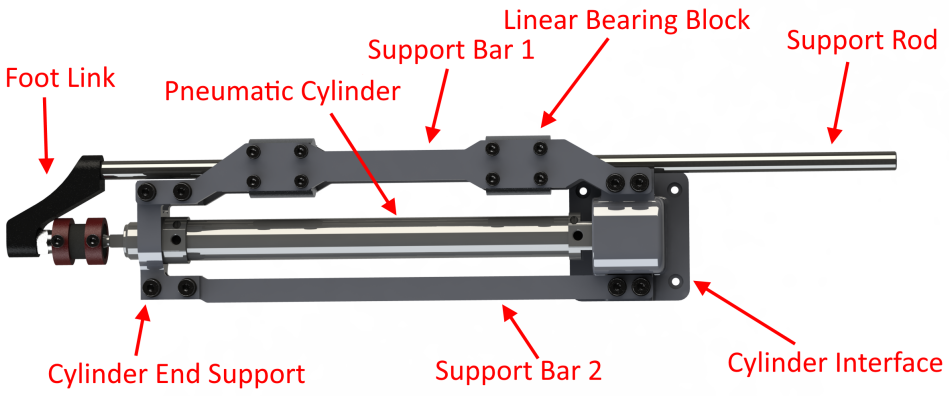

Figure 5.17: Support system for the pneumatic cylinder.

5.6 Final Design

The final design of the different components was motivated by multiple factors often requiring design trade-offs be made. This section serves to show the evolution of the design and the process through which the current configuration was reached. The full final design can be seen in Figure 5.18 below.

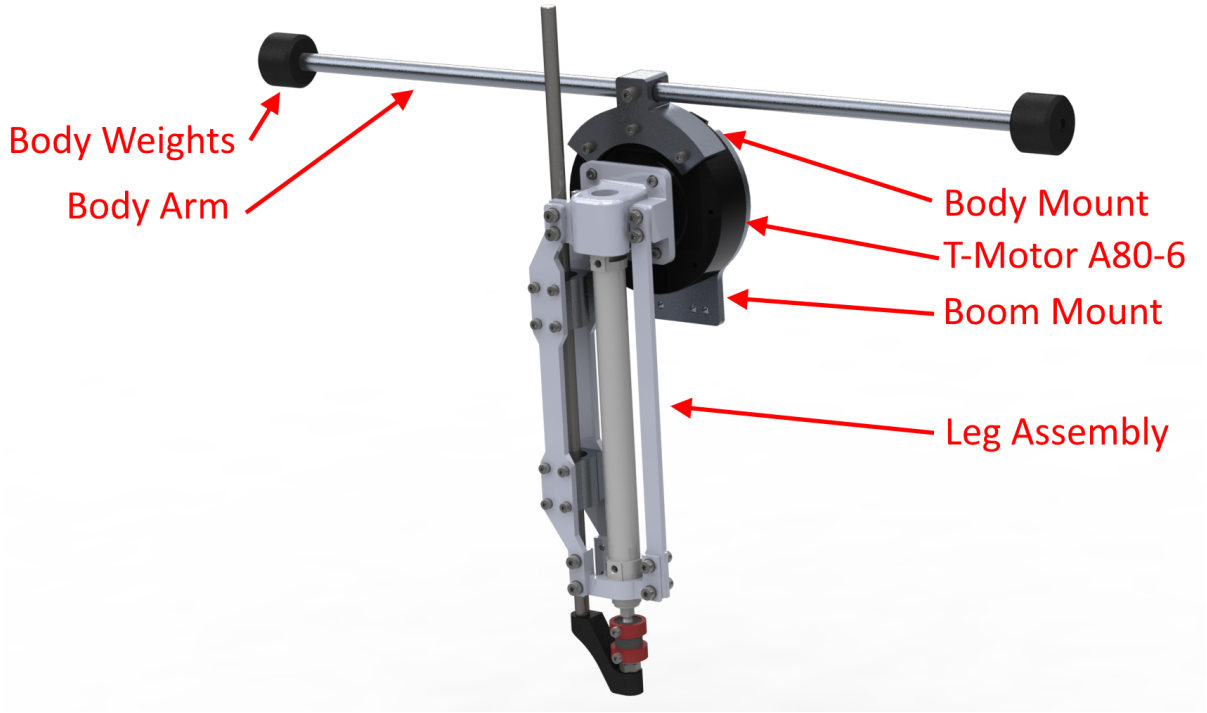

Figure 5.18: Full platform design

5.6.1 Cylinder Motor Interface

One of the most critical parts for the design to function was the interface between the motor and the pneumatic cylinder. This was designed to support the cylinder and act as an interface between it and the motor. An initial design seen on the right of Figure 5.19 made use of a multi-part clamping mechanism. This design was decided against due to its requirement for a five-axis CNC machine to accurately shape the inside of the main interface block.

The built design (seen on the left of Figure 5.19) negated this issue by being made of a single part and using the threads on the top of the cylinder to mate the parts. This

threading was paired with a spring pin to lock the cylinder in place rotationally. Due to thread strength considerations for this part, it was made of 6061 Aluminium. This design only required the use of a three-axis CNC machine for manufacture though created the problem of not knowing the exact supported length due to not knowing where the treads started on each part. This was counteracted by using $1.5mm$ slots at the end of the support bars instead of holes to ensure the system could be assembled.

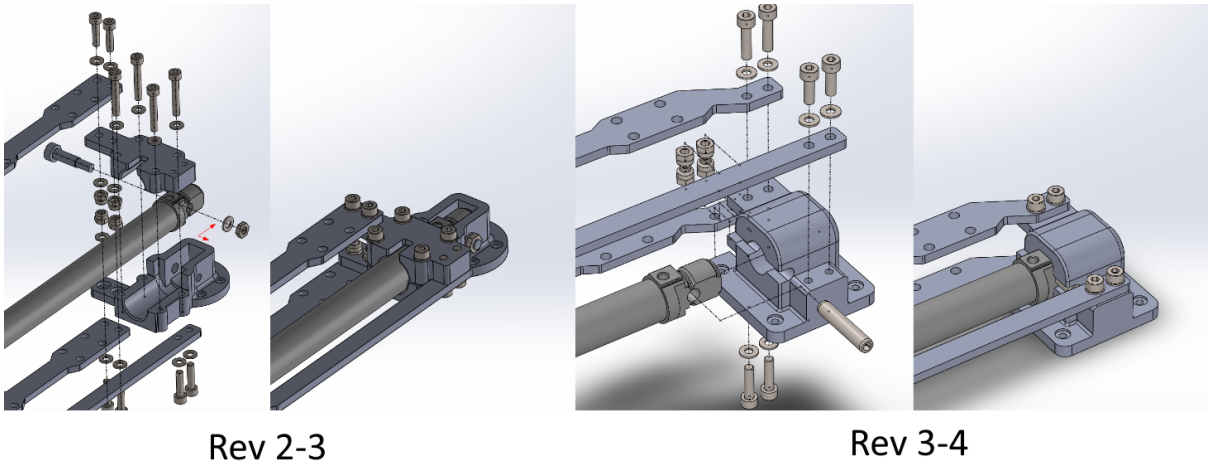

Figure 5.19: Cylinder mount Revision 2-3 exploded and assembled views (Left) and Cylinder mount Revision 3-4 exploded and assembled views (Right).

5.6.2 Foot

The foot design was prioritised for stiffness over everything else as discussed in Section 5.5.2. This design choice was made to make the support more viable but was in direct opposition to the principles of good leg design. This was due to the foot being constructed from steel and therefore significantly increasing the inertia of the leg.

An alternate version was considered that placed the support at the lower point allowing it to be made of a less stiff material. This design was decided against as it made the point of contact off of the axis of the pneumatic cylinder thus complicating control of the system and introducing large loads onto the foot.

5.6.3 Body Design

The main consideration for the body design was its inertia in comparison to the leg's inertia. This moment of inertia of the body was to be maximised for the minimum mass possible. This maximising of inertia was achieved by using a lightweight Al1060 bar with large weights at its ends. The use of these eccentric point masses maximised their effect due to the square relationship between the distance of a mass from a point and its effect on inertia. These point masses were made of mild steel as, though not the highest density material possible, it provided a sufficiently high density at a low cost. The target inertia for the body was set at three times the collapsed legs inertia while the length of the bar was not to exceed double the collapsed legs length.

5.7 Detail Design Summary

Figure 5.20: Final platform as built in its extended cylinder position.

The final platform was successful in minimising the component count for the system. This was predominantly achieved through the use of the motor as the system body, and the fact that the internal bearings in the motor removed the need for rotational support for the leg.

The design of the parts manufacturing was similarly found to be viable as all of the parts were made without error. These parts were also found to be highly robust as none failed during the testing conducted by the author or a PhD student also making use of the platform for testing. This is despite the numerous crashes the robot endured.

The mass and inertia of the leg were sufficiently low to allow for a viable platform, however, both of these were higher than desired. The final leg as-built weighed 1.19 kg with the motor mass accounting for 40.4% of this mass. This mass translated to a leg inertia varied between 0.0116 $kg.m^2$ $-$ 0.0227 $kg.m^2$ depending on the current length of the cylinder. The increased weight was due to the support system and its need for steel components to reduce deflection.

The high inertia of the leg also increased the body mass to provide enough inertia to allow for a controllable system. The fully assembled monopod with the body weighed 1.53 kg with the leg mass accounting for 46% of the mass of the monopod which is higher than other platforms such as Baleka (13.2% [39]) or the MIT Cheetah ($\approx$ 10% [25]). However, due to one of the actuators being included in the leg this still results in a lighter overall platform.

The platform was easy to assemble, due in part to the low component count. An additional contributor to this was the fact that almost all fasteners were accessible at any time with only one bolt obscured by the support bars.

Recommendations for changes to the platform design can be found in Section 9.

Chapter 6: Boom Mechanical Design

This chapter details the process through which the mechanical design of the boom was conducted and the choices involved in developing it. The chapter begins with the development of the specifications followed by the mechanical design, taking into account all considerations before moving on to system validation and acceptance testing.

6.1 Requirements and Specifications

Due to the monopod nature of the robot, a testing support structure was needed to be constructed. This structure needed to support the platform in the sagittal plane as this allowed for a reduction in the control complexity of the platform. To select a boom design the booms described in Section 2.5.1 The following were established as implementation neutral requirements for this structure as the support needed to:

- allow for long time horizon testing (multiple continuous hops with both acceleration and deceleration phases)
- have a minimal effect on the robot's dynamics
- have a consistent effect on the robot's dynamics
- allow for sensing of world frame variables (height, forward velocity, etc.)
- allow for the testing of other platforms, including different robot morphologies - such as planar quadrupeds.

The first requirement negated the possibility of using a trolley, rails system or friction slider since these are all either limited in the distance the platform can travel or require a treadmill (which is unsuitable for transient manoeuvre's). This, therefore, forced the use of a boom.

Once the selection of a boom was established a second set of requirements were created with special consideration for this implementation. These requirements were as follows, the boom should:

- deflect less than 5° under the acceleration of the platform
- weigh less than 2.5 kg as a reaction at the tip
- be sufficiently long that the small-angle assumption holds vertically
- have 3 degrees of freedom that are individually lockable
- sense position and velocity for all 3 degrees of freedom

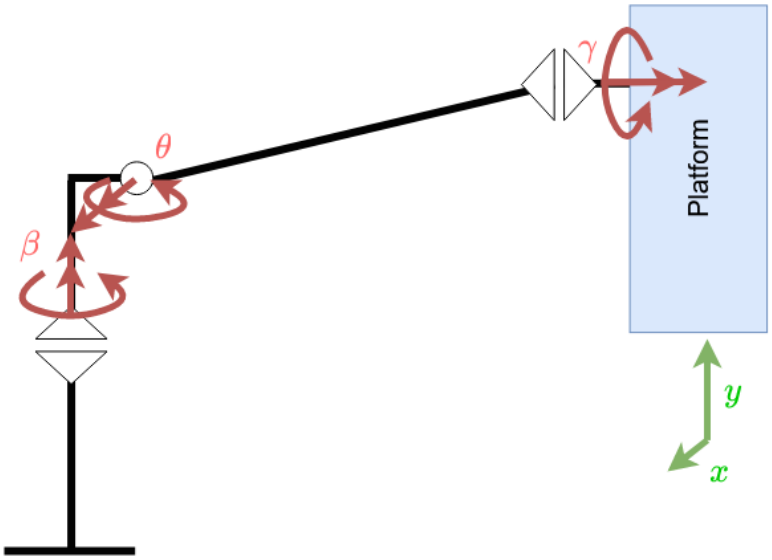

Figure 6.1: Boom co-ordinate reference frames.

The maximum hop height, found in Section 5.3.1.1, of 0.4 m was used to find the minimum length of the boom based on the small-angle assumption for hop height. A trigonometric sin error of less than 1% was desired, therefore, a change in angle for the boom of less than 14° was required. To achieve, this a boom needed an arm longer than 1.65 m.

The boom was designed to carry a planar quadruped of similar size to the monopod. The size of the body for such a quadruped was estimated to be 1.6 times the leg length, with this scaling factor being based on the proportions of a cheetah [93]. For these proportions, a quadruped of similar size would have a body length of 0.61 m.

This body length paired with the assumption that the leg would make contact at a maximum of 50° ahead of the horizontal created a maximum distance from the contact point to a central mounting point of 0.55 m. For this to be within the 14° constraint a minimum boom length of 2.27 m was required.

Due to supply constraints, a boom bar length of 2 m was selected this resulted in a boom with an overall length of 2.145 m. A parallel bar design was selected for the boom. This choice was made to reduce the rotation of the platform but also had the added benefit of reducing the transverse load on the system that would occur due to the leg of the platform not being vertical.

6.2 Rigidity Considerations

The most significant consideration for this design was the rigidity of the boom arm. This was a concern due to the length of the boom and the weight considerations for the boom's design. These weight considerations meant that commonly used high Young's Modulus materials such as steel were not considered viable. Furthermore, due to the size requirements for the beam, custom fabricated composite materials were also not a viable option.

This resulted in the design of a cable-stayed aluminium boom. The design was based on the designs of radio antennas [94] and ships masts [95]. These designs all make use of tensioned cables to reduce the lateral motion of fixed points on the boom.

This design is not without risk, as high compressive loads can cause buckling failure. The risk of this mode of failure is compounded by the length of the boom and low Young's Modulus of the Aluminum used in its construction. The equation for buckling load failure can be seen in Equation 6.1 below [96].

$$F = \frac{n\pi^2 EI}{L^2} \tag{6.1}$$

In this equation F represents the allowable load, E the Young's Modulus, while I the moment of inertia. The variable n is a correction factor for the mountings of the system.

As the ends of the beam are treated as hinge joints rather than fully built in, this constant is 1.

For this analysis, the system was simplified to assume that buckling would occur in region of B_1 and B_2 as seen in Figure 6.2 below as this was the highest loaded section and the longest span between cable points. This gave a permissible compressive load of 3730 N. Due to uncertainty in the applied loads on the boom, the permissible axial load due to cable tension was set to be $2400N$.

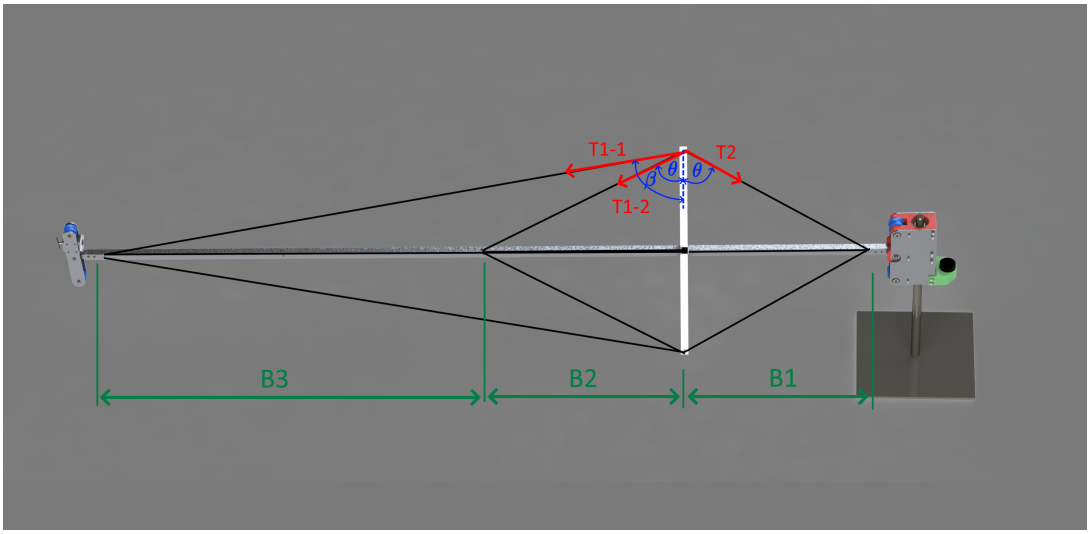

Figure 6.2: Force diagram for the cable assembly of the boom in the plane of 1 set of cables. A second set of cables also present normal to this. This full configuration can be seen in Figure 6.7

It was decided to make the transverse force due to each cable equal except for T_2 which acted to prevent bending of the strut arms and was therefore equal to the sum of all the other compressive loads. This lead to a maximum axial cable load of 627 N for T_{1-1}, 572 N for T_{1-2}, and 1200 N for T_2.

6.3 Design, Assembly and Maintenance

The design of the boom was to be as simple and as low cost as possible. This was achieved by minimising the number of custom manufactured components and was successfully achieved, limiting the manufactured components to four shafts and one bearing housing. The remaining parts were either standard components that could be purchased, 3D printed or laser cut.

The design was lightened by removing one of the boom arms in the four-bar linkage. This was compensated for by attaching tension cables above and below the rigid boom arm. As one of the two cables was always in tension the altered design still operated in fundamentally the same way while allowing for a significantly lighter boom.

To sense the position and velocity of the system in the x, y and γ directions, encoders were located at each of the joints (symbols as per those seen in Figure 6.1). The encoder at the β joint was geared through the use of a timing belt and was used to calculate the approximated x position and velocity. The encoder at the θ joint was attached similarly and was intended to approximate the y position. This configuration can be seen in Figure 6.3 below.

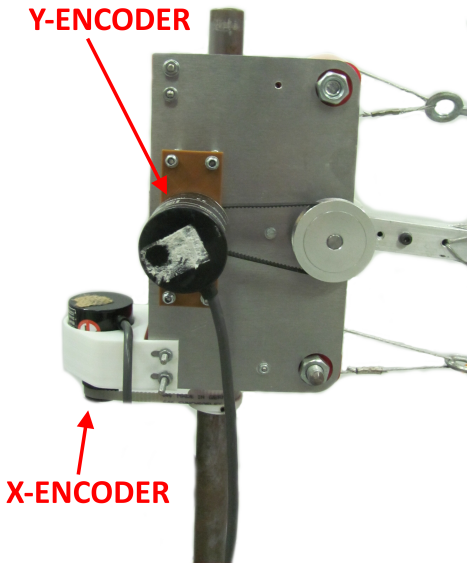

Figure 6.3: Encoders used to measure the movement of the boom (the Y-encoder was removed in later versions).

To tension the cables correctly, their vibrational frequency was used as a proxy measurement for tension. This was possible through the use of the expression of the standing wave equation seen below [97]:

$$f_1 = \frac{1}{2L}\sqrt{\frac{T}{\mu}} \tag{6.2}$$

In the above equation, L is the length of the cable, T is the tension and μ is the mass of the string per unit length. It was found experimentally that the steel cable used had a linear density of $\mu = 9.63\frac{gm}{m}$. The frequency of the cable was measured using a cellphone audio frequency analyser [98]. This method was validated by comparing the force measured by an optoforce force sensor to the measured frequency of the cable while on a test rig.

6.4 Design Validation

Validation of the system was done in two parts. The first was through simulation in Solidworks while the second was through the testing of the physical system.

6.4.1 Simulation Validation

The simulation based validation of the system was done using Solidworks simulation package using its buckling load analysis feature. This was done due to the buckling failure concerns due to the axial load due to the cable tension. This simulation constrained the base of the boom as a pinned joint and using the chosen cable tensions as point loads, pointing in the direction of the cables (shown in Figure 6.4). The deformed shape form this simulation can be seen below:

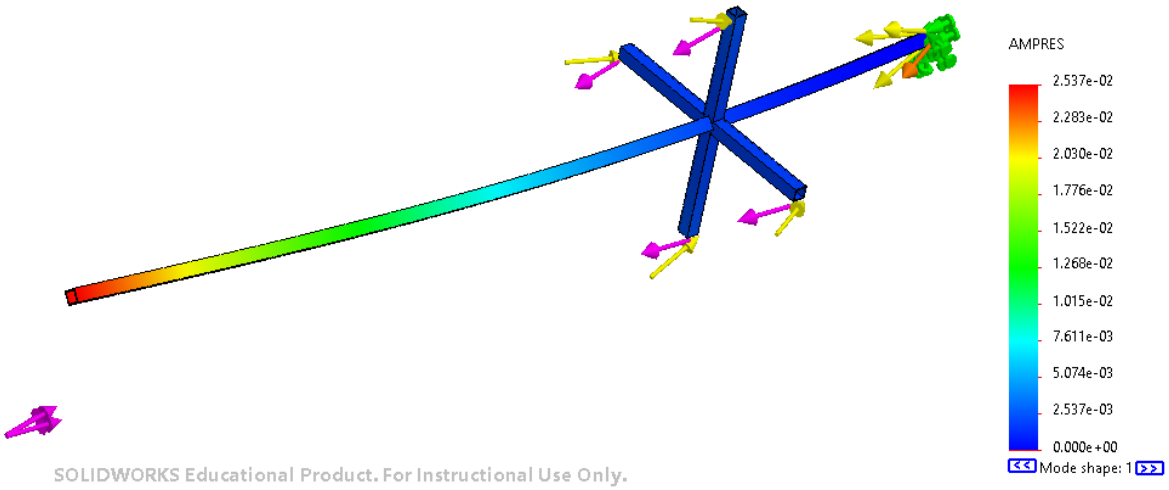

Figure 6.4: Buckling analysis conducted in Solidworks showing the maximum displacement of the boom under its first mode

The shape of the first buckling mode shown in Figure 6.4 is not realistic, as this could not be achieved in reality due to the constraint of the cable stiffness. A further attempt to model this using the SolidWorks elastic spring and tensile preload options did not yield sensible results.

Due to the complexities of building an accurate buckling simulation and validating the results thereof, and the low risks associated with a buckling failure of the boom, it was decided to go ahead with boom assembly. The boom's cables were incrementally pretensioned, while monitoring the structure for any deflection. At the design pretensions, the boom was stable. Manual movement of the boom did not reveal any worrying deflections or instability that might impede the planned testing.

6.4.2 System Acceptance Testing

The physical acceptance testing of the system was conducted by running vertical hopping tests similar to those seen in Section 4.3 but with the platform mounted to the boom rather than linear rails. This was done twice, first without the cables attached and then with them on and correctly tensioned. As the height of the system was measured through an encoder at the θ position if the boom arm was not sufficiently rigid it would be visible as low-frequency noise in the data. The results of these tests can be seen in Figure 6.5

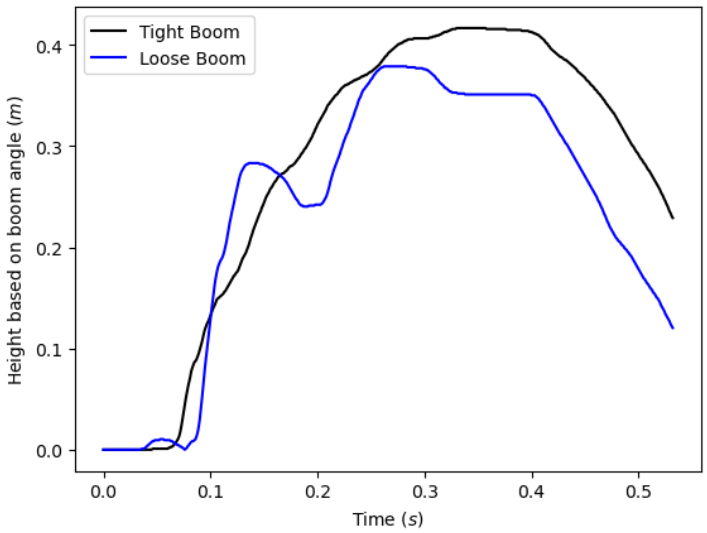

Figure 6.5: Position time graph for the boom with tight and loose cables using the θ encoder to measure the y position.

This testing showed a marked improvement in the boom rigidity due to the cables and can be seen through the smoother, more parabolic trajectory for the tensioned boom. This is not to say that the tensioned boom was entirely effective as a low-frequency wave superimposed on the trajectory was visible, thus showing that non-negligible deflection still occurred.

This deflection can be seen in greater detail in Figure 6.6 below. This figure shows that the encoder measurement under-represents the position of the platform compared to LiDAR readings. Furthermore, there is a notable delay in the encoder readings based on when the motion is observed to start. This lag was caused by the large inertia of the boom resisting its motion and causing a deflection.

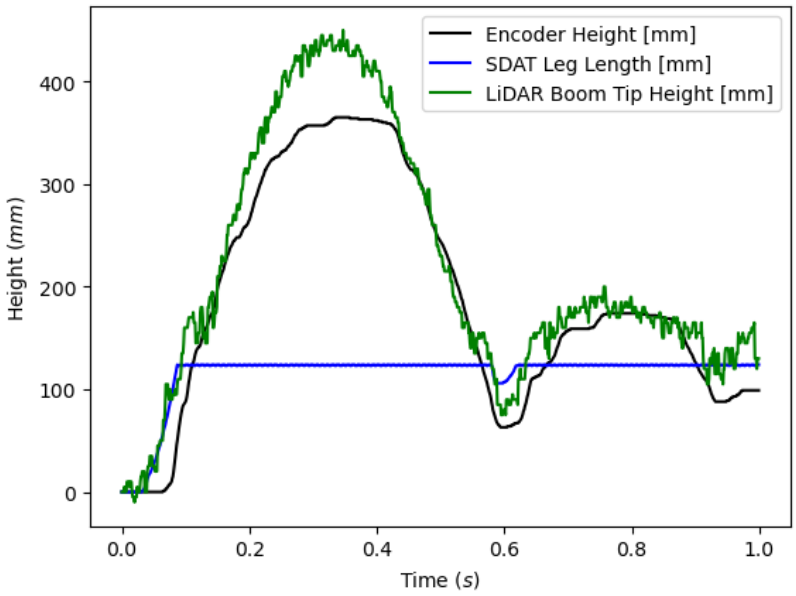

Figure 6.6: Position time graph for the boom with tight cables using the θ encoder, a Garmin LiDAR Lite V3 and SDAT linear encoder to measure position.

6.5 Summary

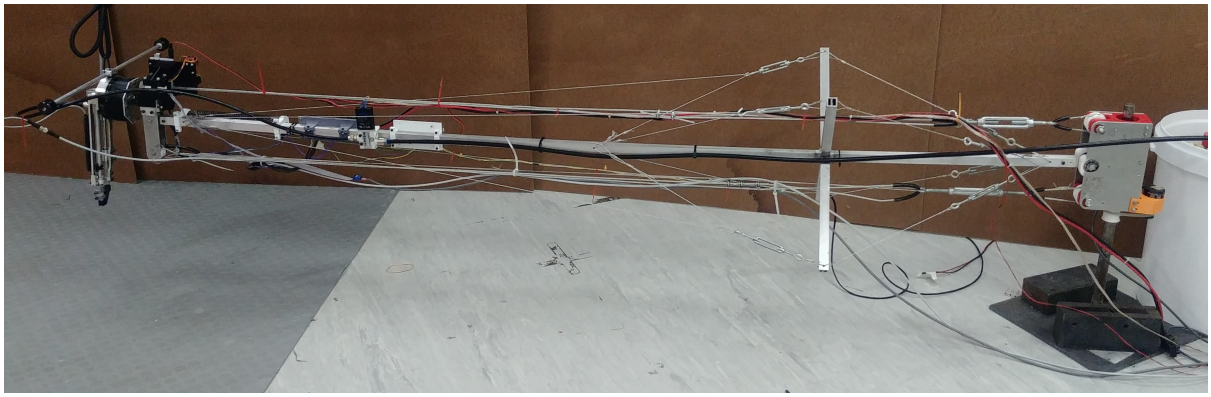

Figure 6.7: Boom as built and fully assembled with the platform attached. The full sensor and controller system is attached to the boom.

The boom did not perform as well as was hoped, making the use of an encoder to measure the vertical position of the platform impractical. Despite this, it was still possible to use the encoder at the β joint to approximate x position as this axis had significantly lower acceleration and was not affected by gravity.

Although the boom did not perform as well as hoped it was still very successful in reducing the weight of the support system and increasing its rigidity when compared to more traditional boom designs of comparable size. The weight reduction came primarily from the use of top and bottom cables to approximate a four-bar linkage without requiring the use of a full additional bar. These design changes made this boom significantly stiffer and lighter than comparably sized booms.

Chapter 7: Estimation and Control

7.1 System Architecture

For architectural purposes, the system was considered as three distinct parts: the boom, the robot and the master system. This was done to allow for the boom to be platform-independent with only changes to the robot controller running on the master system. The system architecture can be seen in Figure 7.1 below:

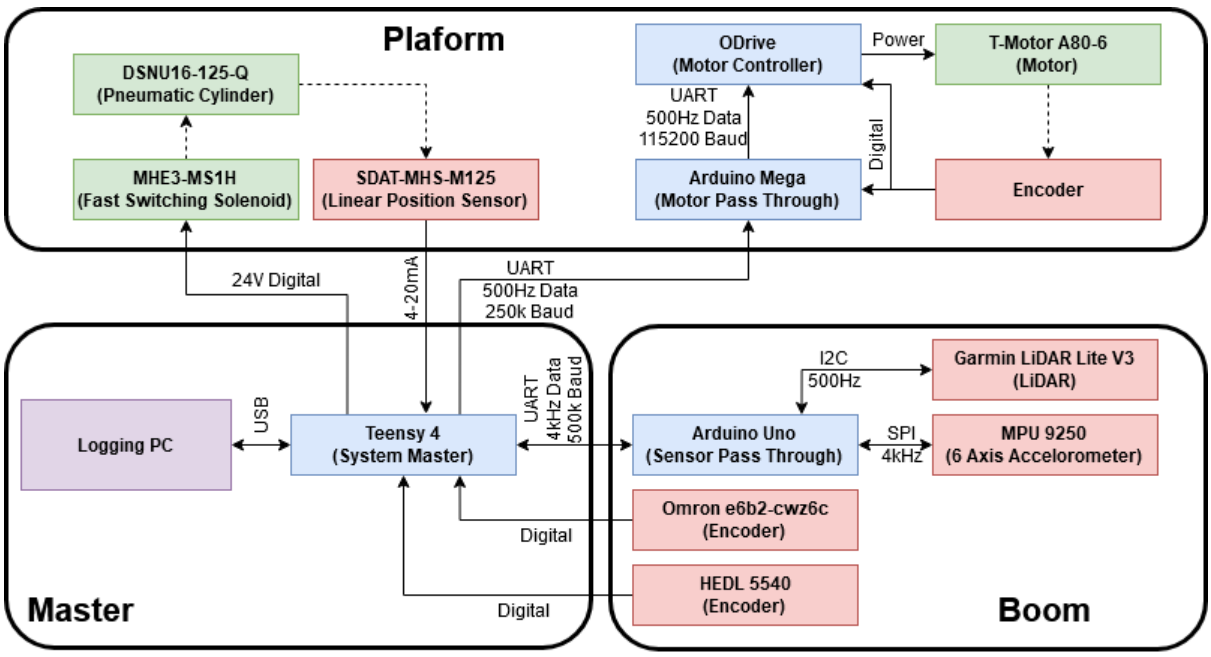

Figure 7.1: System architecture, controllers are represented in blue, sensors in red and actuators in green. Electrical connections are represented with solid lines while physical connections are shown with dotted lines. Above each electrical line, its communication interface is specified.

For the system master, the *Teensy 4* was selected due to its high clock speeds (600MHz) and library availability to aid in programming. The system master took in all sensor information which was fused using a Kalman Filter to estimate the system states, that were then used to control the system. The system master also had logging capabilities, utilizing Matlab's serial Library, logging all the Kalman Filter state variables and sensor

data at a Baud Rate of 500k Baud. The sensor selections and how they interface with the system is described in the sections that follow.

7.2 Boom Sensors

The objective for the boom was to be able to sense the motion of the platform in each of its allowed degrees of freedom. The degrees of freedom of interest were: x, y and roll (γ) (notation as per Figure 6.1). Due to the high vibrations and impact loading present in the system the sensor data received was noisy and not always accurate. These errors necessitated the use of multiple sensors which were fused through the use of a Kalman Filter. This filter was required primarily to get a higher resolution for the vertical position and velocity states of the platform. These states needed a high resolution due to the short duration's of the hops and their use in the various controllers.

7.2.1 Sensor Selection

There were several sensors available for selection, which had numerous advantages and disadvantages, described below. Many of these sensors were available for use as they already existed in the lab, these sensors that were already in stock were prioritised due to time and supply constraints that were exacerbated by the COVID-19 pandemic.

7.2.1.1 Position Sensors

For the effective control and monitoring of the platform's position and orientation in space was required. These position sensors were needed to monitor the x, y and γ positions of the platform as described in Figure 6.1 previously. The sensors themselves can be seen in Figure 7.2 while their properties can be seen in Table 7.1.

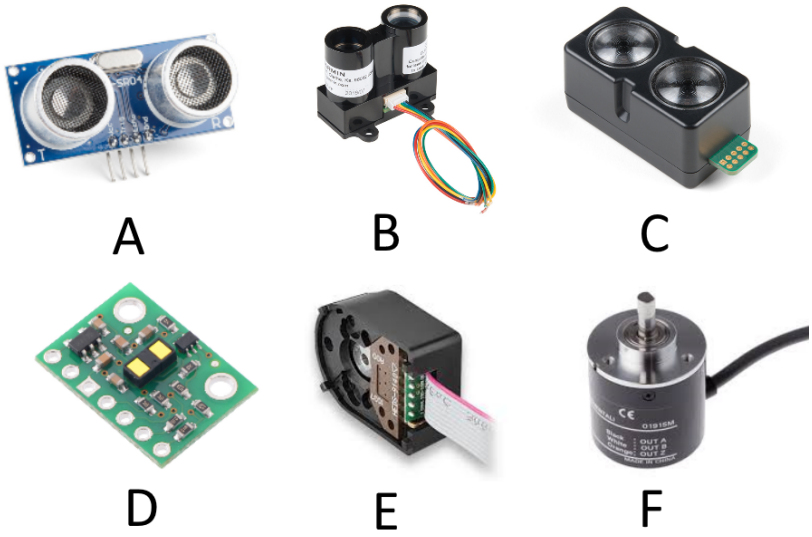

Figure 7.2: Various position sensors considered for the system. A) HC-SR04 Ultrasonic sensor; B) Garmin LiDAR Lite V3; C) Garmin LiDAR Lite V4; D) VL530x Time of Flight Sensor; E) HELD-5640 Optical Encoder; F) Omron E6B2 Optical Encoder.

Table 7.1: Table comparing the properties of different position sensors.

	Resolution	Accuracy	Cost	Update Rate	Range	Degree of Freedom
HC-SR04 Ultrasonic	3mm	3mm	R29	50Hz	2-400cm	y
Garmin LiDAR Lite V3	1cm	2.5cm	R2798	500Hz	0.15-40m	y
Garmin LiDAR Lite V4	1cm	1cm	R1695	200Hz	0.05-10m	y
VL530x Time of Flight	1mm	7%	R195	30Hz	2-200cm	y
HEDL-5640 Encoder	500 PPR	0.0126rad	R1577	Digital	-	β, θ, γ
Omron E6B2 Encoder	1024 PPR	0.0061rad	R3729	Digital	-	β, θ, γ

For the selection of a position sensor, the update rate was a critically important factor as full hop had a duration of $\approx 0.4s$ as seen in the previous hop up test in Section 4.3.1. This short hop duration meant that the lower update rates of the *HC-SR04* and *VL530x* made them too slow to be usable for real-time control of the platform. The encoders were the antitheses to this with update rates limited by the interrupt speeds of the microcontroller

monitoring them or the speed of their motion. Furthermore, these sensors do not have inaccuracies but are rather limited by their resolutions. For these reasons (and the fact that there was stock of this part in the lab therefore negating their higher cost) it was initially intended to use *Omron E62B* encoders to monitor the x and y positions of the platform. This worked for monitoring in the x direction but failed in the y direction due to boom flex as discussed in Section 6.4.2. The *Omron* encoder was mounted to the β joint through the use of a timing belt to increase its positional sensitivity by a gear ratio of 2.62. This can be seen previously in Figure 6.3.

The y axis sensor was by process of elimination limited to a choice between the *Garmin LiDAR Lite V3* and *V4*. These parts had some similarities with both being small LiDAR units that communicate over an I2C interface. However, from these two parts, the *LiDAR Lite V3* was chosen due to its higher speed. An additional benefit to selecting this part was that stock of it was already in the lab and therefore did not need to be purchased. The disadvantage to this sensor choice however was its relatively low accuracy and the short range of communications due to its use of the I2C protocol.

The final position sensor required was an encoder at the tip of the boom for the γ joint. This required an encoder as it was the angle of the platform at this point that was of interest. For this encoder the *HEDL-5640* encoder was chosen. This part was chosen over the higher resolution *Omron* due to its significantly smaller size allowing for a greater range of motion of the boom without collision between the boom and encoder occurring. This interference issue is shown in Figure 7.3 where the smaller *HEDL* encoder avoids interference.

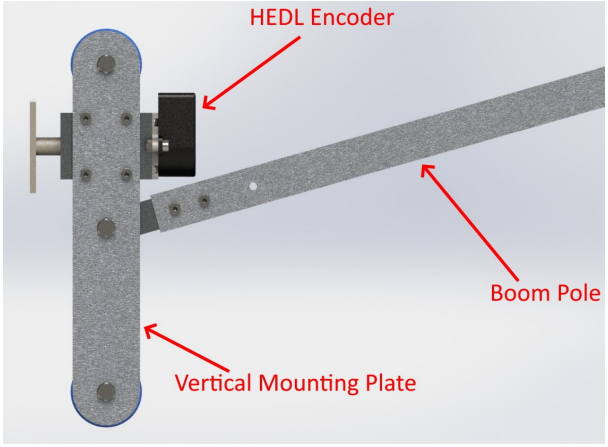

Figure 7.3: Mounting of the *HEDL* encoder on the boom from SolidWorks.

7.2.1.2 Accelerometer

The accelerometer used was the *MPU9250* (depicted in Figure 7.4 below). This part was used as it was in stock with the lab and therefore was able to be acquired immediately for testing. Due to its successful use in its initial testing, it was implemented into the final system.

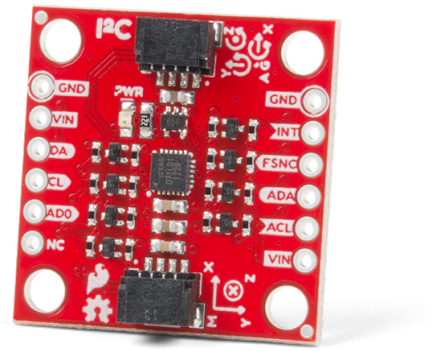

Figure 7.4: MPU-9250 Sparkfun Breakout Board.

This chip is a 9-Degree of freedom sensor with a 3 axis accelerometer, 3 axis gyroscope and 3 axis magnetometer. The magnetometer was considered unreliable due to its proximity to the motor while the gyroscope measurement was only variable in one axis, where it was superseded by the encoder as that was a more accurate senor. For this reason only accelerometer reading were considered. The accelerometer had a maximum full-scale range of $\pm 16\ g$ and resolution of $0.488\ mg$ due to its onboard 16-bit ADC. The largest scale range of $\pm 16\ g$ was used due to the high shock loads present in the system and this allowed for less clipping to occur. The accuracy of this sensor was quantified by setting it stationary on a table and logging its output for 15 minutes. This gave errors of $\sigma_{MPU_Z} = 3.65e-5$ and $\sigma_{MPU_x} = 1.81e-5$ for the two axes of interest.

This chip was advantageous due to its high speed of $4k\ Hz$, this speed being owed to the use of an SPI interface. The combination of the use of SPI (a short range communications protocol) and the need to mount the sensor at the tip of the boom necessitated a conversion in communications protocols.

7.2.2 Subsystem Architecture

The use of the *LiDAR Lite V3* and the *MPU9250* necessitated the use of an additional microcontroller to repackage the data from the sensors and transmit it to the master system using a long range communications protocol. This was required as these sensors needed to be mounted at the tip of the boom while the system master needed to be set at the base of the boom due to its interfaces with other components such as the logging PC, safety switches, and other user interfaces. For this repackaging, an *Arduino Uno* was used due to ease of programming, low cost and existing libraries for both sensors.

In this subsystem, LiDAR data came into the microcontroller over I2C at $500Hz$ while accelerometer data for the x and y axes was received over SPI with a clock speed of $1MHz$ and a data rate of $2kHz$. This data was then repackaged into a data-frame with an identifier for the property being measured, the data itself, a parity bit and a stop bit. This data was then sent to the system master using 5V UART with a baud rate of 500000 at a data rate of $2kHz$. This boom tip sensor assembly can be seen in Figure 7.5 below.

The boom encoders were run directly to the system master. This was done to reduce the load on the *Arduino Uno* and prevent overloading its serial capabilities. The communication distance was also not a concern as these were differential digital outputs sent along a shielded cable.

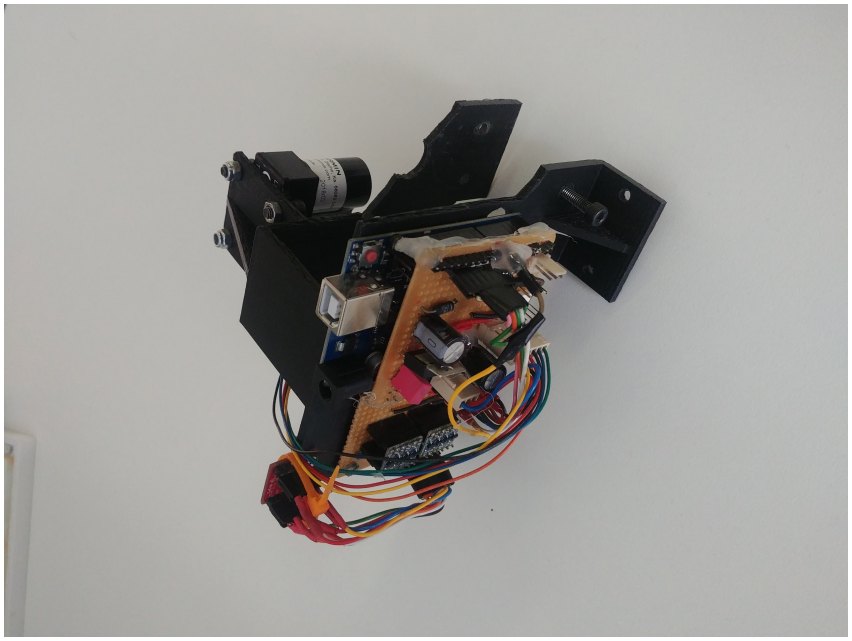

Figure 7.5: Assembled boom tip sensor brick.

7.3 Kalman Filter

Due to the resolution and accuracy limitations of the LiDAR used it was decided that a Kalman Filter would be implemented to improve the quality of the positional data for the system. As this was primarily an issue with the LiDAR, the Kalman Filter was only applied to the y axis. The lower jerk in the x axis allowed for the use of an encoder in this direction which was significantly more accurate. The general form equations and full system equations used can be seen in Appendix C.

The system variables of interest were:

$$X = \begin{bmatrix} y & \dot{y} & \ddot{y} \end{bmatrix}^T \tag{7.1}$$

Where X was the system state matrix, while y was the the vertical position of the platform (tip of the boom) and its derivatives.

There were two expressions of the Kalman Filter tested in simulation before implementing a final version on the platform. This distinction was based on how the accelerometer data was fused into the system. The first option treated it as a control input to the system while the second option implemented it as a sensor in the update stage of the filter.

For the simulated testing of each of the Kalman Filter expressions Matlab's Simscape Multibody and Simulink were used to model the physical system (including the boom modelled as a mass attached to the platform by a spring due to it deflection), sensors and run the Kalman Filter. This allowed for comparisons to truth data and rapid tuning of the covariance for the system.

The accelerometer was hardware limited to a full-scale reading of $\pm 16g$ which resulted in each ground contact overloading the sensor and clipping the measurements. This combined with the normally small error in the accelerometer reading caused instability in the Kalman Filter. To counteract this effect the covariance for the accelerometer input was greatly increased for accelerometer readings above $14g$. This action acted to bias the filter state towards the LiDAR readings for these contact periods. This increase in covariance was tuned using the aforementioned Matlab model. The access to truth data

from the model with the simulated Gaussian error of the sensors allowed for this empirical tuning.

The results of the filter using the accelerometer as a control input can be seen in Figure 7.6 below. The output of the filter when using the accelerometer as a sensor input was similar to what is seen in Figure 7.6 though with slightly worse error characteristics. This small degradation in performance can be seen in the difference in the errors of the two configurations seen in Figures 7.7 and 7.8. The spikes in error due to the large contact accelerations can be observed in Figure 7.7 where the error spikes coincide in time with the change in direction of motion of the body (from down to up) and cylinder rod (changing from stationary to moving up) both of which seen in Figure 7.6.

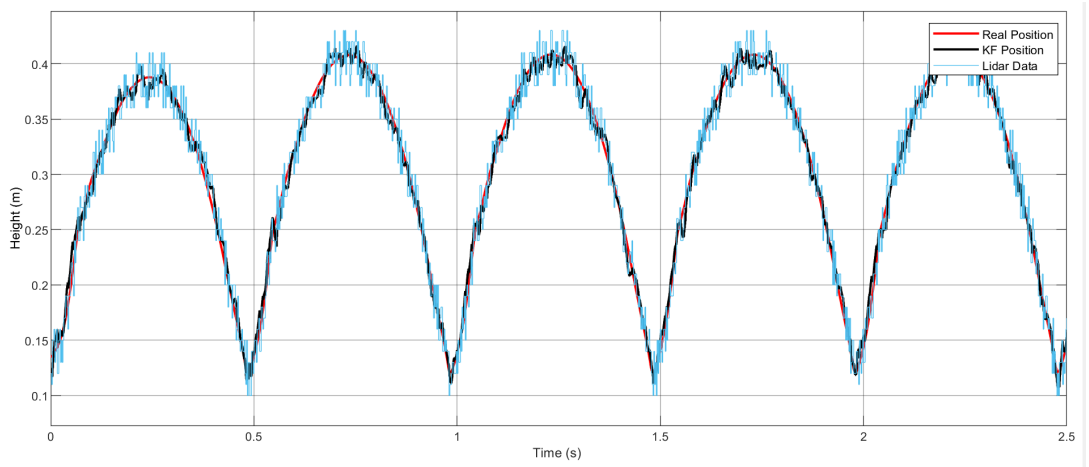

Figure 7.6: Position time graph for the system hopping vertically. This plot includes the truth data position, KF output and LiDAR input.

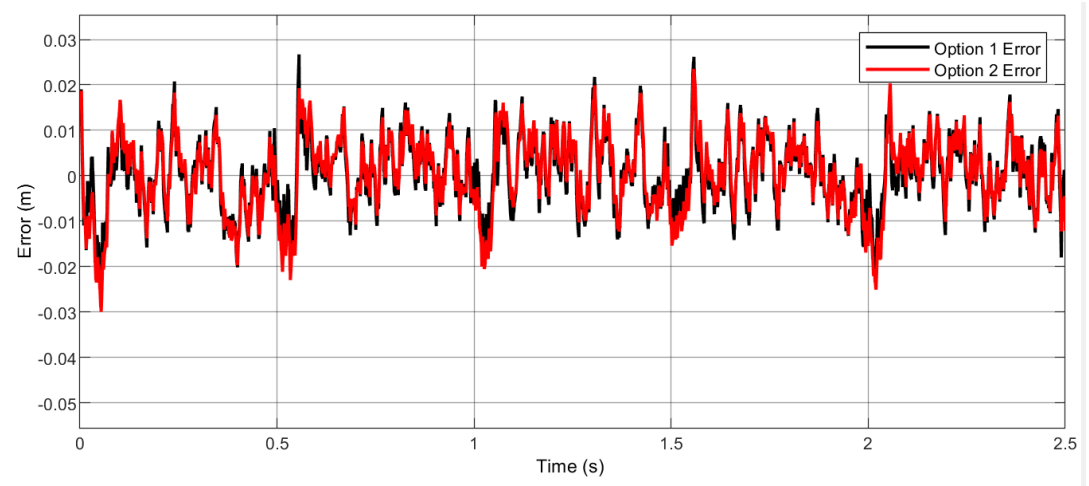

Figure 7.7: Errors of the two different Kalman Filter configurations vs time.

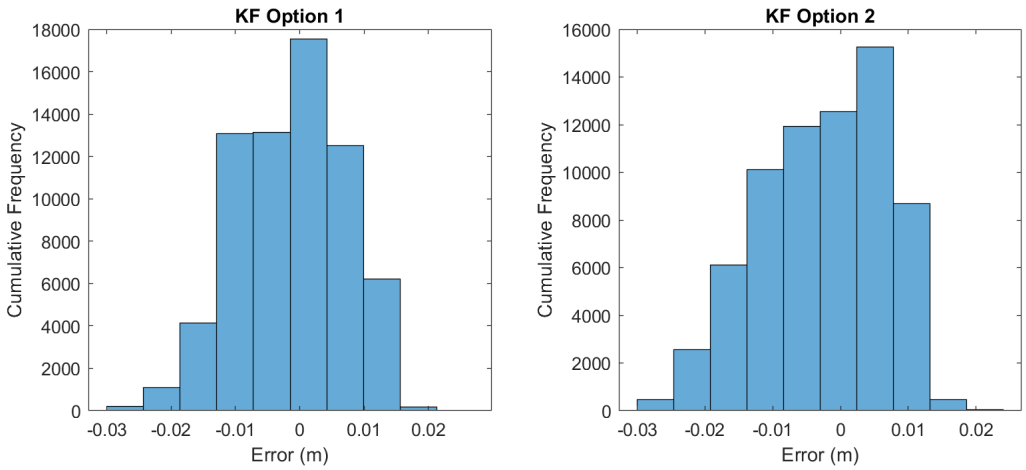

Figure 7.8: Cumulative frequency histogram for the errors for the different Kalman Filter expressions.

Evaluating the errors of the different expressions it was found that option 1 (using the accelerometer as a control input) had a mean of $\bar{x_1} = -1.3\ mm$ and a standard deviation of $\sigma_1 = 8.2\ mm$. Option 2 had similar, if slightly worse, performance with a mean of $\bar{x_2} = -2.6\ mm$ and standard deviation of $\sigma_2 = 9.1\ mm$. In both of these cases, the performance of the Kalman Filter was significantly better than the LiDAR alone. Due to its slightly better performance option 1 was implemented in the real-time system. This was useful as it offered a sensor variance reduction of 63.6% over the use of the LiDAR alone.

This real time implementation was achieved through the use of of a Linear Algebra Library. The initial, known state, of the system was a high found by averaging 100 LiDAR readings with no velocity and the only acceleration being due to gravity. The filter itself was then run at the control loop frequency of $2kHz$.

7.4 Monopod

The sensors for the monopod were used to establish the state of the actuators in the system. These states included the length and angle of the leg. In addition to these sensors, this subsystem required drivers to power the actuators. The sections that follow detail the selection of these sensors and their properties, it also considers the selection of drivers. Finally, it discusses their implementation into a cohesive subsystem

7.4.1 Monopod Sensors

The position of the pneumatic cylinder was measured through the use of a *Festo SDAT-MHS-M125* position sensor (depicted in Figure 7.9). This non-contact sensor measured the position of the piston within the cylinder using hall effect sensors and transmitted it as a $4 - 20\ mA$ signal. This sensor gave a very accurate position of the cylinder with a resolution of 0.05 mm and an accuracy of 0.1 mm. This high positional accuracy was also paired a high sampling speed as the typical sampling interval for the position was 1 ms. The final advantage of this sensor was that it did not require any additional infrastructure to sense the position of the cylinder. For all of the above reasons, this was considered to be the most reliable linear position measurement in the system and was used to validate that the Kalman Filter was implemented correctly and was accurate to the real system. This was done by comparing the takeoff and landing points (the points where the system moved into or off of its full length respectively) in the vertical case to determine if the Kalman Filter's output was aligned to these points. If so it was considered to be accurate.

Figure 7.9: SDAT linear position sensor for pneumatic cylinders.

The second senor used was a motor encoder. The encoder used was the *RMB20IC* and was a hall effect encoder rather than the optical encoder similar to those used previously. This encoder was not specifically selected but rather was a part of the selected motor and was built into it. This encoder had a resolution of 4096 counts per revolution transmitted as a differential 5V signal.

7.4.2 Monopod Actuator Drivers

There were two actuators in the system with each requiring their own driver. The simplest case was the switching circuitry for the solenoid valve. The solenoid required either 0 V or 24 V and consumed up to 4.5 A in a current spike as the solenoid was activated. These power requirements were achieved thought the using a Darlington transistor *(TIP122)* in digital mode. This allowed the solenoid to be driven from a single microcontroller pin and 24 V power supply output.

The motor required a more complex driver with the *ODrive V3.6* (56-volt version) being used. This motor controller, shown in Figure 7.10, was selected as it allowed for UART communications from a microcontroller to give it commands in addition to its USB interface and was recommended by T-Motor for use with their A80-6 motor. Many other servo motor controllers for BLDC motors are designed for use with larger motors used in automation and not the smaller motors seen in robotic platforms. For this reason, many of these servo control motor controllers are ineffective or unusable with these smaller motors due to the lower inductances of these motors. Furthermore, many of these controllers make use of communications protocols that are difficult to implement on a microcontroller (such as EtherCAT) as they are designed for use with larger PLC-based systems.

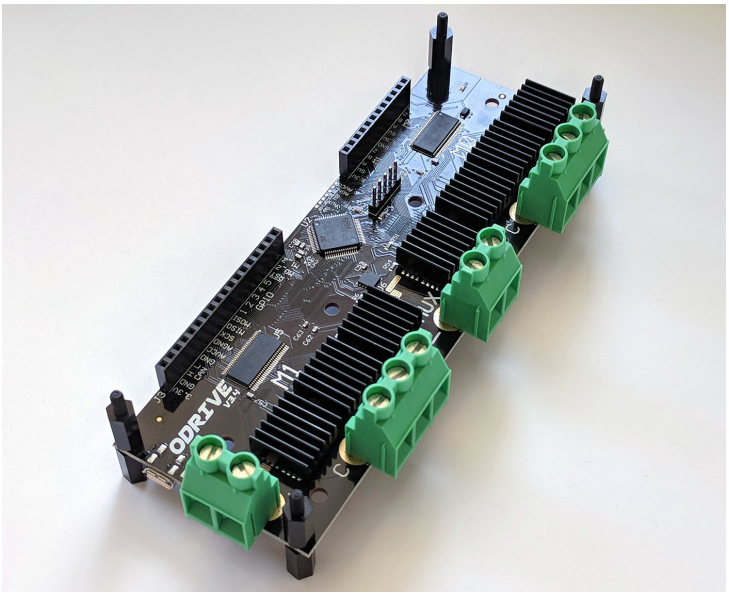

Figure 7.10: ODrive motor controller.

In conjunction with the motor controller, a shunt resistor of 5Ω and $150W$ was used. This resistor was needed so as to not overload the power supply when the motor was being back-driven. The size of this shunt resistor was based on the maximum current of the motor and the power resistors on hand. This could be removed in future by running the motor off of a battery where this current could be used to recharge its source.

7.4.3 Subsystem Architecture

The monopod subsystem made use of a secondary *Arduino Mega* microcontroller to pass data between the system master and the motor controller. This microcontroller was used as it was on hand and had the requisite number of serial ports. The microcontroller pass-through was done due to the large packet size used by the ODrive overloading the serial buffer on the system master when it was directly connected. The use of this pass-through microcontroller allowed for a custom data packet structure defined based on the needs of this system. This custom packet significantly reduced the serial packet size sent from the system master as the full functionality of the motor-controller wasn't required during normal operations. Additionally, this pass-through microcontroller had a shared connection to the motor encoder. This connection allowed it to read the position of the motor without having to request it from the controller, further reducing communications overhead. This reduction is seen by the fact that the master system sent a 5 byte packet to the pass-through microcontroller while the pass-through microcontroller sent a 20 byte packet to the motor controller.

In addition to the motor communications the pneumatic cylinder position data was transmitted across the boom as a $4 - 20\ mA$ signal. This was then converted to a $0 - 3\ V$ analogue signal at the system master where it was read as an analogue voltage. Similarly, the control of the pneumatic solenoid was handled directly through the use of a digital output from the system master.

7.5 Controller Design

For the controller, state machines were used for both the vertical hopping and fixed body tests. These two controllers were slightly different with the vertical hopping state machine being focused on predicting the fire height of the leg while the forward controller was focused on the launch and land angles for the leg. Flowcharts for these controllers can be seen in Figure 7.11 below.

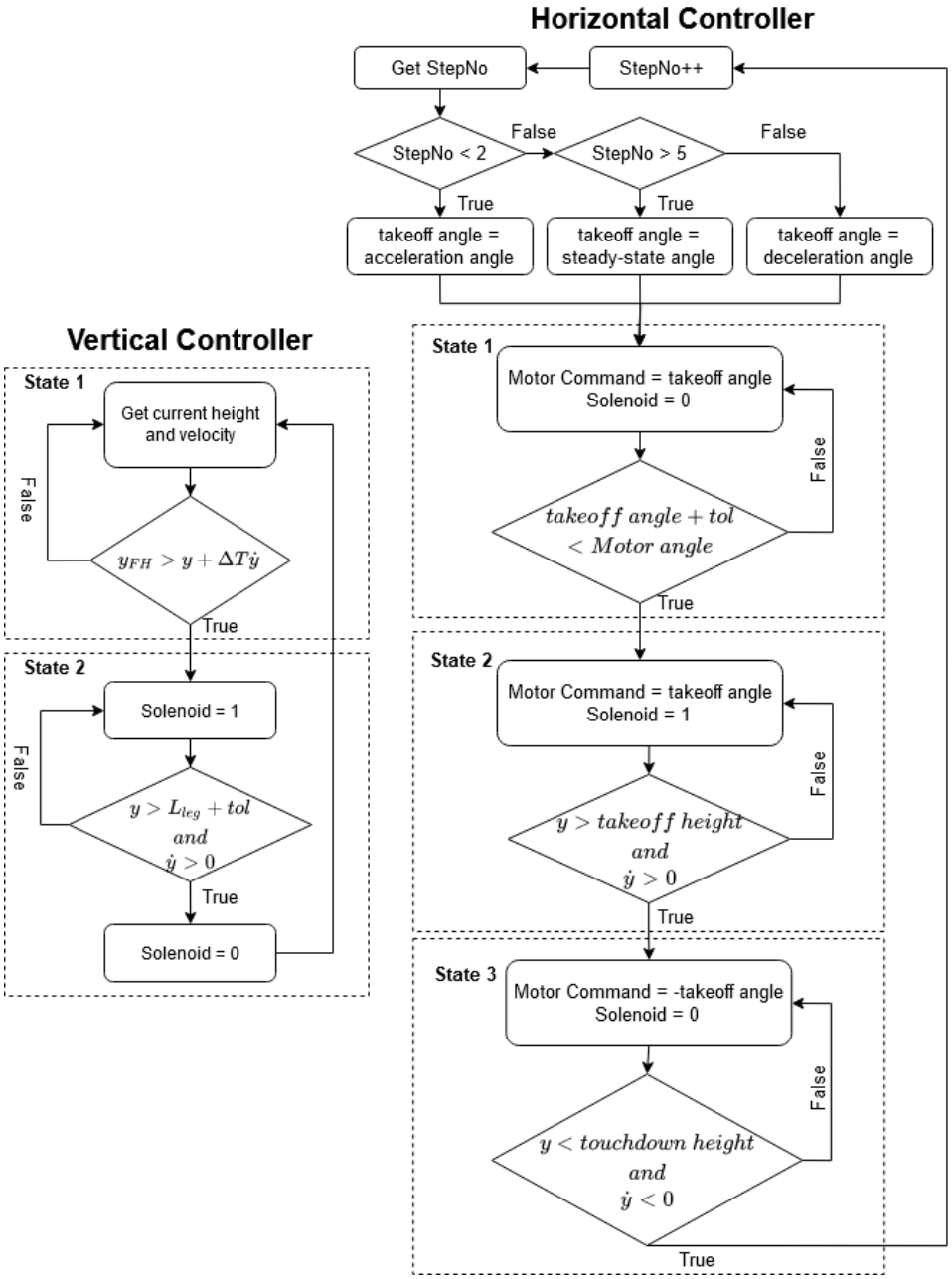

Figure 7.11: Vertical and Horizontal Controllers implemented on the platform.

The vertical hopping controller functioned by checking for the expected height of the system at a time 8.3 ms in the future to compensate for the firing delay of the solenoid (shown as ΔT in the flow chart). If the cylinder was below its programmed fire height the solenoid was activated pressuring the cylinder. The solenoid was only deactivated once the Kalman Filter reported a height that placed the system slightly off the ground while also having a positive vertical velocity. Once the cylinder was deactivated the system would loop back into its predict phase where it checked for the fire height and would continue to loop in this manner until the kill button was pressed.

The state machine used for the forward hopping tests was similar to the one used for the HA simulations and was shown in Figure 5.9. The largest difference in this implementation was that the launch angle was varied based on which number hop was occurring. This allowed for more aggressive lunch angles in the acceleration phase with shallower angles during steady-state and deceleration phases.

7.6 Summary

The sensors in the system were limited primarily based on the short duration of the hops as this necessitated sensors with high update rates. This requirement for fast update rates resulted in the selection of sensor with lower accuracies. To compensate for this additional system states were measured to allow for the use of a multivariate Kalman Filter. This Kalman Filter gave significant improvement to the accuracy of these measurements increasing accuracy by 63.6%.

The sensors on the platform were based around the measurement of the states of the actuators. These actuators were in turn driven through the use of actuator specific drives run by the system master.

The system master handled the flow of data through the system and out of it to the logging PC. In addition to this responsibility, it was required to compute the Kalman Filter states and run the controller.

Chapter 8: Experiments and Results

For the validation of the platform and to test its accuracy to simulated data, several different tests needed to be conducted. These test could be broken into two subsets with the first being concerned with the platforms vertical performance and the second being concerned with its horizontal performance.

The first test was vertical agility testing based on a single hop from a stationary position. This test was done to compare to the simulated vertical agility of the platform from Section 5.3.1.1. The second vertical test was a continuous hopping test, this test was done to test the validity of using firing height as proxy control for the hop height of the system.

The first horizontal test was similar to the first vertical test as it was primarily concerned with its adherence to the simulated horizontal agility for the platform. The final test conducted was concerned with the platforms suitability for use in transient manoeuvres and to that end comprised of long time-horizon testing consisting of acceleration, steady state and finally deceleration.

8.1 General Testing Procedure

Each test was conducted with the safety of the operator being paramount with the secondary aim of ensuring the platform wouldn't be damaged. To achieve this each new test was initially run on a tether until the test case was ensured to be safe for both the operator and the robot. This tether was run to a pulley on the ceiling, so that an assistant could pull the robot off the ground to safety in the event of a failure, this can be seen in Figure 8.1 below. Once the test was found to be safe, it was rerun off of the tether to remove any external effects caused by the tether on the system dynamics.

Figure 8.1: Testing procedure with safety rope and testing assistant.

For each test, the system was powered on while held in the air away from the operator. Once all subsystems were powered on the system master was connected to the PC and the logging program in Matlab was started. Following this, the system was placed on the ground and a button was pressed to start the initialisation sequence. This initialisation was used to zero the various relative sensors and get the initial value state for the Kalman Filter using an average of 10 sensor readings.

Once the initialisation sequence was complete, the debug light on the Teensy turned off to show the system was waiting for a start command. Once the start button was pressed, system logging began and the system master started running the controller. This was continued until a stop button was pressed where the system went to a safe state with the motor outputting zero torque and the solenoid set to low.

Through all of the above, safety for the operator was the priority. This was due to the risk the rapidly moving solid masses that made up the system created.

8.2 Vertical Agility Test

For the vertical agility test, the platform was constrained to be vertical and move only in the y direction. This was done by locking off the pitch joint at the end of the boom and the joint allowing motion in the x direction to prevent motion in these degrees of freedom.

The vertical agility test was conducted in a similar manner to the hop-up tests seen in Section 4.3. The main difference between these test was the use of the boom and the additional mass that this and the platform entailed.

The results of this test compared to the simulated vertical agility of the platform can be seen in Figure 8.2. Due to the change in mass from the estimate used in the mechanical simulations to the platform as-tested, the Vertical Agility simulations were re-run with accurate masses and inertias. This simulation result was also plotted and can be seen compared to the original in Figure 8.3.

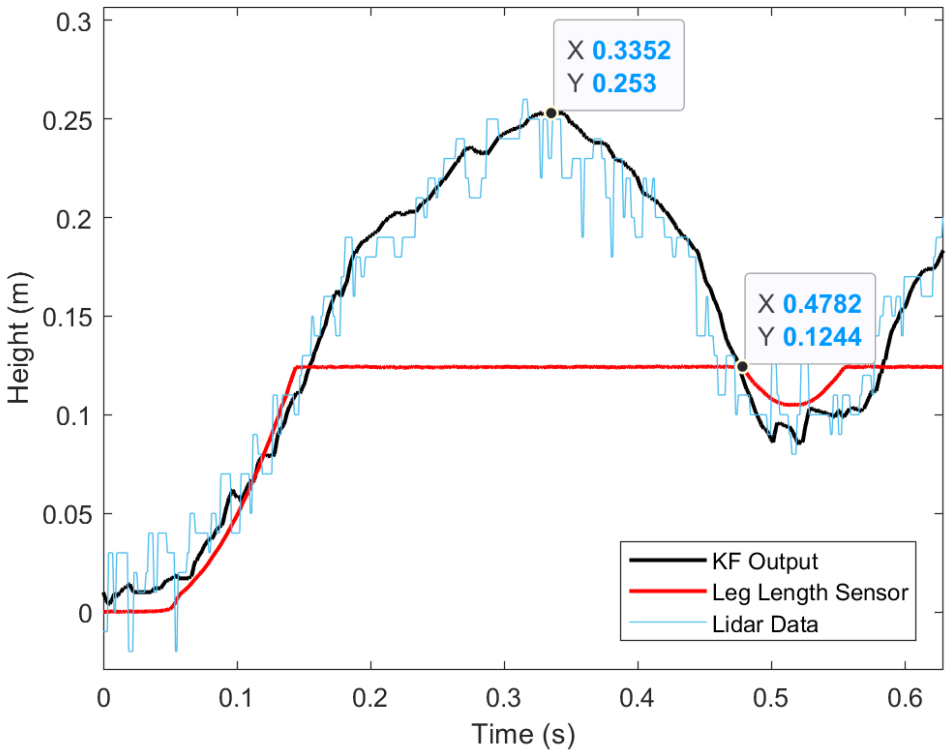

Figure 8.2: VA test for the full platform mounted on the boom.

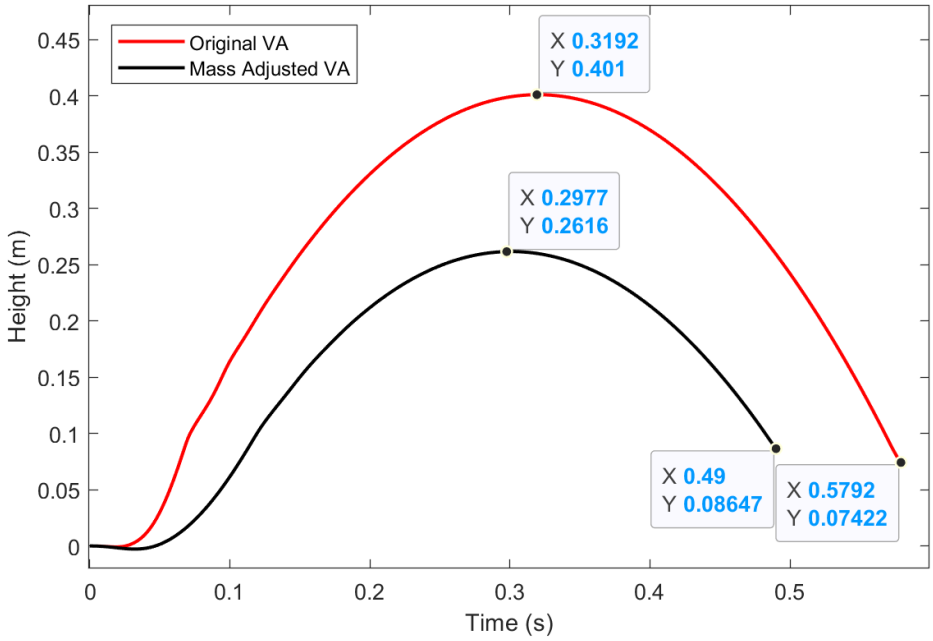

Figure 8.3: Position time plots for the original VA sim and a later one adjusted for the final mass of the system.

From the figure above, the vertical agilities of the system could be calculated. The VA score for the monopod was found to be 0.529 m/s, which differed from the originally anticipated Vertical Agility score for this system of $0.692 m/s$. When the simulated system was adjusted for the final masses on the platform it provided a significantly closer score of $0.534 m/s$.

The discrepancy between the original and mass adjusted score was primarily due to the neglecting of the boom mass in the design of the leg. This mass was originally neglected to make the robot independent of its support. However, this boom mass was not insignificant and had a marked effect on the performance of the final platform. The adherence of the model to the real platform once the correct parameters were set shows robustness in the system model even under different loading cases with the mass corrected simulation carrying a significantly greater load than anything tested in the design of the model.

8.3 Continuous Vertical Hopping Test

In addition to the Vertical Agility hop-up tests, continuous hopping tests with variable heights were conducted similar to those seen in Section 4.3.2. In this case, the hop height tests were based on the height of the system when the cylinder was fired rather than the time in contact with the ground. Fire heights from $20cm - 3cm$ above the ground were tested with the notable fire height tests being discussed in more detail.

This fire height and delayed height can be seen in Figure 8.4. The system lands fully extended and vented with the length of the leg at firing being a product of the fire height and the delay while collapsing under gravity.

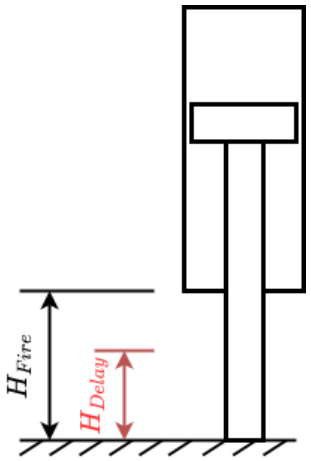

Figure 8.4: Height of the system when the fire command is sent vs when the solenoid is activated. The system is only check for firing when $\dot{H}_{fire}$ is negative

The first notable fire height was $18cm$ as any fire heights above this resulted in only a single hop as the system did not vent enough to reset. At a fire height of $18cm$, multiple hops were possible but the hop height decayed as the max hop height decreased with each subsequent hop. Due to this decrease in the maximum hop height velocity and kinetic energy on landing also decreased. This decrease in energy on landing meant that the cylinder collapsed less on each subsequent hop, less energy could therefore be imparted from the actuator until cylinder failed to sufficiently leave the ground and remained fully extended. The results of this test can be seen in Figure 8.5 below:

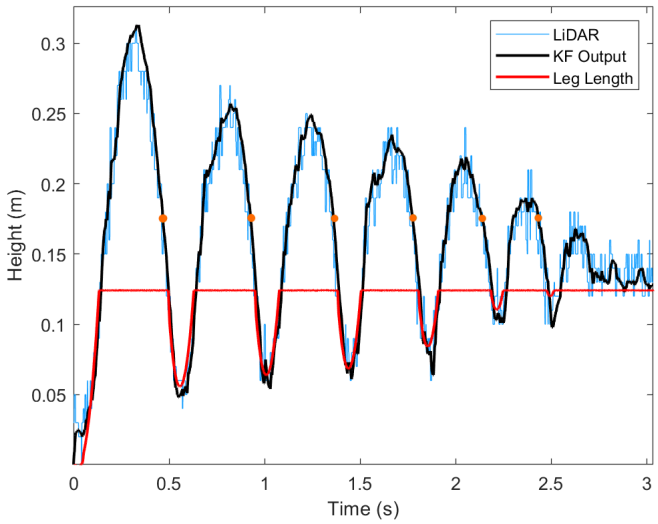

Figure 8.5: Hop height plot for continuous hopping with a fire height of 18 *cm*. The firing command was sent at the point denoted with an orange dot.

For fire heights below 16*cm*, the decay in the hop height for the system was asymptotic to a value greater than its open length. This was a similar result to what was seen in the continuous hopping tests in Section 4.3.2 and showed that hop height trends to a consistent value based on the fire height in a steady-state system. For fire heights between 16*cm* and 13*cm* the system hopped to a height lower than its initial stationary start hop as seen in Figure 8.6 below:

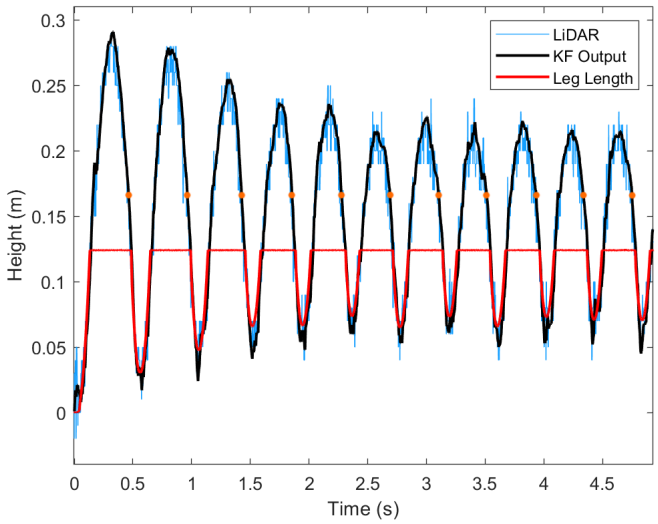

Figure 8.6: Hop height plot for continuous hopping with a fire height of 16 *cm*. The firing command was sent at the point denoted with an orange dot.

For fire heights below 13 *cm*, the maximum hop height on subsequent jumps was greater than the height of a stationary hop. This was likely due to an increase in the maximum pressure of the cylinder due to the kinetic energy of the cylinder compressing the air in the cylinder above its normal maximum. This additional hop height can be seen in Figure 8.7. It should be noted in this figure the output height from the Kalman Filter was less stable and at points give a negative output. This was due to the higher than normal impact force due to the cylinder reaching its fully compressed state. This impact significantly exceeded the readable range of the acclerometer causing this poor tracking of the Kalman Filter.

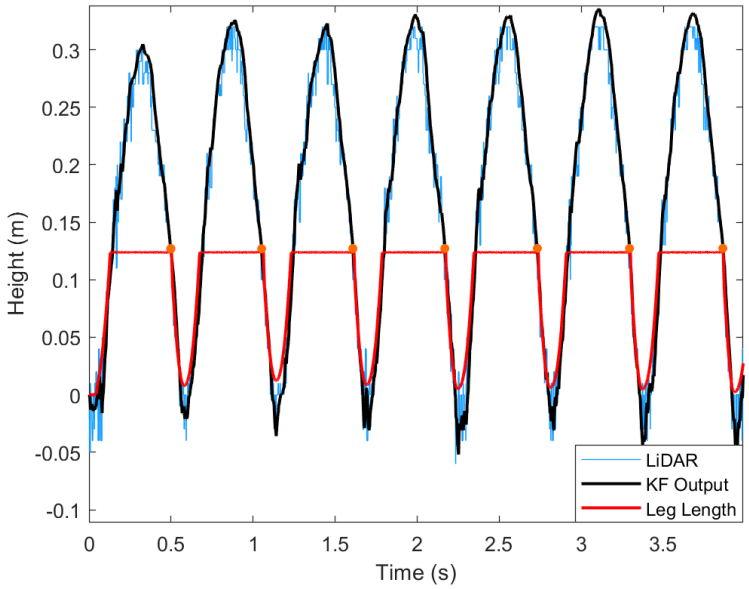

Figure 8.7: Hop height plot for continuous hopping with a fire height of 13 *cm*. The firing command was sent at the point denoted with an orange dot.

The final fire height of interest for the system was 9 *cm*. This value was important as any fire height below this results in a full collapse of the cylinder. This limited the system and could potentially damage it due to the high shock loads when allowed to fully compress. Furthermore, the high shock load paired with the limitation on the reading scale for the accelerometer for the Kalman Filter caused some amount of disturbance in the filter on landing. This disturbance resulted in significant inaccuracy and the decision to only use the SDAT leg length sensor when in contact with the ground. This hop can be seen in Figure 8.8 below:

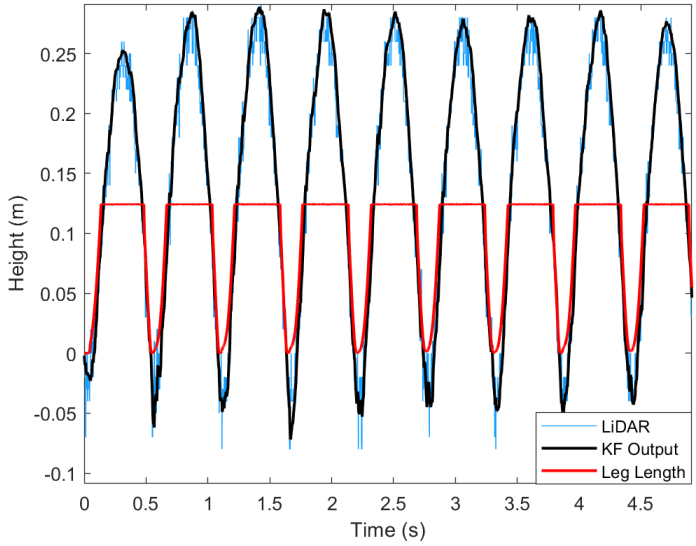

Figure 8.8: Hop height plot for continuous hopping with a fire height of 9 *cm*.

Once data had been collected for all the vertical test cases, a comparison to other platforms in terms of vertical agility was conducted. This comparison can be seen in Figure 8.9 below.

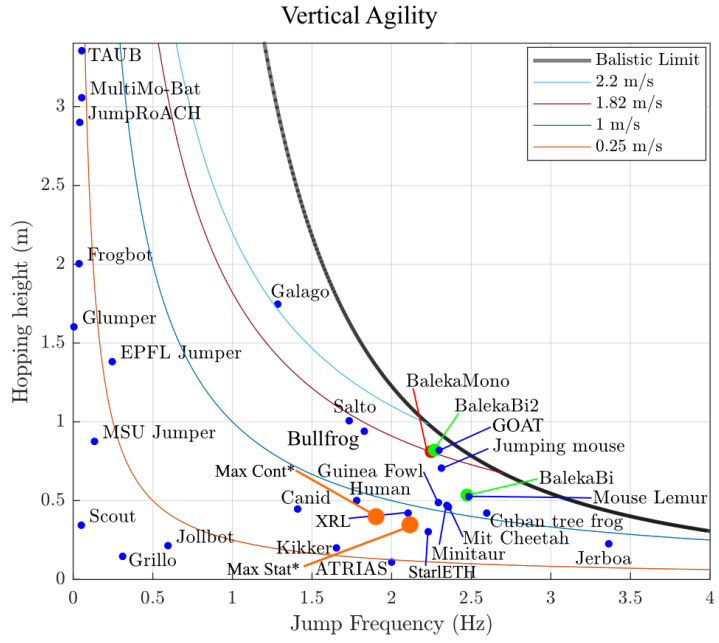

Figure 8.9: Comparison of different platforms in terms of vertical agility. The Monopod robot's results being seen in orange with a ***Max Stat*** depicting the maximum vertical agility from stationary and ***Max Cont*** representing the score for the maximum height continuous hop. This plot was adapted from [39] originally from [90].

In terms of Vertical Agility, the platforms managed to outperform several other platforms including other prismatic platforms such as SCOUT. This is especially notable when considering that the support system for this test was not optimised for vertical hopping testing and observably impacted the vertical agility of the platform. Furthermore, this metric is biased against this robot as only one of the two actuators was used in this test and therefore under-represents the performance of this system.

The vertical hopping of the platform can be seen in Figure 8.10 below. This image shows how the platform moves in space.

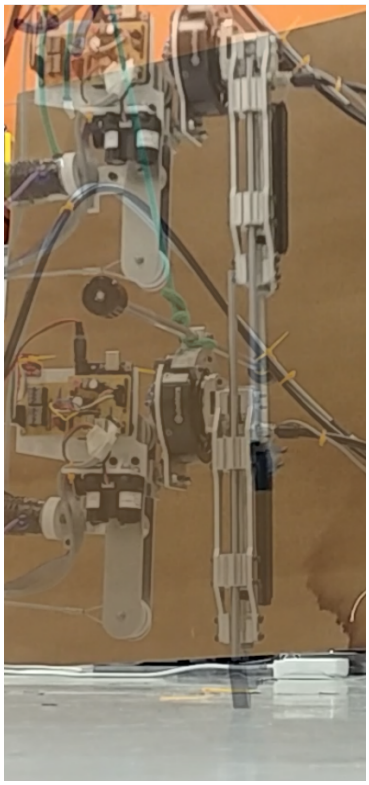

Figure 8.10: Vertical Hopping of the Robot shown through superimposed frames from testing videos

8.4 Horizontal Agility Test

For the horizontal agility testing, the same system as for the vertical tests was used, however, in this case, the clamp locking the motion of the boom in the x direction was removed and the controller was changed over. The data from the encoder measured to approximate the motion in the x direction was used in conjunction with the accelerom-

eter to run a Kalman Filter over the logged data. This was done after the fact in this case as the horizontal data was not used in the controller and post-processing reduced the computational load on the microcontroller. Horizontal Agility hopping tests were conducted with launch angles from 5° to 10°, as angles beyond this were considered to be too large for fixed body testing on the boom to be safe or effective. This safety concern was due to concerns over the large torque forces beyond this point potentially damaging the boom. The results from the boundary launch angles tested can be seen in Figures 8.11 and 8.12 below:

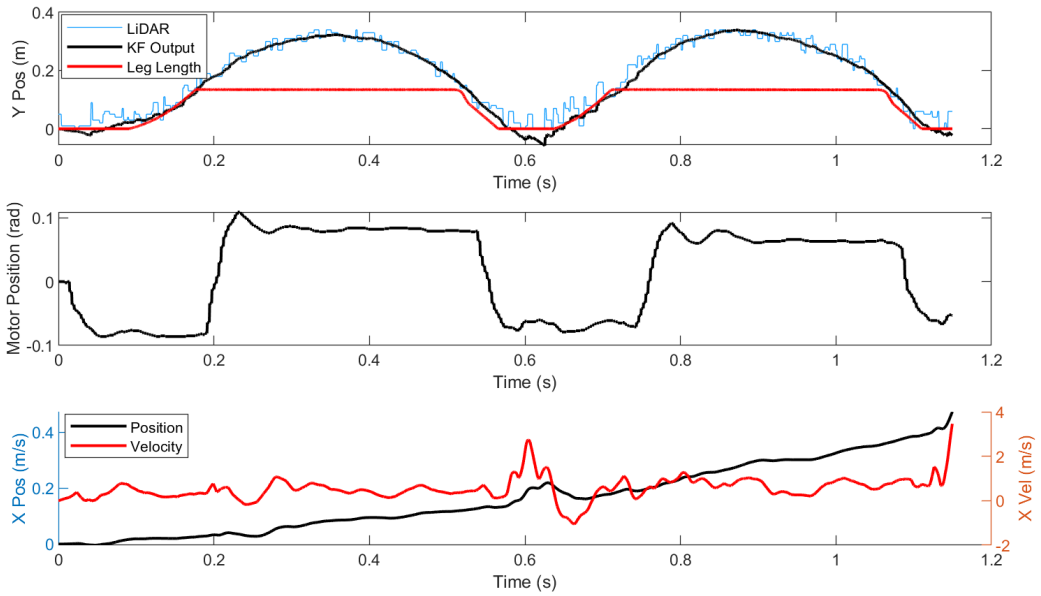

Figure 8.11: Horizontal Agility Hops with a launch angle of 5°.

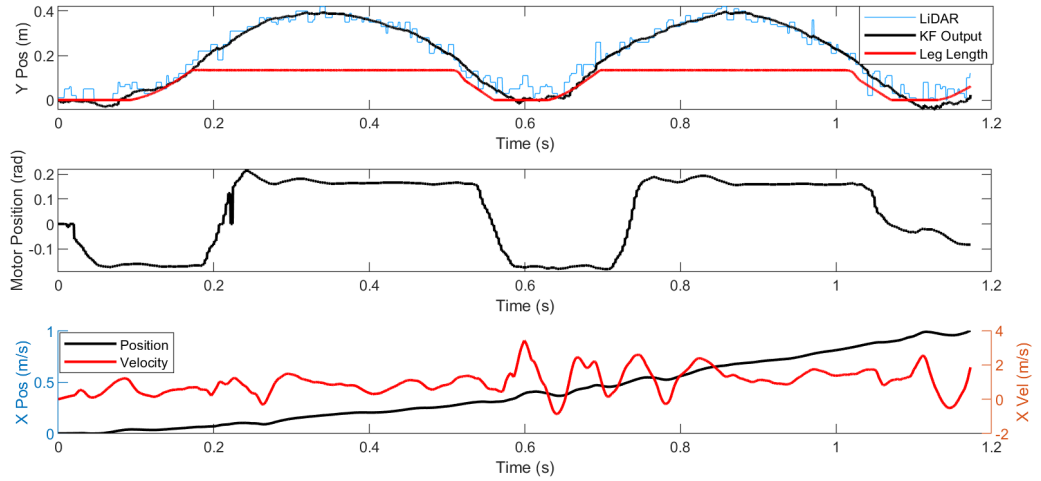

Figure 8.12: Horizontal Agility Hops with a launch angle of 10°.

From the plots above (and the additional test data not pictured) a full plot for horizontal agility versus launch angle could be generated. This was done for both the HA1 and HA2 metrics as described in Section 5.3.2. This data can be seen in Figure 8.13 below:

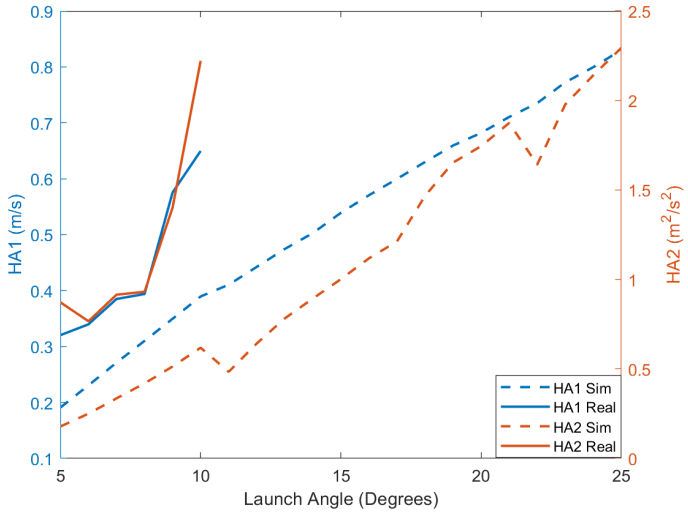

Figure 8.13: Horizontal Agility Plots versus angle for the system. The measured values are plotted with solid lines while the simulated values are plotted with dashed lines.

From the plots above it was seen that both HA1 and HA2 were larger than their expected values from simulation though still in the range of possible horizontal agilities for the system. The highest measured values for HA1 and HA2 occurred at the 10° launch angle test and corresponded to values of 0.65 m/s and 2.22 m^2/s^2 respectively. The simulated values for this launch angle were 0.38 m/s for HA1 with a corresponding value of 0.606 m^2/s^2 for HA2.

8.5 Transient Manoeuvres

The final set of tests conducted were for long time horizon horizontal hopping. This was conducted with a fixed body on the robot to reduce the scope of the control problem with the same controller as used in the Horizontal Agility tests being used again. The difference, in this case, was that during this test the launch angle used was set based on the number of the hops that had already occurred. For this testing, one acceleration step was used followed by four steady-state steps and finally two deceleration steps.

The magnitude for the launch angles was set empirically using more conservative values than were observed in simulation. The acceleration step was set through a sweep from 5° to 10°. The steady-state steps were set to the highest angle that was repeatable for multiple steps, which was tested by running the robot on a tether and observing when a failure occurred. Once the highest stable angle was found validation tests were conducted off of the tether.

The most aggressive stable gait was found to have an acceleration step of 8° followed by steady-state steps of 5° and finally deceleration steps of 1°. The results of this test can be seen in Figure 8.14 below while other test results can be seen in Appendix E.

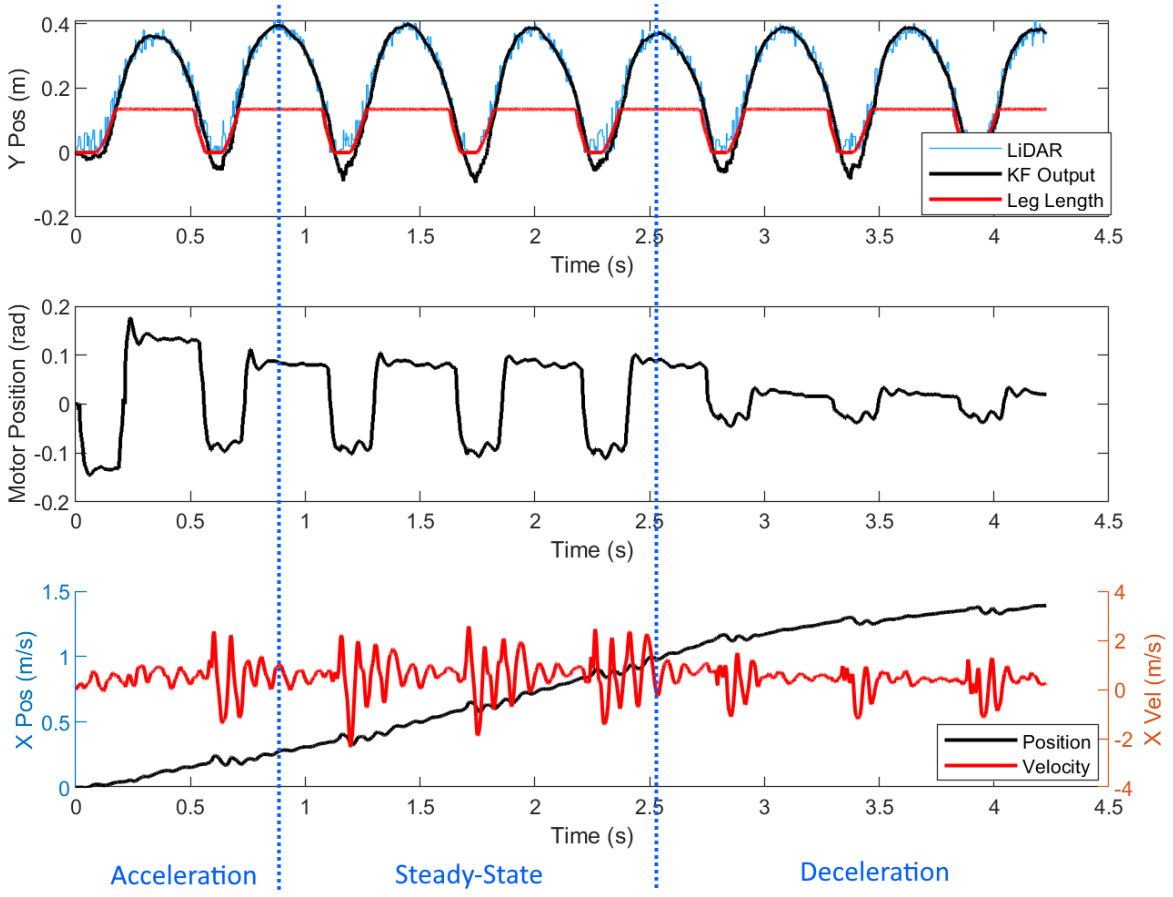

Figure 8.14: Long time horizon hopping test with an initial launch angle of 8°

A video of this test can be seen as https://youtu.be/iJDS-UnmrPo.

8.6 Summary

The objective of this project was to construct a prismatic pneumatic monopod for rapid acceleration. Testing was conducted on this final platform in both in the vertical and planar case with both demonstrating the viability of the platform. In the vertical case, the height of the system at firing could be used as a proxy method for control of the height of the platform in the steady-state case. This was observed to be impractical for transient control as the previous-hop height was coupled to the subsequent hop height when using the fire height command system.

In addition to the control system, the Kalman Filter could be seen to work admirably, reducing the noise from the LiDAR and giving a velocity state for use in the prediction of the fire height of the platform. The KF was relatively stable only losing tracking when the cylinder collapsed to its solid height as the acceleration greatly exceeded the reading limit on the accelerometer and had stabilised by the time the robot left the ground.

The horizontal agility for the platform exceeded the expected results from simulation. This was not necessarily due to better performance of the platform but rather the author believes that this was due to torsional deflection in the boom resulting in a launch angle greater than what was commanded or expected.

As a by-product of the other testing conducted the robustness was tested as the system endured several thousand hop cycles. During this time none of the parts on the system failed and managed to survive multiple crashes. This showed that the platform met its initial robustness specification.

Chapter 9: Conclusions and Recommendations

9.1 Conclusions

The aim of this project was to create a platform for use in legged robotics making use of pneumatic actuators. This required not only the mechanical construction of this platform but of several test rigs, design simulations as well as a full embedded system to control the platform. The measure for the success of this system was its adherence to the requirements for the platform but further it was compared to other robots and simulations of the platform used in its design.

Initially hopping tests were conducted on a pneumatic cylinder seen in Chapter 4. These test were used to develop robust models for the cylinders. These models were tailored to the system as implemented and were used throughout the rest of the project. These models aided in the actuator selection in 5.3 and the simulated testing for the Kalman Filter. This model was further validated by the accuracy of the model to hopping tests outside of its original load case, a fact seen through the relatively small error ($< 1\%$) between simulated and real data for the Vertical Agility tests in seen Section 8.2.

The leg was designed to be as lightweight and modular as possible. This weight constraint was largely met with the full platform only weighting 1.53 kg, however, this was limited by the large mass of the support structure of the piston rod. The modularity requirement was met through the use of bolted joints between parts and discreet sub-assemblies. These factors would allow different leg or body configurations without a full redesign of the platform.

Additional structures were constructed to aid in testing, these being a linear test rig and a boom. The boom posed a significant design challenge in trying to reduce its mass

while maintaining rigidity. The cable stayed technique implemented for this purpose dramatically increased the stiffness of the boom arm. Additional use of tension cables allowed for the construction of a 4 bar linkage boom with only 1 rigid bar - further reducing the weight of the boom.

To find the position of the platform in space accurately, a sensor system was created. This system made use of a LiDAR and accelerometer which were fused through the use of a Kalman Filter. This filer improved the accuracy of the position measure of the system by 66.8% allowing for more fine control of the system.

The system itself was found to be valid through testing as it was capable of running horizontally in a controlled manner. In addition to this the performance of the system was evaluated against other robots using Vertical Agility as a mark of performance. This metric was biased against prismatic designs, however, this robot was found to out perform other prismatic platforms such as SCOUT.

In addition to the performance metrics for success, the less measurable metrics of ease of assembly and robustness were also met. This ease of assembly was seen from the easy access to almost all of the parts with it taking less than an hour to strip or assemble the platform. The robustness of the system was demonstrated through the fact that the platform was run for an excess of 1000 cycles between the testing conducted for this thesis and that of a PhD student also making use of the platform, during which none of the parts failed. This combined with the previous validation of the systems performance showed that the system was successful in its goal of being a good platform used to test controllers and transient maneuvers.

Recommendations

Though the robot was considered a success, it and its support structure were a first prototype and not without flaws. The first and most significant recommendation is to build the double-link design simulated in Section 5.3. This platform not only showed improved performance in simulation but could also reduced the weight of the platform as the support structure used by the prismatic system wouldn't be required. Any addi-

tional complexity due to the rotating reference frames of the leg might be offset by the performance improvements.

The boom could also be improved, as although it performed admirably given the constraints placed on it, it was still sub-optimal. The boom under-performed in both weight and rigidity metrics. It is the Author's belief that both of these could be improved by using a different material for the boom. A boom arm made from composite materials such as commonly available Carbon Fiber tubing would allow for a lighter and stiffer boom. Furthermore, this change would also give the boom more resistance to torque loads therefore improving the accuracy of fixed body testing. This was originally not used due to 2 m lengths of tubing not being available for purchase and difficulty finding a supplier that could produce a part so large. Therefore to implement this shorter tube lengths should be procured and joined using custom clamping joints or some similar method.

The Author felt that changes might also be made to the actuator drives with both having improvements that can be made. The pneumatic driver systems should be altered to measure the pressure in the cylinder to allow for better transient control. This pressure measurement could be used in conjunction with height measurements to allow for accurate transient control. Additionally more solenoid valves could be used with different supply pressures to further increase control. At a minimum, a second valve should be added to be able to command a contraction of the cylinder. The Author recommends doing this with a second 3/2 valve to increase the number of pneumatic states in the system and to not negatively impact performance by having direct state changes with no time to vent the cylinder.

The motor driver was also not without fault. The unnecessarily large UART package size necessitated the use of a microcontroller purely to pass data to the ODrive. As the ODrive is an open-source piece of hardware the author recommends that a custom firmware version is made with smaller UART package sizes. As this device is still receiving updates it is possible that ODrive themselves implement this. This could also be avoided by changing the communications protocol used from UART to CAN if this feature becomes better developed in future firmware releases.

Future work using this platform should attempt to compare the double link and single cylinder designs from real data. Furthermore, the leg designed should be tested in a planar quadruped or biped configurations. This type of test could leverage the modularity of the platform to compare the efficacy of these different configurations without having the leg itself as a factor.

Bibliography

[1] "SABS - ACCESSIBILITY & DISABILITY - STANDARDS & PUBLICATIONS." [Online]. Available: https://www.sabs.co.za/Sectors-and-Services/Services/Access/access_sp.asp

[2] "Policies, frameworks and tools." [Online]. Available: https://gsdrc.org/topic-guides/disability-inclusion/policies-frameworks-and-tools/

[3] S. Salman, "What would a truly disabled-accessible city look like?" *The Guardian*, Feb. 2018. [Online]. Available: https://www.theguardian.com/cities/2018/feb/14/what-disability-accessible-city-look-like

[4] "7 Times Honda's Asimo Bot Showed Off Its Skills, and Once When It Didn't," Jul. 2018, library Catalog: www.digitaltrends.com Section: Emerging Tech. [Online]. Available: https://www.digitaltrends.com/cool-tech/7-times-hondas-asimo-bot-showed-off-its-skills/

[5] P. . N. . |. . GMT, "How Boston Dynamics Is Redefining Robot Agility - IEEE Spectrum," library Catalog: spectrum.ieee.org. [Online]. Available: https://spectrum.ieee.org/robotics/humanoids/how-boston-dynamics-is-redefining-robot-agility

[6] C. Hubicki, J. Grimes, M. Jones, D. Renjewski, A. Spröwitz, A. Abate, and J. Hurst, "ATRIAS: Design and validation of a tether-free 3D-capable spring-mass bipedal robot:," *The International Journal of Robotics Research*, Jun. 2016, publisher: SAGE PublicationsSage UK: London, England. [Online]. Available: https://journals.sagepub.com/doi/10.1177/0278364916648388

[7] R. Alexander, G. Maloiy, R. Njau, and A. Jayes, "Mechanics of running of the Ostrich (Struthio Camelus)," *Journal of Zoology*, vol. 187, pp. 169–178, Aug. 2009.

[8] A. M. Wilson, J. C. Lowe, K. Roskilly, P. E. Hudson, K. A. Golabek, and J. W. McNutt, "Locomotion dynamics of hunting in wild cheetahs," *Nature*, vol. 498, no.

7453, pp. 185–189, Jun. 2013, number: 7453 Publisher: Nature Publishing Group. [Online]. Available: https://www.nature.com/articles/nature12295/

[9] R. J. Full and R. B. Weinstein, "Integrating the Physiology, Mechanics and Behavior of Rapid Running Ghost Crabs: Slow and Steady Doesn't Always Win the Race," *American Zoologist*, vol. 32, no. 3, pp. 382–395, Jun. 1992. [Online]. Available: https://academic.oup.com/icb/article-lookup/doi/10.1093/icb/32.3.382

[10] W. C. Flannigan, G. M. Nelson, and R. D. Quinn, "Locomotion controller for a crab-like robot," in *Proceedings. 1998 IEEE International Conference on Robotics and Automation (Cat. No.98CH36146)*, vol. 1, May 1998, pp. 152–156 vol.1, iSSN: 1050-4729.

[11] S. Cotton, I. M. C. Olaru, M. Bellman, T. v. d. Ven, J. Godowski, and J. Pratt, "FastRunner: A fast, efficient and robust bipedal robot. Concept and planar simulation," in *2012 IEEE International Conference on Robotics and Automation*, May 2012, pp. 2358–2364, iSSN: 1050-4729.

[12] K. Weinmeister, P. Eckert, H. Witte, and A. Ijspeert, "Cheetah-cub-S: Steering of a quadruped robot using trunk motion," in *2015 IEEE International Symposium on Safety, Security, and Rescue Robotics (SSRR)*, Oct. 2015, pp. 1–6.

[13] C. Fisher, S. Shield, and A. Patel, "The effect of spine morphology on rapid acceleration in quadruped robots," in *2017 IEEE/RSJ International Conference on Intelligent Robots and Systems (IROS)*, Sep. 2017, pp. 2121–2127.

[14] C. Hubicki, M. Jones, M. Daley, and J. Hurst, "Do limit cycles matter in the long run? stable orbits and sliding-mass dynamics emerge in task-optimal locomotion," in *2015 IEEE International Conference on Robotics and Automation (ICRA)*, 2015, pp. 5113–5120.

[15] I. Poulakakis and J. W. Grizzle, "Modeling and control of the monopedal robot Thumper," in *2009 IEEE International Conference on Robotics and Automation*, May 2009, pp. 3327–3334, iSSN: 1050-4729.

[16] B. Katz, J. D. Carlo, and S. Kim, "Mini Cheetah: A Platform for Pushing the Limits of Dynamic Quadruped Control," in *2019 International Conference on Robotics and Automation (ICRA)*, May 2019, pp. 6295–6301, iSSN: 2577-087X.

[17] G. Wiedebach, S. Bertrand, T. Wu, L. Fiorio, S. McCrory, R. Griffin, F. Nori, and J. Pratt, "Walking on partial footholds including line contacts with the humanoid robot atlas," in *2016 IEEE-RAS 16th International Conference on Humanoid Robots (Humanoids)*, Nov. 2016, pp. 1312–1319, iSSN: 2164-0580.

[18] J. Pransky, "AIBO – the No. 1 selling service robot," *Industrial Robot: An International Journal*, vol. 28, no. 1, pp. 24–26, Feb. 2001. [Online]. Available: https://www.emerald.com/insight/content/doi/10.1108/01439910110380406/full/html

[19] A. Patel and M. Braae, "An Actuated Tail Increases Rapid Acceleration Manoeuvres in Quadruped Robots," *Lecture Notes in Electrical Engineering*, vol. 313, pp. 69–76, Jan. 2015.

[20] R. J. Full, T. Kubow, J. Schmitt, P. Holmes, and D. Koditschek, "Quantifying Dynamic Stability and Maneuverability in Legged Locomotion," *Integrative and Comparative Biology*, vol. 42, no. 1, pp. 149–157, Feb. 2002, publisher: Oxford Academic. [Online]. Available: https://academic.oup.com/icb/article/42/1/149/559954

[21] R. Tedrake, "Underactuated Robotics: Algorithms for Walking, Running, Swimming, Flying, and Manipulation (Course Notes for MIT 6.832)." [Online]. Available: http://underactuated.mit.edu/

[22] J. Meyer and A. Guillot, "Biologically inspired robots," in *Springer Handbook of Robotics*, B. Siciliano and O. Khatib, Eds. Springer, 2008, pp. 1395–1422. [Online]. Available: https://doi.org/10.1007/978-3-540-30301-5_61

[23] M. Travers and H. Choset, "Bioinspired robots: Examples and the state of the art," Feb. 2018, library Catalog: www.sciencemag.org. [Online]. Available: https://www.sciencemag.org/bioinspired-robots-examples-and-state-art

[24] J. Clark, D. Goldman, P.-C. Lin, G. Lynch, T. Chen, H. Komsuoglu, R. Full, and D. Koditschek, "Design of a bio-inspired dynamical vertical climbing robot," 06 2007.

[25] S. Seok, A. Wang, M. Y. Chuah, D. J. Hyun, J. Lee, D. M. Otten, J. H. Lang, and S. Kim, "Design Principles for Energy-Efficient Legged Locomotion and Implementation on the MIT Cheetah Robot," *IEEE/ASME Transactions on Mechatronics*, vol. 20, no. 3, pp. 1117–1129, Jun. 2015, conference Name: IEEE/ASME Transactions on Mechatronics.

[26] J. Pratt and G. Pratt, "Intuitive control of a planar bipedal walking robot," in *Proceedings. 1998 IEEE International Conference on Robotics and Automation (Cat. No.98CH36146)*, vol. 3, May 1998, pp. 2014–2021 vol.3, iSSN: 1050-4729.

[27] B. Miripour-Fard, *Climbing and Walking Robots*. BoD – Books on Demand, Mar. 2010, google-Books-ID: t_ugDwAAQBAJ.

[28] M. H. Raibert and I. E. Sutherland, "Machines That Walk," *Scientific American*, vol. 248, no. 1, pp. 44–53, 1983. [Online]. Available: https://www.jstor.org/stable/24968806

[29] M. H. Raibert, *Legged Robots that Balance*. MIT Press, 1986, google-Books-ID: EXRiBnQ37RwC.

[30] I. Uyanık, O. Morgul, and U. Saranli, "Experimental Validation of a Feed-Forward Predictor for the Spring-Loaded Inverted Pendulum Template," *IEEE Transactions on Robotics*, vol. 31, no. 1, pp. 208–216, Feb. 2015, conference Name: IEEE Transactions on Robotics.

[31] J. W. Hurst, J. E. Chestnutt, and A. A. Rizzi, "Design and Philosophy of the BiMASC, a Highly Dynamic Biped," in *Proceedings 2007 IEEE International Conference on Robotics and Automation*. Rome, Italy: IEEE, Apr. 2007, pp. 1863–1868, iSSN: 1050-4729. [Online]. Available: http://ieeexplore.ieee.org/document/4209357/

[32] M. Raibert, M. Chepponis, and H. Brown, "Running on four legs as though they were one," *IEEE Journal on Robotics and Automation*, vol. 2, no. 2, pp. 70–82, Jun. 1986.

[33] R. Altendorfer, U. Saranli, H. Komsuoglu, D. Koditschek, H. Brown, M. Buehler, N. Moore, D. McMordie, and R. Full, "Evidence for spring loaded inverted pendulum running in a hexapod robot," in *ISER*, 2000.

[34] S. Seok, A. Wang, M. Y. Chuah, D. Otten, J. Lang, and S. Kim, "Design principles for highly efficient quadrupeds and implementation on the MIT Cheetah robot," in *2013 IEEE International Conference on Robotics and Automation*, May 2013, pp. 3307–3312.

[35] C. Fisher, A. Blom, and A. Patel, "Baleka: A Bipedal Robot for Studying Rapid Maneuverability," *Frontiers in Mechanical Engineering*, vol. 6, p. 54, Jul. 2020. [Online]. Available: https://www.frontiersin.org/article/10.3389/fmech.2020.00054/full

[36] N. Kau, A. Schultz, N. Ferrante, and P. Slade, "Stanford Doggo: An Open-Source, Quasi-Direct-Drive Quadruped," in *2019 International Conference on Robotics and Automation (ICRA)*. Montreal, QC, Canada: IEEE, May 2019, pp. 6309–6315. [Online]. Available: https://ieeexplore.ieee.org/document/8794436/

[37] G. Kenneally, A. De, and D. E. Koditschek, "Design Principles for a Family of Direct-Drive Legged Robots," *IEEE Robotics and Automation Letters*, vol. 1, no. 2, pp. 900–907, Jul. 2016.

[38] J. M. Duperret and D. E. Koditschek, "An empirical investigation of legged transitional maneuvers leveraging Raibert's Scissor algorithm," in *2015 IEEE International Conference on Robotics and Biomimetics (ROBIO)*, Dec. 2015, pp. 2531–2538.

[39] A. F. Blom, "Design of a bipedal robot for rapid acceleration and braking manoeuvres," 2019, accepted: 2020-02-14T08:37:33Z Publisher: Engineering and the Built Environment. [Online]. Available: https://open.uct.ac.za/handle/11427/31116

[40] K. Graichen, S. Hentzelt, A. Hildebrandt, N. Kärcher, N. Gaißert, and E. Knubben, "Control design for a bionic kangaroo," *Control Engineering Practice*, vol. 42, pp. 106–117, Sep. 2015. [Online]. Available: http://www.sciencedirect.com/science/article/pii/S0967066115000957

[41] M. P. Murphy, A. Saunders, C. Moreira, A. A. Rizzi, and M. Raibert, "The LittleDog robot," *The International Journal of Robotics Research*, vol. 30, no. 2, pp. 145–149, Feb. 2011. [Online]. Available: http://journals.sagepub.com/doi/10.1177/0278364910387457

[42] M. Raibert, K. Blankespoor, G. Nelson, and R. Playter, "BigDog, the Rough-Terrain Quadruped Robot," *IFAC Proceedings Volumes*, vol. 41, no. 2, pp. 10 822–10 825, Jan. 2008. [Online]. Available: http://www.sciencedirect.com/science/article/pii/S1474667016407020

[43] M. Hutter, "StarlETH & Co.: Design and control of legged robots with compliant actuation," 2013.

[44] J. Hurst, "Building Robots That Can Go Where We Go - IEEE Spectrum." [Online]. Available: https://spectrum.ieee.org/robotics/humanoids/building-robots-that-can-go-where-we-go

[45] L. Raw, C. Fisher, and A. Patel, "Effects of Limb Morphology on Transient Locomotion in Quadruped Robots," in *2019 IEEE/RSJ International Conference on Intelligent Robots and Systems (IROS)*, Nov. 2019, pp. 3349–3356, iSSN: 2153-0866.

[46] M. H. Raibert, "Hopping in legged systems — Modeling and simulation for the two-dimensional one-legged case," *IEEE Transactions on Systems, Man, and Cybernetics*, vol. SMC-14, no. 3, pp. 451–463, May 1984.

[47] M. Zhao and Y. Qiu, "Event-based control for pneumatic single-legged hopping robot," in *2012 IEEE International Conference on Mechatronics and Automation*, Aug. 2012, pp. 297–302.

[48] A. H. Chang, C. Hubicki, A. Ames, and P. A. Vela, "Every Hop is an Opportunity: Quickly Classifying and Adapting to Terrain During Targeted Hopping," in *2019 International Conference on Robotics and Automation (ICRA)*, May 2019, pp. 3188–3194.

[49] M. Hutter, C. Gehring, D. Jud, A. Lauber, C. D. Bellicoso, V. Tsounis, J. Hwangbo, K. Bodie, P. Fankhauser, M. Bloesch, R. Diethelm, S. Bachmann, A. Melzer, and M. Hoepflinger, "ANYmal - a highly mobile and dynamic quadrupedal robot,"

in *2016 IEEE/RSJ International Conference on Intelligent Robots and Systems (IROS)*, Oct. 2016, pp. 38–44, iSSN: 2153-0866.

[50] D. Robinson, J. Pratt, D. Paluska, and G. Pratt, "Series elastic actuator development for a biomimetic walking robot," in *1999 IEEE/ASME International Conference on Advanced Intelligent Mechatronics (Cat. No.99TH8399)*, Sep. 1999, pp. 561–568.

[51] H. Kolvenbach, E. Hampp, P. Barton, R. Zenkl, and M. Hutter, "Towards Jumping Locomotion for Quadruped Robots on the Moon," in *2019 IEEE/RSJ International Conference on Intelligent Robots and Systems (IROS)*. Macau, China: IEEE, Nov. 2019, pp. 5459–5466. [Online]. Available: https://ieeexplore.ieee.org/document/8967552/

[52] M. Khoramshahi, A. Spröwitz, A. Tuleu, M. N. Ahmadabadi, and A. J. Ijspeert, "Benefits of an active spine supported bounding locomotion with a small compliant quadruped robot," in *2013 IEEE International Conference on Robotics and Automation*, May 2013, pp. 3329–3334.

[53] Y. H. Zhang, L. Zheng, W. J. Ge, and Z. H. Zou, "Mechanism design and optimization of a bionic kangaroo jumping robot," *IOP Conference Series: Materials Science and Engineering*, vol. 324, p. 012078, Mar. 2018. [Online]. Available: https://iopscience.iop.org/article/10.1088/1757-899X/324/1/012078

[54] C. Semini, N. G. Tsagarakis, B. Vanderborght, Y. Yang, and D. G. Caldwell, "HyQ - Hydraulically actuated quadruped robot: Hopping leg prototype," in *2008 2nd IEEE RAS EMBS International Conference on Biomedical Robotics and Biomechatronics*, Oct. 2008, pp. 593–599.

[55] T. Tanaka and S. Hirose, "Development of leg-wheel hybrid quadruped "AirHopper" design of powerful light-weight leg with wheel," in *2008 IEEE/RSJ International Conference on Intelligent Robots and Systems*, Sep. 2008, pp. 3890–3895.

[56] K. W. Wait and M. Goldfarb, "A Pneumatically Actuated Quadrupedal Walking Robot," *IEEE/ASME Transactions on Mechatronics*, vol. 19, no. 1, pp. 339–347, Feb. 2014. [Online]. Available: http://ieeexplore.ieee.org/document/6410036/

[57] R. van Varseveld and G. Bone, "Accurate position control of a pneumatic actuator using on/off solenoid valves," *IEEE/ASME Transactions on Mechatronics*, vol. 2, no. 3, pp. 195–204, Sep. 1997, conference Name: IEEE/ASME Transactions on Mechatronics.

[58] M.-C. Shih and M.-A. Ma, "Position control of a pneumatic cylinder using fuzzy PWM control method," *Mechatronics*, vol. 8, no. 3, pp. 241–253, Apr. 1998. [Online]. Available: http://www.sciencedirect.com/science/article/pii/S0957415898000051

[59] G. M. Bone and S. Ning, "Experimental Comparison of Position Tracking Control Algorithms for Pneumatic Cylinder Actuators," *IEEE/ASME Transactions on Mechatronics*, vol. 12, no. 5, pp. 557–561, Oct. 2007.

[60] P. G. Weyand, D. B. Sternlight, M. J. Bellizzi, and S. Wright, "Faster top running speeds are achieved with greater ground forces not more rapid leg movements," *Journal of Applied Physiology*, vol. 89, no. 5, pp. 1991–1999, Nov. 2000, publisher: American Physiological Society. [Online]. Available: https://journals.physiology.org/doi/full/10.1152/jappl.2000.89.5.1991

[61] M. P. Murphy, A. Saunders, C. Moreira, A. A. Rizzi, and M. Raibert, "The LittleDog robot:," *The International Journal of Robotics Research*, Dec. 2010, publisher: SAGE PublicationsSage UK: London, England. [Online]. Available: https://journals.sagepub.com/doi/10.1177/0278364910387457

[62] S. Seok, A. Wang, D. Otten, and S. Kim, "Actuator design for high force proprioceptive control in fast legged locomotion," in *2012 IEEE/RSJ International Conference on Intelligent Robots and Systems*, Oct. 2012, pp. 1970–1975, iSSN: 2153-0866.

[63] A. Spröwitz, A. Tuleu, M. Vespignani, M. Ajallooeian, E. Badri, and A. J. Ijspeert, "Towards dynamic trot gait locomotion: Design, control, and experiments with Cheetah-cub, a compliant quadruped robot," *The International Journal of Robotics Research*, vol. 32, no. 8, pp. 932–950, Jul. 2013. [Online]. Available: https://doi.org/10.1177/0278364913489205

[64] L. Ding, H. Gao, Z. Deng, J. Song, Y. Liu, G. Liu, and K. Iagnemma, "Foot–terrain interaction mechanics for legged robots: Modeling and experimental validation," *The*

International Journal of Robotics Research, vol. 32, no. 13, pp. 1585–1606, Nov. 2013. [Online]. Available: http://journals.sagepub.com/doi/10.1177/0278364913498122

[65] D. Kim, S. J. Jorgensen, J. Lee, J. Ahn, J. Luo, and L. Sentis, "Dynamic locomotion for passive-ankle biped robots and humanoids using whole-body locomotion control," *The International Journal of Robotics Research*, vol. 39, no. 8, pp. 936–956, Jul. 2020, publisher: SAGE Publications Ltd STM. [Online]. Available: https://doi.org/10.1177/0278364920918014

[66] M. Gienger, K. Loffler, and F. Pfeiffer, "Towards the design of a biped jogging robot," in *Proceedings 2001 ICRA. IEEE International Conference on Robotics and Automation (Cat. No.01CH37164)*, vol. 4, May 2001, pp. 4140–4145 vol.4, iSSN: 1050-4729.

[67] K. Narioka, A. Rosendo, A. Sproewitz, and K. Hosoda, "Development of a minimalistic pneumatic quadruped robot for fast locomotion," in *2012 IEEE International Conference on Robotics and Biomimetics (ROBIO)*, Dec. 2012, pp. 307–311.

[68] M. Shahrokni, Q. Zhu, J. Liu, W. Tetzlaff, and T. Oxland, "Design and biomechanical evaluation of a rodent spinal fixation device," *Spinal cord*, vol. 50, pp. 543–7, Jan. 2012.

[69] J. S.colett and J. Hurst, "Artificial restraint systems for walking and running robots: An overview," *International Journal of Humanoid Robotics*, vol. 09, Jul. 2012.

[70] B. Brown and G. Zeglin, "The bow leg hopping robot," in *Proceedings. 1998 IEEE International Conference on Robotics and Automation (Cat. No.98CH36146)*, vol. 1, May 1998, pp. 781–786 vol.1, iSSN: 1050-4729.

[71] B. Andrews, B. Miller, J. Schmitt, and J. E. Clark, "Running over unknown rough terrain with a one-legged planar robot," *Bioinspiration & Biomimetics*, vol. 6, no. 2, p. 026009, Jun. 2011. [Online]. Available: https://iopscience.iop.org/article/10.1088/1748-3182/6/2/026009

[72] M. Alghooneh, C. Q. Wu, and M. Esfandiari, "A Passive-Based Physical Bipedal Robot With a Dynamic and Energy-Efficient Gait on the Flat Ground,"

IEEE/ASME Transactions on Mechatronics, vol. 21, no. 4, pp. 1977–1984, Aug. 2016, conference Name: IEEE/ASME Transactions on Mechatronics.

[73] A. Sato and M. Buehler, "A planar hopping robot with one actuator: design, simulation, and experimental results," in *2004 IEEE/RSJ International Conference on Intelligent Robots and Systems (IROS) (IEEE Cat. No.04CH37566)*, vol. 4, Sep. 2004, pp. 3540–3545 vol.4.

[74] R. Colbrunn, G. Nelson, and R. Quinn, "Design and control of a robotic leg with braided pneumatic actuators," in *Proceedings 2001 IEEE/RSJ International Conference on Intelligent Robots and Systems. Expanding the Societal Role of Robotics in the the Next Millennium (Cat. No.01CH37180)*, vol. 2, Oct. 2001, pp. 992–998 vol.2.

[75] M. Ahmadi and M. Buehler, "The ARL monopod II running robot: control and energetics," in *Proceedings 1999 IEEE International Conference on Robotics and Automation (Cat. No.99CH36288C)*, vol. 3, May 1999, pp. 1689–1694 vol.3, iSSN: 1050-4729.

[76] J. Pratt, C.-M. Chew, A. Torres, P. Dilworth, and G. Pratt, "Virtual Model Control: An Intuitive Approach for Bipedal Locomotion." *I. J. Robotic Res.*, vol. 20, pp. 129–143, Jan. 2001.

[77] M. van den Broek, "Fast Self-Stable Planar Bipedal Running," 2019. [Online]. Available: https://repository.tudelft.nl/islandora/object/uuid%3A3b31bc33-1f67-4fda-85db-5dace4835bcf

[78] "Planar Elliptical Runner is biped with clever mechanical design." [Online]. Available: https://techxplore.com/news/2017-05-planar-elliptical-runner-biped-clever.html

[79] R. Labbe, "Kalman and Bayesian Filters in Python," Oct. 2020, original-date: 2014-05-16T19:24:36Z. [Online]. Available: https://github.com/rlabbe/Kalman-and-Bayesian-Filters-in-Python

[80] R. Faragher, "Understanding the Basis of the Kalman Filter Via a Simple and Intuitive Derivation [Lecture Notes]," *IEEE Signal Processing Magazine*, vol. 29, no. 5, pp. 128–132, Sep. 2012, conference Name: IEEE Signal Processing Magazine.

[81] S. Haykin, "Kalman Filters," in *Kalman Filtering and Neural Networks*. John Wiley & Sons, Ltd, 2002, pp. 1–21, section: 1 _eprint: https://onlinelibrary.wiley.com/doi/pdf/10.1002/0471221546.ch1. [Online]. Available: https://onlinelibrary.wiley.com/doi/abs/10.1002/0471221546.ch1

[82] G. Welch and G. Bishop, "An Introduction to the Kalman Filter," p. 16, 2006.

[83] H. Celik and S. J. Piazza, "Simulation of Aperiodic Bipedal Sprinting," *Journal of Biomechanical Engineering*, vol. 135, no. 8, p. 081008, Jun. 2013. [Online]. Available: http://biomechanical.asmedigitalcollection.asme.org/article.aspx?doi=10.1115/1.4024577

[84] F. White, *Fluid Mechanics*, ser. McGraw-Hill series in mechanical engineering. McGraw Hill, 2011. [Online]. Available: https://books.google.co.za/books?id=egk8SQAACAAJ

[85] M. Boles and D. Yunus A. Cengel, *Thermodynamics: An Engineering Approach*. McGraw-Hill Education, 2014. [Online]. Available: https://books.google.co.za/books?id=Ao95ngEACAAJ

[86] C. Fisher, "Trajectory optimization inspired design for legged robotics," 2021, publisher: University of Cape Town Engineering and the Built Environment.

[87] S. Kalouche, "GOAT: A legged robot with 3D agility and virtual compliance," in *2017 IEEE/RSJ International Conference on Intelligent Robots and Systems (IROS)*, Sep. 2017, pp. 4110–4117.

[88] "A80-6_a Series Dynamical Modular_robot Dynamics_t-MOTOR Store-Official Store for T-motor drone motor,ESC,Propeller." [Online]. Available: https://store-en.tmotor.com/goods.php?id=894

[89] "A80-9_a Series Dynamical Modular_robot Dynamics_t-MOTOR Store-Official Store for T-motor drone motor,ESC,Propeller." [Online]. Available: https://store-cn.tmotor.com/goods.php?id=895

[90] D. W. Haldane, M. M. Plecnik, J. K. Yim, and R. S. Fearing, "Robotic vertical jumping agility via series-elastic power modulation," *Science Robotics*, vol. 1, no. 1, Dec. 2016, publisher: Science Robotics Section: Research Article. [Online]. Available: https://robotics.sciencemag.org/content/1/1/eaag2048

[91] M. Haberland and S. Kim, "On extracting design principles from biology: Ii. case study - the effect of knee direction on bipedal robot running efficiency," *Bioinspiration and biomimetics*, vol. 10, p. 016011, 02 2015.

[92] "ODrive Docs." [Online]. Available: https://docs.odriverobotics.com/

[93] L. Boast, A. Houser, K. Good, and M. Gusset, "Regional variation in body size of the cheetah (acinonyx jubatus)," *Journal of Mammalogy*, vol. 94, p. 1293–1297, 12 2013.

[94] Pan Wen-Hao, Eatherton Matthew R., Tao Mu-Xuan, Yang Yue, and Nie Xin, "Design of Single-Level Guyed Towers Considering Interrelationship between Bracing Strength and Rigidity Requirements," *Journal of Structural Engineering*, vol. 143, no. 9, p. 04017128, Sep. 2017. [Online]. Available: https://ascelibrary.org/doi/10.1061/%28ASCE%29ST.1943-541X.0001857

[95] M. Heydari, H. Moharrami, and H. Yazdani-Paraei, "Nonlinear Analysis and Optimum Design of Guyed Masts," *Journal of Optimization Theory and Applications*, vol. 155, no. 3, pp. 1025–1046, Dec. 2012. [Online]. Available: https://doi.org/10.1007/s10957-012-0098-2

[96] R. Budynas, J. Shigley, and J. Nisbett, *Shigley's Mechanical Engineering Design*, ser. McGraw-Hill series in mechanical engineering. McGraw-Hill, 2008, no. v. 10. [Online]. Available: https://books.google.co.za/books?id=Cd0eAQAAIAAJ

[97] R. Knight, *Physics for Scientists and Engineers: A Strategic Approach*. Pearson, 2013, no. v. 5. [Online]. Available: https://books.google.co.za/books?id=0U96jgEACAAJ

[98] "Spectroid – Apps on Google Play." [Online]. Available: https://play.google.com/store/apps/details?id=org.intoorbit.spectrum&hl=en_ZA&gl=US

[99] S. Shield, "Tutorials in lagrangian mechanics, trajectory optimization and pyomo," 2020. [Online]. Available: https://github.com/UCTMechatronics/pyomo_tutorials

Appendix A: Theory Development

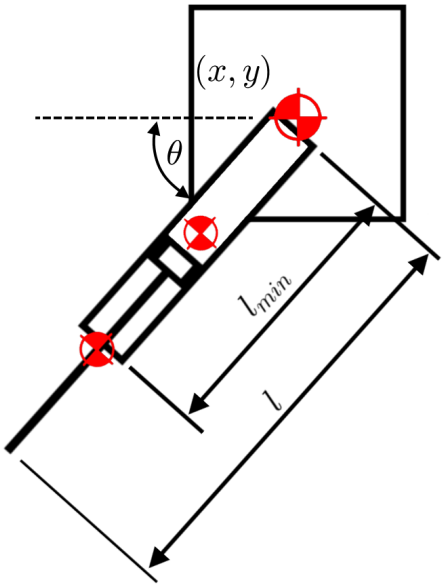

Figure A.1: System definition for the systems in Sections A.1 and A.2

A.1 Motor Test 1

The equation used for the system was as follows

$$\begin{aligned} T(t) &= I\alpha(t) \\ \omega(t) &= \int \alpha(t)dt \\ \theta(t) &= \int \omega(t)dt \end{aligned} \tag{A.1}$$

In this equation the torque is set by the ideal motor model with

$$T = T_{stall}\left(1 - \frac{\omega}{\omega_{no\ load}}\right) \tag{A.2}$$

A.2 Motor Test 2

For motor test to lagrangian methods were used to develop the equation of motion for the system. These equations are based on, and explained more thoroughly, in a tutorial series by Stacy Shield [99].

These equations being based on the general form for Legrange Mechanics:

$$\frac{d}{dt}\left(\frac{\partial T}{\partial \dot{q}_i}\right) - \frac{d}{dt}\left(\frac{\partial V}{\partial \dot{q}_i}\right) - \frac{\partial T}{\partial q_i} + \frac{\partial U}{\partial q_i} = Q \tag{A.3}$$

The coordinate system for this system being

$$q = \begin{bmatrix} x & y & \theta & l \end{bmatrix}^T \tag{A.4}$$

Where x and y defined the CoM of the body, θ the leg angle and l the leg length (which could vary between l_{min} and $2l_{min}$.The centres of mass of the cylinder and the rod were then defined as:

$$COM_{motor} = \begin{bmatrix} x \\ y \end{bmatrix} \tag{A.5}$$

$$COM_{cyl} = \begin{bmatrix} x + 0.5l_{min}\cos(\theta) \\ y + 0.5l_{min}\sin(\theta) \end{bmatrix} \tag{A.6}$$

$$COM_{rod} = \begin{bmatrix} x + (0.5l_{min} + l)\cos(\theta) \\ y + (0.5l_{min} + l)\sin(\theta) \end{bmatrix} \tag{A.7}$$

while the foot position was defined similarly as

$$foot = \begin{bmatrix} x + l\cos(\theta) \\ y + l\sin(\theta) \end{bmatrix} \tag{A.8}$$

In addition to the above there were four major non-conservative forces acting in the system: the ground reaction force (GRX), friction (F_{fric}), internal cylinder forces (F_{cyl}) and the motor torque (T).

These forces were then converted to generalised forces as torques as follows:

$$F_{cyl} = \begin{bmatrix} F_{cyl}\cos(\theta) \\ F_{cyl}\sin(\theta) \\ 0 \end{bmatrix}$$

$$r_{cyl} = \begin{bmatrix} xCOM_{cyl} \\ yCOM_{cyl} \\ 0 \end{bmatrix}$$

$$Q_{cyl} = J(r_{cyl}, q)^T F_{cyl} \tag{A.9}$$

$$T = \begin{bmatrix} 0\cos(\theta) \\ 0\sin(\theta) \\ T \end{bmatrix}$$

$$r_T = \begin{bmatrix} x \\ y \\ \theta \end{bmatrix}$$

$$Q_T = J(r_T, q)^T T \tag{A.10}$$

$$GRX = \begin{bmatrix} 0 \\ GRX \\ 0 \end{bmatrix}$$

$$r_{GRX} = \begin{bmatrix} foot_x \\ foot_y \\ 0 \end{bmatrix}$$

$$Q_{GRX} = J(r_{GRX}, q)^T GRX \tag{A.11}$$

$$F_{Fric} = \begin{bmatrix} F_{Fric} \\ 0 \\ 0 \end{bmatrix}$$

$$r_{Fric} = \begin{bmatrix} foot_x \\ foot_y \\ 0 \end{bmatrix}$$

$$Q_{Fric} = J(r_{Fric}, q)^T F_{Fric} \tag{A.12}$$

From this the final expression for Q can be found to be:

$$Q_{tot} = Q_{cyl} + Q_T + Q_{GRX} + Q_{Fric} \tag{A.13}$$

The potential energy is then foud as:

$$V = g * (M_{motor} * y + M_{cyl} * yCOM_{cyl} + M_{rod} * yCOM_{Rod}) \tag{A.14}$$

following this the kinetic energy is found as:

$$\begin{aligned} T = 0.5(&M_{motor}(J(COM_{motor}, q))^T J(COM_{motor}, q) \\ &+ M_{cyl}(J(COM_{cyl}, q))^T J(COM_{cyl}, q) \\ &+ M_{rod}(J(COM_{rod}, q))^T J(COM_{rod}, q)) \\ &+ 0.5 * (dTheta^2) Ileg \end{aligned} \tag{A.15}$$

These terms are then partially differentiated to give the final equation of motion of the system. This was solved using Matlab's symbolic Library and is too large to show here.

Appendix B: Mechanical Drawings

B.1 Platform Parts

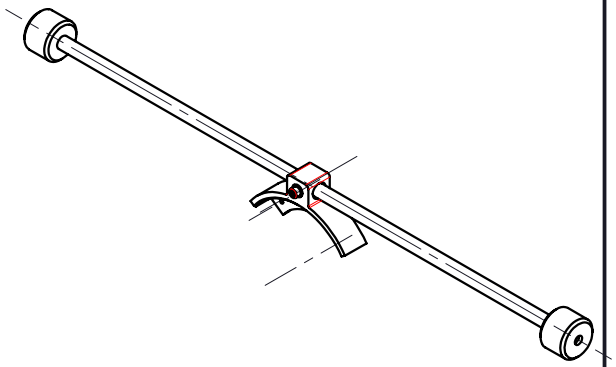

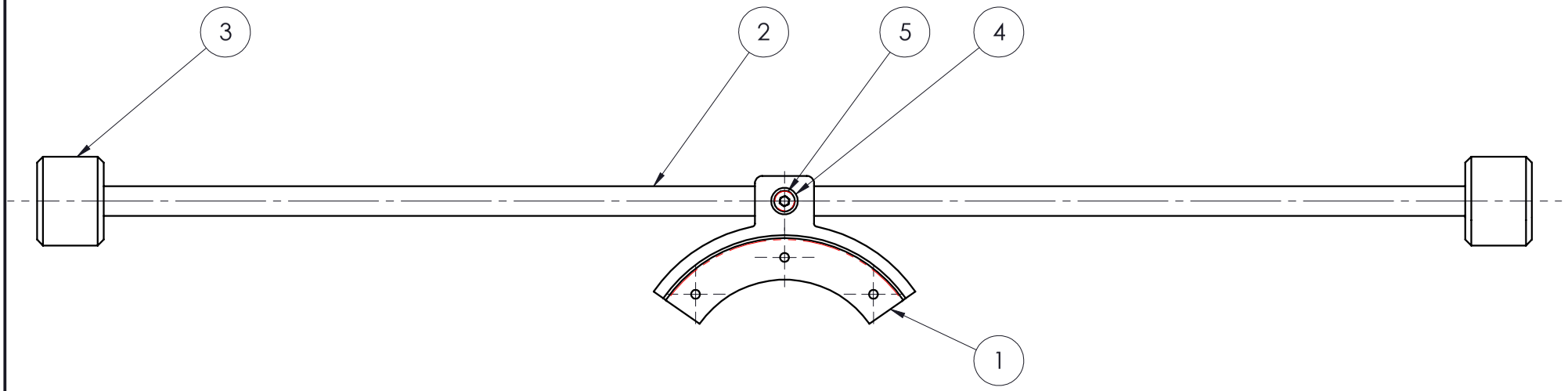

NO.	PART NUMBER	DESCRIPTION	SPECIFICATION	QTY
5	ISO 4762 M4 x 10 - 10N			2
4	ISO 10673-3.6-N			2
3	BDY PRT 001	Body End Weights	See DWG for details, Plain Carbon Steel	2
2	BDY PRT 002	Body Arm	See DWG for details, 1060 Alloy	1
1	BDY PRT 003	Motor Body Holder	See DWG for details, 1060 Alloy	1

Scale: 1:5 on A4	University of Cape Town Department of Mechanical Engineering			
Drawn By: Joshua van Zyl	All un-toleranced dimensions to adhere to ISO 2768-m	Title: Body Assembly		
Checked :	Assembly Drawing	Drawing Number : Body Assembly	Rev. : A	Sheet : 1 of 1

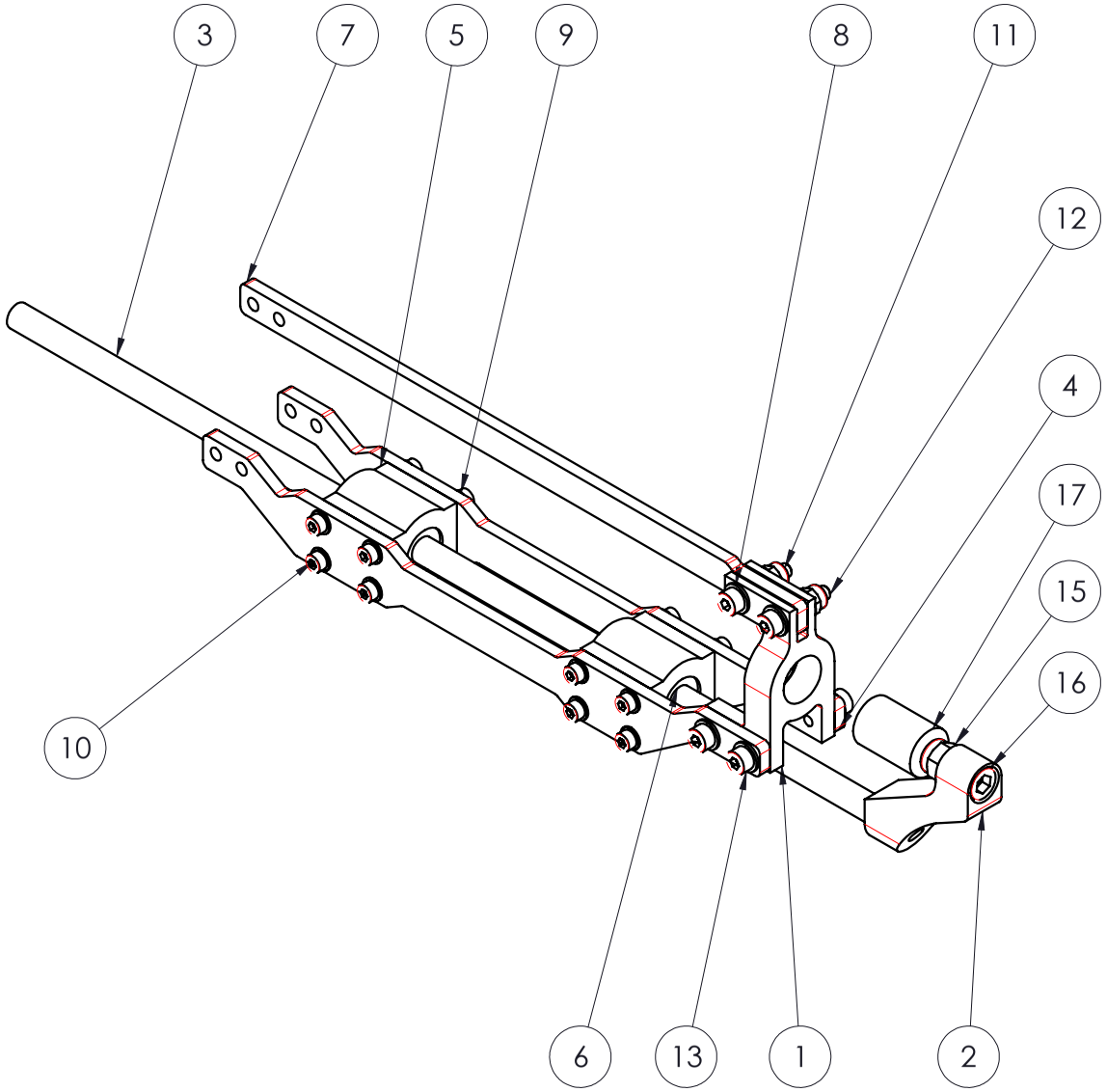

NO.	PART NUMBER	DESCRIPTION	SPECIFICATION	QTY
17	Coupling	Coupling	See DWG for details, Rubber	1
16	ISO 4762 M6 x 20 - 20N			1
15	ISO 7040-M6-N			1
14	Circlip DIN 472 - 15 x 1			2
13	ISO 4762 M4 x 10 - 10N			4
12	ISO 4762 M4 x 20 - 20N			2
11	ISO 7040-M4-N			2
10	ISO 4762 M3 x 10 - 10N			16
9	ISO 10673-2.75-N			16
8	ISO 10673-3.6-N			8
7	SUPP PRT 001	Support Bar Thin	See DWG for details, 5454-H34	1
6	SKF LBBR8	Linear Ball Bearing	See DWG for details, Alloy Steel	2
5	SUPP PRT 005	Linear Bearing Block	See DWG for details, 6061 Alloy	2
4	SUPP PRT 002	Support Bar Thick	See DWG for details, 5454-H34	2
3	SUPP PRT 004	Cylinder Support Rod	See DWG for details, Alloy Steel	1
2	SUPP PRT 005	Foot Link	See DWG for details, Alloy Steel	1
1	SUPP PRT 003	Cylinder Support Bar Holder	See DWG for details, 6061 Alloy	1

Scale: 1:2 on A4

University of Cape Town
Department of Mechanical Engineering

Drawn By: Joshua van Zyl

All un-toleranced dimensions to adhere to ISO 2768-m

Title: Support Subassembly

Checked :

Assembly Drawing

Drawing Number : Support SubassemblyA

Rev. :

Sheet : 1 of 1

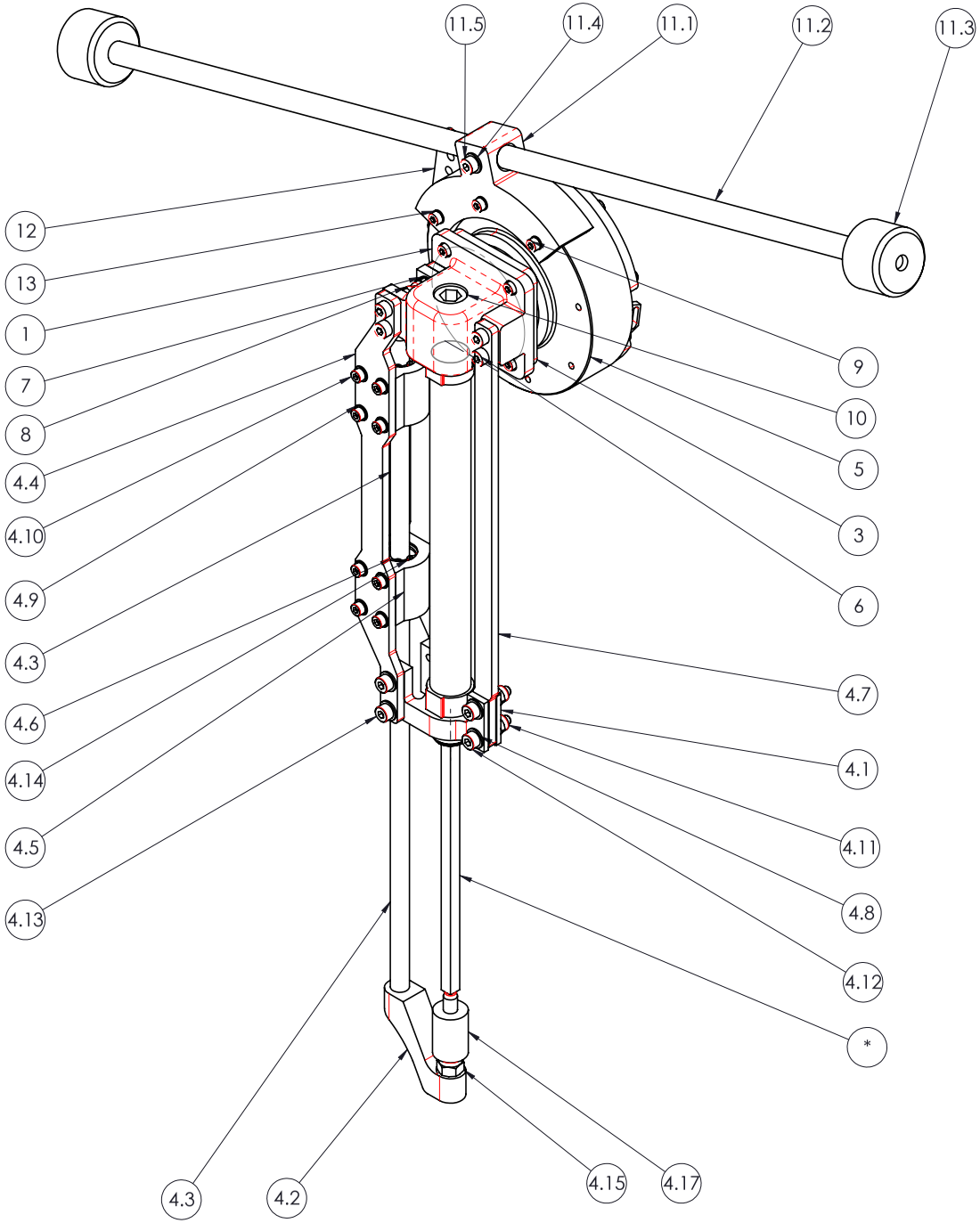

NO.	PART NUMBER	DESCRIPTION	SPECIFICATION	QTY
13	ISO 10673-2.75-S			11
12	Boom Part	Motor Boom Interface	See DWG for details, 1060 Alloy	1
11.5	ISO 4762 M4 x 10 - 10N			2
11.4	ISO 10673-3.6-N			2
11.3	BDY PRT 001	Body End Weights	See DWG for details, Plain Carbon Steel	2
11.2	BDY PRT 002	Body Arm	See DWG for details, 1060 Alloy	1
11.1	BDY PRT 003	Motor Body Holder	See DWG for details, 1060 Alloy	1
11	Body Assembly	Body Assembly	See DWG for details	1
10	ISO 4029 - M16 x 12-N			1
9	ISO 4762 M3 x 10 - 10N			21
8	ISO 7040-M4-N			4
7	ISO 10673-3.6-S			4
6	ISO 4762 M4 x 16 - 16N			6
5	A80-6	TMotor A80-6		1
4.17	Coupling	Coupling	See DWG for details, Rubber	1
4.16	ISO 4762 M6 x 20 - 20N			1
4.15	ISO 7040-M6-N			1
4.14	Circlip DIN 472 - 15 x 1			2
4.13	ISO 4762 M4 x 10 - 10N			4
4.12	ISO 4762 M4 x 20 - 20N			2
4.11	ISO 7040-M4-N			2
4.10	ISO 4762 M3 x 10 - 10N			16
4.9	ISO 10673-2.75-N			16
4.8	ISO 10673-3.6-N			8
4.7	SUPP PRT 001	Support Bar Thin	See DWG for details, 5454-H34	1
4.6	SKF LBBR8	Linear Ball Bearing	See DWG for details, Alloy Steel	2
4.5	SUPP PRT 005	Linear Bearing Block	See DWG for details, 6061 Alloy	2
4.4	SUPP PRT 002	Support Bar Thick	See DWG for details, 5454-H34	2
4.3	SUPP PRT 004	Cylinder Support Rod	See DWG for details, Alloy Steel	1
4.2	SUPP PRT 005	Foot Link	See DWG for details, Alloy Steel	1
4.1	SUPP PRT 003	Cylinder Support Bar Holder	See DWG for details, 6061 Alloy	1
4	Support Subassembly	Support Subassembly	See DWG for details	1
3	PRT 002	Motor-Clamp Interface	See DWG for details, 6061 Alloy	1
2	DSNU-16-125			1
1	PRT001	Cylinder Motor Interface	See DWG for details, 6061 Alloy	1

Scale: 1:10 on A3	University of Cape Town Department of Mechanical Engineering			
Drawn By: <Name>	All un-toleranced dimensions to adhere to ISO 2768-m	Title:		
Checked :	Assembly drawing	Drawing Number :	Rev. : A	Sheet : 1 of 1

B.2 Boom Parts

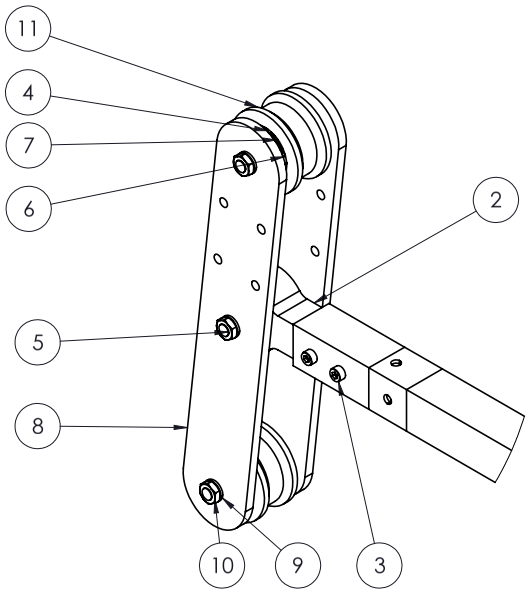

DETAIL A
SCALE 1 : 2

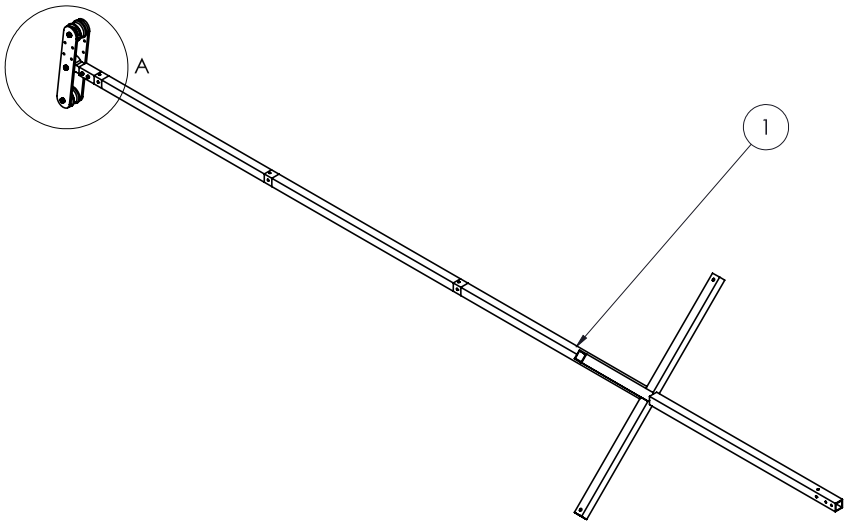

ITEM NO.	PART NUMBER	DESCRIPTION	QTY.
1	MainBoomWCross		1
	MainPole		1
	CrossBeam2018		4
2	PoleBearingHolder2018		1
3	ISO 4762 M3 x 8 - 8N		4
4	Circlip DIN 472 - 19 x 1		3
5	EndShaft2018		3
6	DIN 625 - 626 - 8,SI,NC,8_68		3
7	Circlip DIN 471 - 6 x 0.7		6
8	EndPlate2018		2
9	ISO 10673-4.55-S		6
10	ISO - 4035 - M5 - N		6
11	PulleyTip2		2

Scale: 1:10 on A3	University of Cape Town Department of Mechanical Engineering			
Drawn By: <Name>	All un-toleranced dimensions to adhere to ISO 2768-m	Title: Boom Pole Assembly		
Checked :	Assembly drawing	Drawing Number :	Rev. : A	Sheet : 1 of 1

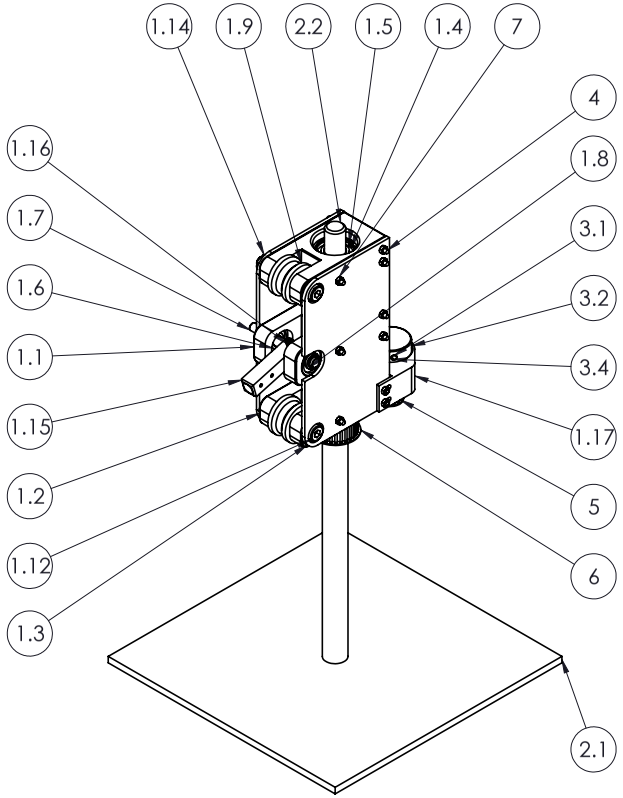

ITEM NO.	PART NUMBER	DESCRIPTION	QTY.
1	Boom Bearing Block Assembly		1
1.1	MainPoleBearingBlock		1
1.2	PulleyBearingBlock		2
1.3	SidePlate2018		2
1.4	DIN 625 - 6004 - 12,SI,NC,12_68		3
1.5	Circlip DIN 472 - 42 x 1.75		3
1.6	DIN 625 - 6200 - 8,SI,NC,8_68		2
1.7	MainPoleShaft		1
1.8	Circlip DIN 471 - 10 x 1		2
1.9	PulleyBase		2
1.10	DIN 625 - 629 - 8,SI,NC,8_68		2
1.11	Circlip DIN 472 - 26 x 1.2		2
1.12	DIN 7984 - M10 x 70 --- 26N		2
1.13	ISO 10673-9.3-S		2
1.14	ISO - 4032 - M10 - D - N		2
1.15	PoleRootShaftHolder		1
1.16	ISO 4762 M4 x 8 - 8N		2
1.17	Base encoder mount		1
2	Boom Upright		1
2.1	BoomBasePlate		1
2.2	UprightBoomPole		1
3	E6B2-CWZ6C		1
3.1	E6B2-CWZ6C-1		1
3.2	E6B2-CWZ6C-2		1
3.3	ISO 1224 - 190615 - R,10,SI,NC,10_68		1
3.4	E6B2-CWZ6C-3		1
3.5	ISO 7046-1 - M2 x 3 - Z --- 3N		3
4	M4 ThreadRod		9
5	14-5M-009		1
6	28-5M-015		1
7	ISO - 4032 - M4 - D - N		18

Scale: 1:5 on A3	University of Cape Town Department of Mechanical Engineering			
Drawn By: <Name>	All un-toleranced dimensions to adhere to ISO 2768-m	Title: Upright Assembly		
Checked :	Assembly drawing	Drawing Number :	Rev. : A	Sheet : 1 of 1

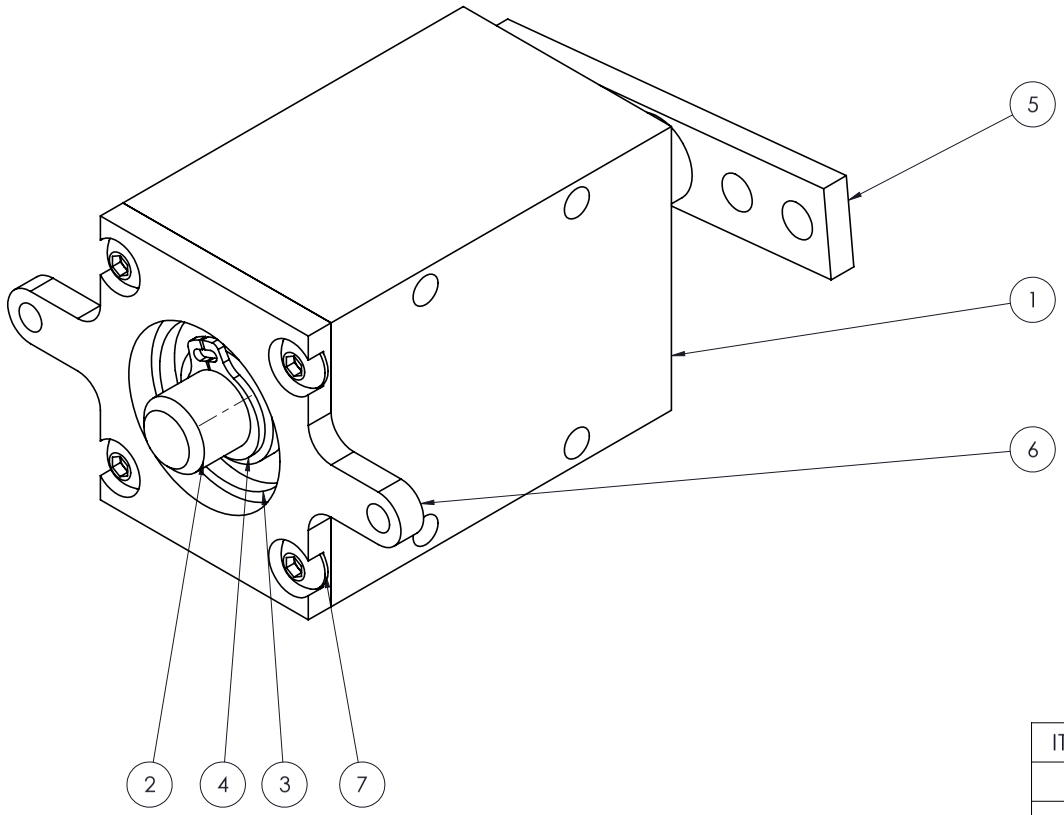

ITEM NO.	PART NUMBER	DESCRIPTION	QTY.
1	EndRollBlock		1
2	EndRollShaft		1
3	DIN 625 - 608 - 8,SI,NC,8_68		2
4	Circlip DIN 471 - 8 x 0.8		1
5	EndEffectorPlate		1
6	EndBearingPlate		1
7	ISO 7380 - M3 x 8 - 8N		4

Scale: 2:1 on A3	University of Cape Town Department of Mechanical Engineering			
Drawn By: <Name>	All un-toleranced dimensions to adhere to ISO 2768-m	Title:		
Checked :	Assembly drawing	Drawing Number :	Rev. : A	Sheet : 1 of 1

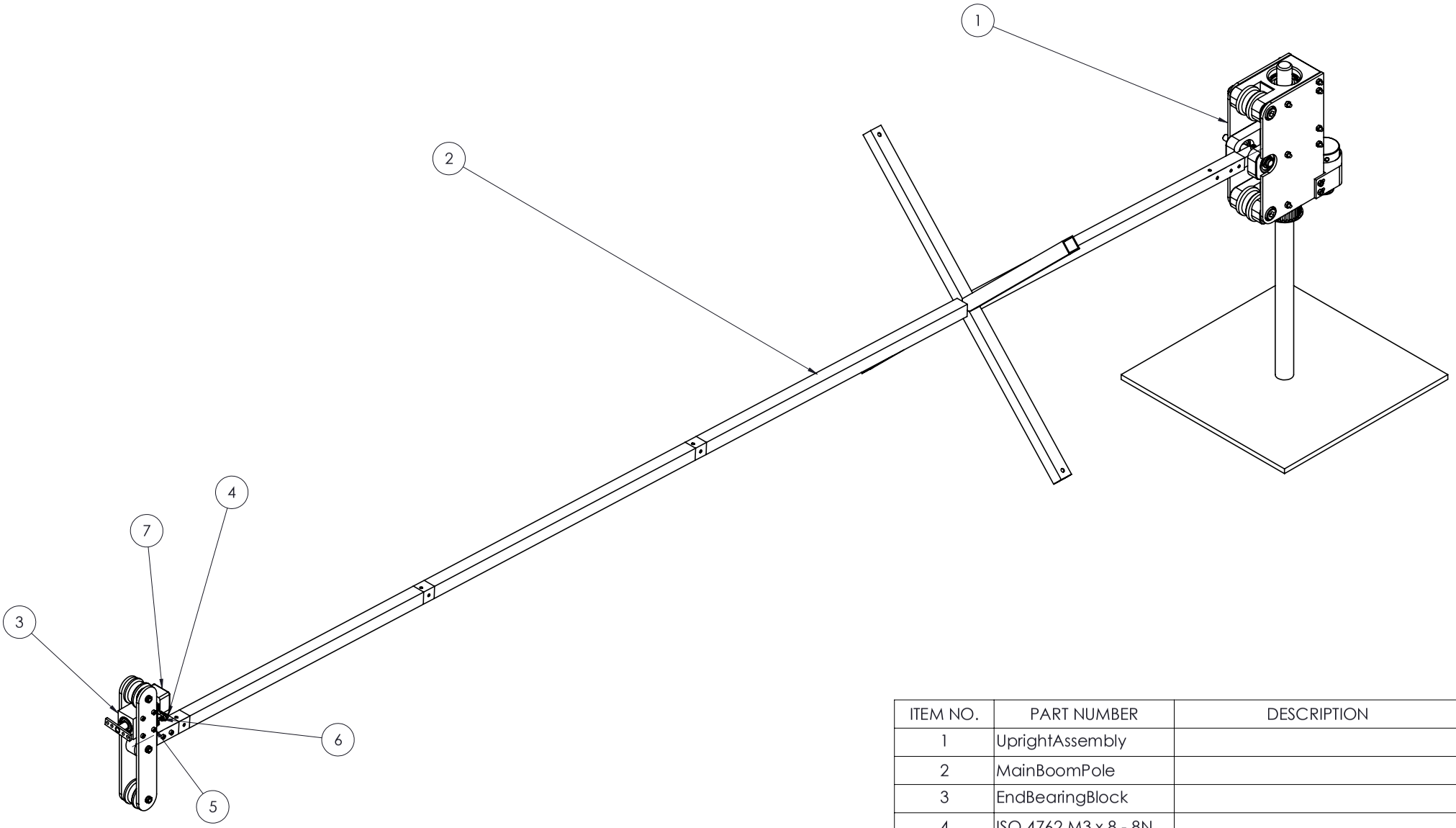

ITEM NO.	PART NUMBER	DESCRIPTION	QTY.
1	UprightAssembly		1
2	MainBoomPole		1
3	EndBearingBlock		1
4	ISO 4762 M3 x 8 - 8N		2
5	ISO 4762 M3 x 10 - 10N		8
6	ISO - 4032 - M3 - D - N		2
7	HEDL Encoder		1

Scale: 1:5 on A3	University of Cape Town Department of Mechanical Engineering			
Drawn By: <Name>	All un-toleranced dimensions to adhere to ISO 2768-m	Title:		
Checked :	Assembly drawing	Drawing Number :	Rev. : A	Sheet : 1 of 1

Appendix C: Kalman Filter

The general form equation for a Kalman filter are broken up into a predict and update phase. The predict phase is defined as:

$$\begin{aligned} \bar{x} &= \mathrm{Fx} + \mathrm{Bu} \\ \bar{P} &= \mathrm{FPF}^T + Q \end{aligned} \tag{C.1}$$

Where F describes the motion of the system, x is the current system state, B is the effect the control input has on the system and u is the control input itself.

$$\begin{aligned} y &= z - H\bar{x} \\ K &= \bar{P}H^T\left(H\bar{P}H^T + R\right)^{-1} \\ x &= \bar{x} + \mathrm{Ky} \\ P &= (I - \mathrm{KH})\,\bar{P} \end{aligned} \tag{C.2}$$

In this case y is the residual, z the sensor measurements, H a unit conversion matrix between the filters output and the measurements.

Option 1 for the KF, where the accelerometer was used as a control input had the following

values:

$$
\begin{aligned}
F &= \begin{bmatrix} 1 & \mathrm{dt} & 0.5\mathrm{dt}^2 \\ 0 & 1 & \mathrm{dt} \\ 0 & 0 & 1 \end{bmatrix} \\
Q &= \begin{bmatrix} \frac{\mathrm{dt}^4}{4} & \frac{\mathrm{dt}^3}{2} & \frac{\mathrm{dt}^2}{2} \\ \frac{\mathrm{dt}^3}{2} & \mathrm{dt}^2 & \mathrm{dt} \\ \frac{\mathrm{dt}^2}{2} & \mathrm{dt} & 1 \end{bmatrix} \sigma^2 \\
\sigma^2 &= \frac{\mathrm{dA_{max}}}{5} \\
B &= 0 \\
U &= 0 \\
H &= \begin{bmatrix} 100 & 0 & 0 \\ 0 & 0 & 9.81 \end{bmatrix} \\
R &= \begin{bmatrix} 2.5^2 & 0 & 0 \\ 0 & 0 & \left(3.65\mathrm{x}10^{-5}\right)^2 \end{bmatrix}
\end{aligned} \tag{C.3}
$$

The second option was

$$
\begin{aligned}
F &= \begin{bmatrix} 1 & \mathrm{dt} & 0.5\mathrm{dt}^2 \\ 0 & 1 & \mathrm{dt} \\ 0 & 0 & 0 \end{bmatrix} \\
Q &= \begin{bmatrix} \frac{\mathrm{dt}^4}{4} & \frac{\mathrm{dt}^3}{2} & \frac{\mathrm{dt}^2}{2} \\ \frac{\mathrm{dt}^3}{2} & \mathrm{dt}^2 & \mathrm{dt} \\ \frac{\mathrm{dt}^2}{2} & \mathrm{dt} & 1 \end{bmatrix} \sigma^2 \\
\sigma^2 &= \mathrm{dA}_{\max} \\
B &= 1 \\
U &= \begin{bmatrix} 0 \\ 0 \\ \mathrm{Az} * 9.81 \end{bmatrix} \\
H &= \begin{bmatrix} 100 & 0 & 0 \end{bmatrix} \\
R &= \begin{bmatrix} 2.5^2 & 0 & 0 \end{bmatrix}
\end{aligned} \tag{C.4}
$$

Appendix D: Code

For controller/system master code please see:

https://github.com/JayVeeZee/Masters/tree/master/ControllerCode/TeensyKF

For sensor or motor pass-through code please see:

https://github.com/JayVeeZee/Masters/tree/master/SensorCode

Appendix E: Test Data

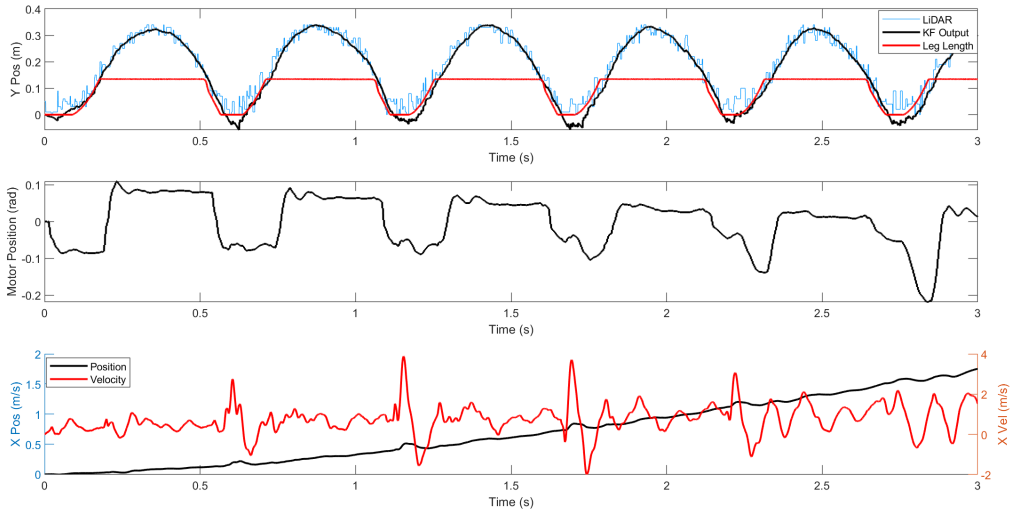

Figure E.1: Long time horizon hopping test with an initial launch angle of 5°

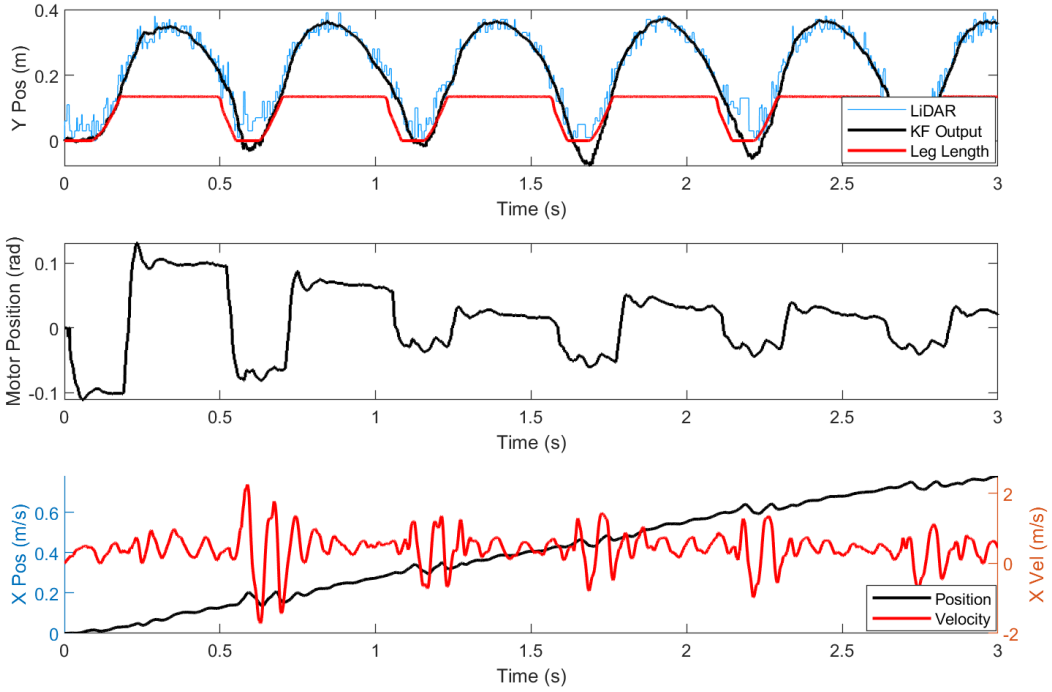

Figure E.2: Long time horizon hopping test with an initial launch angle of 6°

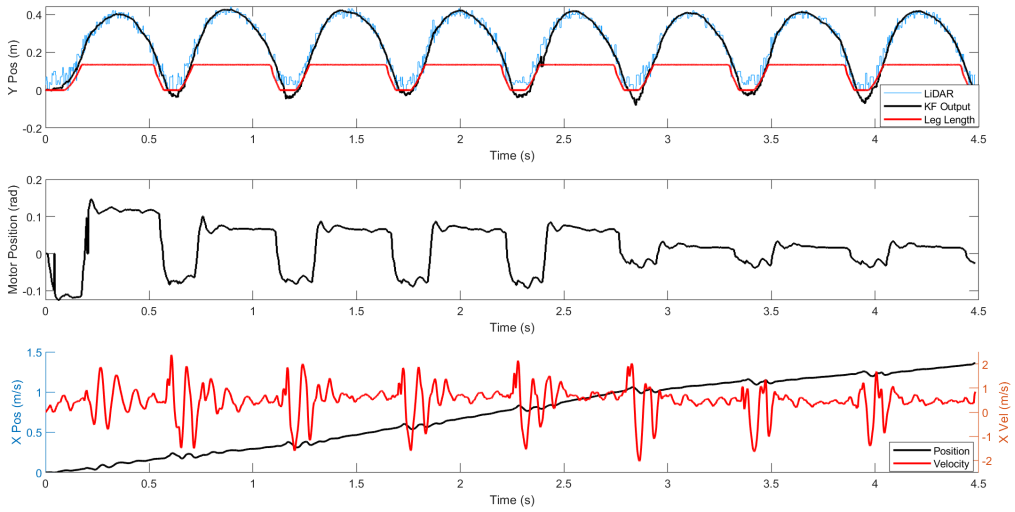

Figure E.3: Long time horizon hopping test with an initial launch angle of 7°